Czech Technical University in Prague

Faculty of Electrical Engineering

Doctoral Thesis

August 2017

Ing. Ondřej Zoubek

Czech Technical University in Prague

Faculty of Electrical Engineering
Department of Electric Drives and Traction

APPLICATION OF FIELD PROGRAMMABLE GATE ARRAYS IN SOPHISTICATED CONTROL STRUCTURES OF ELECTRIC DRIVES

Doctoral Thesis

Ing. Ondřej Zoubek

Prague, August 2017

Ph.D. Programme: Electrical Engineering and Information Technology
Branch of study: Electric Machines, Apparatus and Drives

Supervisor: Ing. Jiří Zděnek, CSc.

Statement

I declare that I am the only author of the doctoral thesis entitled "Application of Field Programmable Gate Arrays in Sophisticated Control Structures of Electric Drives", led by supervisor Ing. Jiří Zděnek, CSc. and I have used only the literature listed at the end of the thesis in the list of used literature.

Ing. Ondřej Zoubek

Acknowledgments

I would like to thank to my supervisor Ing. Jiří Zděnek, CSc. for the great cooperation on our research topic, for his patience and guidance throughout the entire work. He has provided me with lot of valuable remarks, comment and advices helping my thesis to be successful. He has led my work toward the goal and helped me to overcome many difficulties.

This work could not arise without enthusiasm for rolling stock of many people. Namely Robert Škrlant, train driver and serviceman from company SD – Kolejová doprava, a.s., the owner and operator of the locomotives on which the research was conducted, Ing. Pavel Mňuk, CSc. from the company JOXIMA, s.r.o., the provider of the locomotive computer and RNDr. Bedřich Pola from the company ASIX s.r.o. for the material support provided for this work.

Last but not least, I would like to thank my family, especially my wife Barbora, for her support, patience and determination. Without her the thesis would never have been completed.

Abstract

This doctoral thesis deals with the transmission of traction power from the traction vehicle to the train and presents an analysis of the current state of operation of the slip regulator on the III. generation heavy freight locomotive Škoda factory designation 93E.

It was necessary to use Field Programmable Gate Array (FPGA) technology to acquire, process and record the data. The introductory part of the thesis is an introduction to the field of the FPGAs and briefly summarizes the history of these integrated circuits.

The basic elements of the traction power transmission system are the traction motor, the mechanical system of the traction motor-wheelset and its rotary mass and the wheel-rail contact.

From the point of view of the traction motor and its regulator, an analysis of the influence on damping of the mechanical system oscillations by the traction motor and its excitation was performed.

The most extensive part of the thesis deals with the motor-wheelset three-mass mechanical system model and its influence on the locomotive's adhesion properties. The model parameters were obtained by analyzing measured speed data of the traction system and the resulting model is compared with other previously published three-mass locomotive traction system models.

The last, but most important, element of the traction power transmission system is the wheel-rail contact. This thesis presents currently widely accepted model of the adhesion characteristics on the wheel-rail contact. This model is based on Kalker's linear creep theory and has been further adapted by various authors to better match empirical data.

The "*zebra*" method is described in detail and is utilized to obtain the wheel speed data needed to perform the analysis, including the "*autocorrelation*" method of data processing. The data obtained were also used to create a mathematical model of traction power transmission from traction machine to the wheelset. Some of the developed measurement methods are generally usable and can be deployed on both current and new locomotives to increase control accuracy.

Multiple problems have been identified that cause the suboptimal operation of the slip regulator of the Škoda 93E locomotive and solutions that do not require any mechanical intervention to the design of the current locomotive has been proposed. Some problems that have been identified by studying the model can be generalized to other types of locomotives.

Keywords: FPGA, adhesion, wheel speed measurement

Abstrakt

Práce se zabývá přenosem trakční síly z hnacího vozidla na vlak a prezentuje analýzu současného stavu fungování skluzového regulátoru na těžké nákladní lokomotivě Škoda III. generace, továrního označení 93E.

Při získávání, zpracování a záznamu potřebných dat bylo nezbytné použít technologii hradlových polí (FPGA). Úvodní část práce je úvodem do problematiky použití hradlových polí a stručně shrnuje historii těchto integrovaných obvodů.

Základními prvky v systému přenosu trakčního výkonu je trakční motor, mechanická soustava trakční motor-dvojkolí a její rotační hmoty a styk kolo-kolejnice.

Z pohledu trakčního motoru a jeho regulátoru byla provedena analýza vlivu trakčního motoru a buzení na tlumení kmitů mechanické soustavy.

Nejrozsáhlejší část práce se zabývá tříhmotovým modelem mechanické soustavy trakční motor-dvojkolí a vlivu jeho vlastností na adhezní vlastnosti lokomotivy. Parametry modelu byly získány analýzou změřených rychlostních dat a model je konfrontován s jinými dříve publikovanými tříhmotovými modely pohonu lokomotiv.

Posledním, avšak nejvíce důležitým, článkem přenosu trakční síly z hnacího vozidla na vlak je styk kolo-kolejnice. V této práci je nejprve prezentován současný široce akceptovaný model adhezního součinitele na styku kolo-kolejnice. Tento model je založený na Kalkerově teorii lineárního tečení, avšak byl dále upraven různými autory, aby lépe odpovídal empirickým datům.

Podrobně je popsána metodika „*zebra*“ pro získání přesné informace o rychlosti otáčení kol soukolí, která byla potřebná pro provedení analýzy včetně metodiky „*autokorelace*“ zpracování dat. Získaná data byla také použita pro vytvoření matematického modelu přenosu výkonu z trakčního motoru na dvojkolí. Některé části vyvinuté metody měření jsou obecně použitelné a lze je nasadit na současných i nových lokomotivách pro zvýšení přesnosti regulace.

Byly identifikovány vícečetné problémy způsobující neoptimální funkci skluzového regulátoru zkoumané lokomotivy Škoda 93E a byly navrženy možnosti řešení, které nevyžadují žádný mechanický zásah do konstrukce současné lokomotivy. Některé problémy,

které byly identifikovány na základě studia modelu lze generalizovat i na jiné typy lokomotiv, než je zkoumaná lokomotiva.

Klíčová slova: FPGA, adheze, měření rychlosti otáčení kol

Table of Contents

1. List of Symbols and Abbreviations....14
2. Introduction....18
2.1 The Locomotive....18
2.2 The Goals of the Thesis....19
3. Introduction to the Field....21
3.1 Introduction to the FPGA....21
3.2 Structure of Modern FPGA....22
3.3 Possibilities and Drawbacks of FPGAs....24
3.4 Interaction of DSP and FPGA....26
3.5 Wheel Slip in Railway Traction....29
3.6 Re-adhesion Control....32
3.7 Theoretical Adhesion Characteristics and Experimental Verification....33
4. High Precision Data Acquisition....36
4.1 Previously Published Wheel Speed Measurements....36
4.2 Initial Wheel Slip Speed Evaluation....39
4.3 The Zebra Method....41
4.4 Encoder Autocorrelation Method....46
4.5 Data Acquisition and Record Utilizing FPGA....51
4.6 Test Run Data....53
5. Three-Mass Traction System Model....54
5.1 Zebra Method Obtained Data – Locomotive Škoda 93E....54
5.2 Zebra Method Obtained Data – Locomotive CNR HXD2....57
5.3 Three-Mass Model of Torque Transmission System....59
5.4 Identification of Three-Mass Model Parameters....63
5.5 Damping of the Three-Mass Model....66
5.6 Energy Balance and Conditions During Slippage....72
5.7 Detection of Wheelset Axle Torsional Vibrations....78
6. Conclusions....80
7. List of Used Literature....83

8. List of Author's Publications.....86
Appendix A – Schematics.....87
Appendix B – Photo Documentation.....96

List of Figures

Figure 1: Simplified structure of an island-style FPGA....23
Figure 2: Distribution of tasks between processor and logic....27
Figure 3: Software complexity consequences....28
Figure 4: To the adhesion coefficient....29
Figure 5: Simplified diagram of adhesion coefficient versus slip speed....30
Figure 6: Block schematics of simple re-adhesion controllers....32
Figure 7: Different shapes of re-adhesion traction force reduction....32
Figure 8: Distribution of normal and tangential stress in wheel-rail contact [11]....33
Figure 9: Model and measurement on Bombardier SBB 460 [11], [26]....34
Figure 10: Model and measurement on Bombardier 12X [11], [27]....34
Figure 11: Model and measurement on GM SD 45X [11], [28]....34
Figure 12: Model and measurement on Siemens Eurosprinter 127 [11], [29]....34
Figure 13: Model and measurement on Siemens S 252[11], [30]....34
Figure 14: Calculated typical adhesion coefficient [11]....35
Figure 15: Direct electrical connection to encoder signals using nested stepladder PCBs....36
Figure 16: Wheel speed during traction on HXD2C, data from locomotive computer [32]….37
Figure 17: Wheel and train speed during breaking, data from locomotive computer [31]....37
Figure 18: Comparison of obtained wheel speeds during slippage....38
Figure 19: Wheel and GPS speed difference, traction, straight track....39
Figure 20: Wheel and GPS speed difference, traction, curved track....39
Figure 21: Wheel and GPS speed difference, braking, straight track....39
Figure 22: Wheel and GPS speed difference, braking, curved track....39
Figure 23: Wheel and GPS speed difference, coasting, straight track....39
Figure 24: Wheel and GPS speed difference, coasting, curved track....39
Figure 25: The locomotive wheel with zebra encoder....42
Figure 26: The idea of zebra measurement method....42
Figure 27: Position of zebra sensor within bogie....43
Figure 28: The location of zebra sensor....43
Figure 29: Adjustment of the scan depth by angle of photodiode....44

Figure 30: The magnitude and the phase response of band-pass filter.....45
Figure 31: Captured waveforms during setting the locomotive into motion.....45
Figure 32: Typical rotary encoder signal and its properties.....47
Figure 33: The data acquired by zebra method.....48
Figure 34: Progress of relative cog error κk.....49
Figure 35: Relative cog error κk of all 100 cogs on an axle mounted encoder.....50
Figure 36: Rotary encoder raw measured and processed wheel speed.....50
Figure 37: Simplified diagram of data capture chain.....51
Figure 38: FIFO organization in 32-bit memory address space.....52
Figure 39: Raw and processed data from logic analyzer.....53
Figure 40: Magnitude response of FIR filter used for frequency isolation.....54
Figure 41: Acquired wheel speed data band-pass filtered 50-70Hz on Škoda 93E.....55
Figure 42: Acquired wheel speed data band-pass filtered 18-25Hz on Škoda 93E.....56
Figure 43: Acquired and filtered wheel speed data on CNR HXD2.....57
Figure 44: Simplified schematic of torque transmission system.....59
Figure 45:Three mass model of torque transmission system.....60
Figure 46: General three-mass model of torque transmission.....60
Figure 47: Eigenvectors of three-mass model.....65
Figure 48: Simplified diagram of electric parameters of one bogie.....66
Figure 49: Linearization of adhesion characteristics near operating point.....68
Figure 50: Eigenvalues and eigenvectors dependency on Kμ.....70
Figure 51: Eigenvector dependency on Kμ.....71
Figure 52: Voltage and currents of DC machine during slip.....72
Figure 53: Power and energies during slip.....73
Figure 54: Energy stored in rotational mass during slip.....74
Figure 55: Decomposition of traction power into parts.....76
Figure 56: Detected adhesion coefficient μ on wheel speed peak-peak amplitude.....77
Figure 57: Simulated magnitude response for different speeds.....78

List of Tables

Table 1: List of symbols....14
Table 2: List of indexes (three-mass model)....15
Table 3: Comparison of the Sigma-Delta and SAR A/D Converters....25
Table 4: Parameters of creep model identified from measurements [11]....35
Table 5: Typical parameters of creep model [11]....35
Table 6: Speed difference during various conditions without slipping....40
Table 7: Obtained properties of detected wheelset vibrations....56
Table 8: The gearbox ratio of discussed locomotives....61
Table 9: Published three-mass model parameters....62
Table 10: Measured and expected properties in relation to three-mass model....64
Table 11: Estimated model parameters of discussed locomotives....65
Table 12: Eigenvalue and eigenvector dependency on k1 and Kμ....70
Table 13: Nyquist frequency on locomotive speed....79

1. List of Symbols and Abbreviations

Symbol	Meaning	Unit	Typical value
a	Elliptical wheel-rail contact semi-major axis	mm	
$\boldsymbol{A}$	State-space representation matrix		
b	Elliptical wheel-rail contact semi-minor axis	mm	
c_x	Rotational stiffness of „x“	N·m/rad	10^6 N·m/rad
d_x	Damping of „x“	N·m·s/rad	10^2 N·m·s/rad
f	Frequency (of vibrations, ...)	Hz	52 Hz
g	Gravity of Earth	m/s^2	9.81 m/s^2
i	Imaginary unit of complex number		
i_a	DC machine armature current	A	1100 A
i_b	DC machine flux coil current	A	110 A
J_x	Moment of inertia of „x“	kg·m^2	340 kg·m^2
k_I	Machine constant	Vs/rad	50
k_A	Reduction factor of Kalker's coefficients for creep part	-	100%
k_S	Reduction factor of Kalker's coefficients for slippage part	-	40%
K_μ	Slope of adhesion characteristics expressed in torque to slip in angular units	N·m·s/rad	±15000
L_a	Total inductance of simplified armature circuit	H	21 mH
m	Mass (of locomotive, per wheelset, ...)	kg	$1.2 \cdot 10^5$ kg
M	Torque (per wheel, ...)	N·m	18.75 kN
N	Normal force (per wheel, ...)	N	100 kN
p	Gearbox ratio (1:p)	-	3.5 – 4.5
r	Wheel diameter	m	0.625 m
R_a	Total resistance of simplified armature circuit	Ω	0.1 Ω
s	Slip ratio	-	0.5%
t	Time	s	
T	Tangential force (per wheel, ...)	N	30 kN
Δv	Slip velocity	m/s	0.05 m/s

Table 1: List of symbols

Symbol	Meaning	Unit	Typical value
v_t	Train longitudinal velocity	m/s	10 m/s
v_x	Recalculated velocity of „x“	m/s	10 m/s
u_a	Armature voltage	V	1500 V
u_i	Internal back-EMF voltage	V	1500 V
w_x	Rotations per second of „x“	1/s	2.55 s^{-1}
$\boldsymbol{x}$	State-space representation state vector		
ω_x	Angular speed of „x“	rad/s	16 rad/s
φ_x	Angle of rotation of „x“	rad	
κ_k	Rotary encoder relative cog (number k) error	-	±1%
ε	Gradient of tangential stress	-	
μ	Adhesion coefficient / Friction coefficient	-	30%
μ_0	Friction coefficient at zero slip velocity	-	55%
μ_∞	Friction coefficient at infinity slip velocity	-	25%
σ	Normal stress at wheel-rail contact	N/m^2	
τ	Tangential stress at wheel-rail contact	N/m^2	
c_x, d_x, J_x, M_x, ω_x, ...	Values recalculated to the wheelset side of the gearbox		
c_x', d_x', J_x', M_x', ω_x', ...	Values recalculated to the traction motor side of the gearbox		

Table 1 (cont.): List of symbols

x	Meaning
1	Traction motor
2	Direct driven wheel
3	Indirect driven wheel
12	Gearbox / Hollow shaft / Cardan shaft
23	Wheelset axle

Table 2: List of indexes (three-mass model)

List of abbreviations

ACIM **AC Induction Machine.** A machine where power to the rotor is supplied by means of electromagnetic induction. To generate a torque, the machine must always work with a slip.

ADC **Analog to Digital Converter.** A device used for conversion of continuous quantity of analog signal to discrete time representation in digital form. Can be a standalone integrated circuit or part of a larger integrated circuit, like micro-controller.

ALU **Arithmetic Logic Unit.** Digital circuit that performs binary arithmetic operations.

CLB **Configurable Logic Block.** The basic building block of a FPGA. Structure of CLB evolved from one LUT and flip-flop to more complicated structures, but main part of CLB still remains one or more LUTs and flip-flop.

CPLD **Complex Programmable Logic Device.** A digital integrated circuit with similar capabilities as FPGA, but logic functions are constructed instead of LUTs using sum of products.

CPU **Central Processing Unit.** Digital circuit the carries out instructions of a program.

DMA **Direct Memory Access.** Method how to access contents of RAM by a hardware without intervention of CPU.

DSP **Digital Signal Processor.** A microprocessor with an architecture optimized for high computational power.

FPGA **Field Programmable Gate Array.** A digital integrated circuit designed to be configured by a designer after manufacturing.

FPU **Floating-point Unit.** Part of computer which carries out operations on floating point numbers.

GPU **Graphics Processing Unit.** Specialized circuit designed to accelerate manipulation with images. Can be used as a vector co-processor.

MPSoC **Multi-processor System on a Chip.** A SoC design with multiple processor cores.

PI, PID **Proportional-Integral(-Derivative) Controller.** The widely used type of closed loop controller.

PIN **P-Intrinsic-N (e. g. photodiode).** PIN Photodiode with large undoped (intrinsic) region among p-type and n-type doped semiconductor regions.

RAM **Random Access Memory.** Generic type of computer memory which can be written to and read from.

RS-422 Technical standard specifying electrical differential digital signaling over twisted pair, up to 1500 meters or 10 Mbit/s (not at the same time).

SAR ADC **Successive Approximation Register ADC.** An analog-to-digital converter that converts analog signal by means of binary search through all possible quantization levels.

Sepex **Separately Excited (field coil) DC machine.** Type of DC motor where field coil current is controlled independently on the armature coil current.

SoC **System on a Chip.** An electronic design which integrates all components of a computer system on chip (frequent exception are memories).

2. Introduction

2.1 The Locomotive

The Czech Republic largest and most important manufacturer of locomotives, Škoda Transportation, has delivered in 1994 four prototypes of electric locomotive designation number 93E (class 184), initially on demand of the national railway operator. The worsening economic situation of then Czech Republic stood behind suppliers chain disintegration, cancellation of the order and stopping of further development without delivery of more units. Four manufactured prototypes remained without functioning locomotive computer.

The construction and mechanical parts of the locomotive were widely reused from so called II. generation of Škoda locomotives and in many aspects the construction resembles successful locomotives designation number 69E/71E (class 163/363). The arrangement of bogies is quite unusual: six axles on three bogies, Bo'Bo'Bo', the middle bogie is sliding in curves to the sides.

A small and progressive team of rolling stock enthusiasts built the locomotive computer and breathed life into the locomotive. Thanks to this, the locomotive computer also incorporated the state-of-the-art technologies, namely the Škoda 93E carries the first locomotive computer manufactured in the Czech Republic which used the Field Programmable Gate Array (FPGA) circuits. The Field Programmable Gate Array circuit was configured by RNDr. Bedřich Pola, my future employer.

Despite the locomotive was initially projected as universal and express train locomotive with top speed 155 km/h, the final assignment at the mining company Severočeské Doly is very different – the locomotive was re-geared to top speed 95 km/h and now is working as a heavy freight locomotive in slope and curve very demanding track, simply put, on the physical adhesion limits.

Coincidentally, at the time of finishing my diploma thesis under supervision of Ing. Jiří Zděnek, CSc., I was not aware that Ing. Zděnek actually know RNDr. Pola, my employer. When I was approached by my supervisor to help with the problem of the locomotive slip regulator, I, also rolling stock enthusiast, did not hesitate for a second. The results of the analysis are presented in this doctoral thesis.

2.2 The Goals of the Thesis

The goals of this doctoral thesis are expressed in the following points:

1. To analyze slip velocity and adhesion characteristics
    - There is a disagreement between the theory (derived from tribology) and the means how the locomotive designers understand the adhesion theory, how to control the locomotive traction system and to maximize the adhesion. The disagreement is so deep that there is even disagreement about basic properties of the wanted operating point of the traction vehicle. Therefore the actual properties of the adhesion and adhesion characteristics are analyzed in connection with the investigated locomotive.
2. To analyze the speed measurement method and to propose improvements
    - It was suggested that higher resolution of wheel speed measurement will improve the quality of slip regulation (assuming that concrete slip is the desired operation point of slip regulator).
3. To analyze the traction force transmission from traction machine to the wheel-rail contact
    - Generally speaking, there is always rotary encoder mounted on some rotational part of the transmission system to measure the axle speed. The rotation encoder can be mounted on the traction machine or near one wheel of the wheelset. The adhesion depends on wheel-rail contact, but in either method, neither or only one wheel speed is measured directly. The remaining wheel speed(s) can be derived from mathematical model.

4. To analyze the conditions during slippage
    - Important question is the required response time of slip regulator. This is closely related to the question of energy distribution during slippage – what amount of energy is stored in surplus kinetic energy of the rotational mass. The required response time can be determined by defining the maximum amount of slip (velocity) regulatory deviation and knowledge of amount of energy being stored into rotational mass during slippage.
5. To analyze slip regulator and propose possible improvements
    - The basic goal of the analysis is determination of a set of measures that can be done to improve the slip regulator and overall adhesion utilization of the locomotive.

3. Introduction to the Field

3.1 Introduction to the FPGA

The Field Programmable Gate Arrays (FPGA) are, as the name suggests, logic devices into which logical functions can be loaded and the FPGA will then execute the desired logical functions. The loading process is called *configuration* of the FPGA. The binary information fed into the FPGA is much like a program in a processor, therefore can be considered as a software and is called *configuration bitstream*. The bitstream is produced by a process called *place and route*, a process which is much like a compiler in the area of processors. The place and route is provided by vendor of the FPGA. An academic place and route exists for a generic island-style FPGA [1].

Popularity of the FPGAs among developers is gaining, particularly with the rapid development of information technologies and amount of processed data. By the essence of logical devices, the FPGA can handle much more data in comparison to a classic processor, because the FPGA can very effectively process the data in parallel and in vectors (the design of the pipelines is fully under control of the designer). One particular FPGA device can process small amount of data in a very complex way, but also can process vast amount of data in a simple way and both cases can occur simultaneously in one device. Such process is poorly achievable with a microcontroller or even a digital signal processor. Digital signal processor cannot run at higher frequency sacrificing more complex instructions at the expense of the simple instructions. The scalability of the FPGAs is not attainable by microcontrollers or signal processors. Vector data processing is possible with high-end DSPs or even standard PC processors, using popular SIMD instructions [2], but developer is always constrained by resources of the given processor and therefore the processor is either complex (and expensive) or is highly adapted to the particular application.

Commercial applications are manufactured in large series and signal processors can be developed for a given application (for example graphic processors for smart phones or PC)[1]

1 Specialized processors, Graphic Processing Units (GPUs), are powerful vector processors incorporated in virtually any PC. The opportunity to use this computational power to be employed in scientific research is followed by group General-Purpose Computation on Graphics Hardware, www.gpgpu.org. For further comparison of GPUs vs. FPGAs I would recommend the kind reader article [4].

[3]. For special applications, which are not manufactured in large series like commercial applications (in some cases one cannot talk about series at all), the usage of FPGA comes out as much better. In the area of motor control they have their irreplaceable place.

3.2 Structure of Modern FPGA

The internal structure of programmable logic devices has been developing almost thirty years from their first introduction[2]. Today market's most used programmable devices are CPLDs and FPGAs. Complex Programmable Logic Devices (CPLDs) are in comparison with FPGAs smaller (by PCB area and number of pads), cheaper and suitable as replacement of few (at most tens of) logic integrated circuits of TTL logic family 7400. They are popular by designers as a “glue“logic. The advantages of CPLDs include:

- possibility to include many different logic functions in one device
- flash memory makes possible to correct design errors without need to correct the error directly on the PCB
- very interesting is possibility to design the PCB and the internal logic functions of the CPLD simultaneously

Island-style FPGAs have different structure than the CPLDs. They consist mainly of a matrix of Configurable Logic Blocks (CLB) interconnected by Programmable Switch Matrices (PSM) as depicted in figure 1 [5]. The structure of the CLB has been changing over years, but the common feature is programmable Look-Up Table (LUT) followed by a flip-flop. This design was verified by years of development and usage of the FPGAs. In comparison of CPLDs to FPGAs, a FPGA can hold order of magnitude more logic, but generally is also slower. Today island-style FPGAs add to the matrix structure of the CLBs also other specialized blocks, like memories, multipliers and accumulators. All these functions can also be created on the standard CLB structure, but the specialized structures holds less area and are much faster.

There are many types of the FPGAs on the market. The most important manufactures are Xilinx, Altera, Lattice and Microsemi (formerly Actel). The author of this thesis has over fifteen years of experience of developing designs using Xilinx FPGAs, therefore lot of the

2 First FPGA XC2064 was introduced by Xilinx, Inc. in 1986.

work is related to the Xilinx, but the technologies of other manufacturers on the market are very competitive and therefore the conclusions can be transformed to remaining FPGA manufacturers.

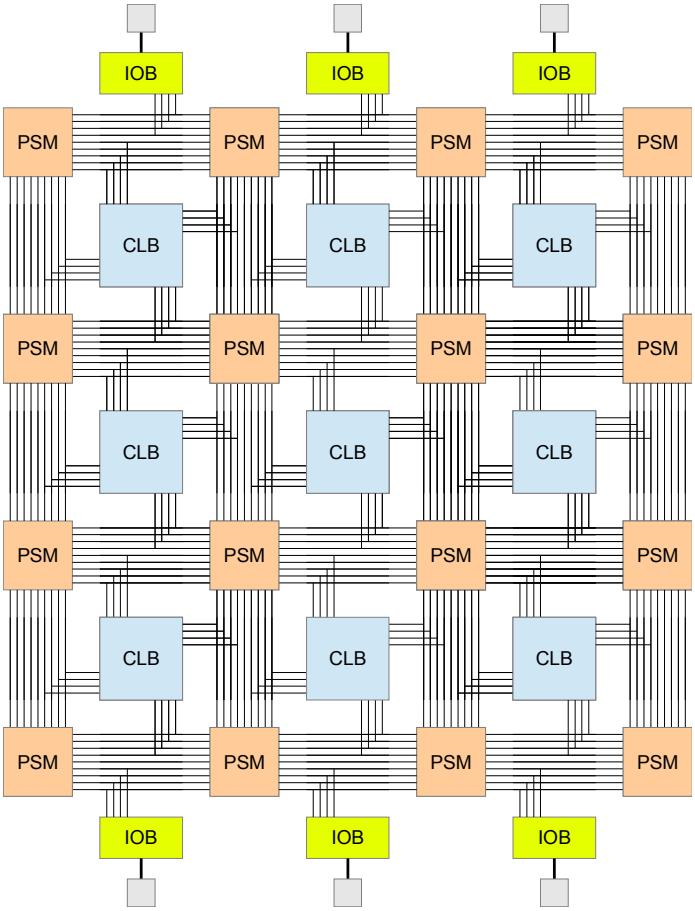

Figure 1: Simplified structure of an island-style FPGA

3.3 Possibilities and Drawbacks of FPGAs

The Field Programmable Gate Arrays are strictly digital devices and can process solely digital signals. Information exchange with the surroundings is realized by Input/Output Blocks – IOBs. The FPGAs therefore can communicate only using such resources, which are supported by the IOBs. Baseline FPGAs have capabilities to communicate using TTL and CMOS/LVCMOS logic levels and their signals are preferably synchronous (captured directly into a flip-flop). Strictly asynchronous design is not convenient to be implemented in a FPGA and therefore asynchronous inputs are possible to be captured after resynchronization. Many FPGAs can also use high-speed single ended and differential signals, like LVDS[3], SSTL[4]. High-end FPGAs have SerDes[5] units which are capable of multi-gigabit serial communication, similar to the PC buses like PCIe and SATA.

The FPGAs cannot directly interface analog signals. These must be converted using some kind of A/D converter (ADC). Such use of external converter looks like a great disadvantage over motor-control signal processors and microcontrollers. On closer examination are in fact most of the measured analog values at various different voltage domains other than the control computer and therefore the system must consist of standalone ADC with a voltage isolation barrier made of optocouplers with a serial digital communication or any other kind of galvanic isolation. The exception are popular LEM[6] sensors, which are inherently isolated up to few kilovolts [6].

3 LVDS stands for Low Voltage Differential Signaling. Popular as a high-speed replacement of RS-485 up to hundreds Mbps.

4 SSTL stands for Stub Series Terminated Logic. Popular for high-speed connections on PCB, used with DDR SDRAM.

5 SerDes stands for serialization-deserialization.

6 LEM is name of the manufacturer. The current sensors are based on sensing magnetic field around conductor. Similar products are offered also by Allegro MicroSystems, Inc.

	Successive Approximation ADC	Sigma-Delta ADC
Requires Sample-Hold	Yes	No
Slow and accurate	Yes	Yes
Continuous operation	No	Yes
Requires trigger logic	Yes	No
Requires local clock source	Yes, can be inaccurate	Yes, accurate
Fast and inaccurate	No	Yes
Requires decimation	No	Yes
Requires clock reconstruction	No	Yes
Communication over optocoupler feasible by a micro-controller	Yes	No

Table 3: Comparison of the Sigma-Delta and SAR A/D Converters

Very advantageous is usage of analog sigma-delta converters. For a given value, the regulator often requires highly accurate information, but the update rate, or bandwidth, of this information is not required to be very high. In contrast, the fault detection circuit or the sign detection in a matrix converter [7] is not required to be precise, but is required to be very fast. The comparison of the SAR ADC and Σ-Δ ADC is in table 3. Using the Σ-Δ converter both fast inaccurate and slower accurate information about value can be transmitted over just one digital line (e. g. optic wire or optocoupler). For such reception a clock reconstruction unit and a decimation unit are required and these units are easily implemented in the FPGA structure. In comparison to the common SAR ADC & comparator solution, up to three digital lines will be required – one for asynchronous digital data, one for fast comparator data and one for trigger of the conversion (the conversion takes significant amount of time and it may be required to synchronize start of the conversion of all converters in the system to start them simultaneously and to align the conversion within the switching period).

3.4 Interaction of DSP and FPGA

Modern regulation structures of electric drives often incorporates a FPGA. The FPGA is responsible of the fault detection and in more complicated designs also of the signal generation and communication with sensors and other devices. The design has more emphasis on the fault detection (common to high-power designs with more expensive switching devices) the usage of FPGA is more common. In most cases, especially because of former lack of computational power of the FPGAs, the system is designed as a combination of a digital signal processor (DSP) and a FPGA attached to it. The FPGA was then responsible of the communication tasks, including pulse generation for switching devices, the sensor data reception and the fault detection, while the DSP was responsible of the computational tasks.

The communication between the FPGA and the DSP is conform to the DSP requirements, because the FPGAs are more flexible in this task. The common solution is to attach the FPGA to a common external bus of the DSP and the bus architecture is often a well known legacy bus in an 8086 (“Intel-style” bus) or a 68000 (“Motorola-style” bus) style, or for higher throughput a synchronous bus.

The requirements for data rates between the FPGA and the DSP can be demanding and software model is often designed that the FPGA is mapped into the memory area of the DSP and acts like a peripheral of the processor.

In the last ten years the speeds and sizes of the FPGAs gained such level, that a simple controller and arithmetical logical units were feasible to be implemented easily in a FPGA. For a modern low-end FPGA[7] is implementation of controller of simple 8-bit micro-controller negligible [8].

The control of a modern electric drive is not possible without processor and software equipment. Especially, solution of the tasks like starting, error handling, marginal situations and communication with higher level system using hard-wired (meant hard-wired in the FPGA) controller is possible only with difficulties. Every such solution leads inevitably to

7 The smallest member of the Spartan-3 family of FPGAs, XC3S50A-4VQG100C costs about $6 per one piece.

a microcode controller and there is a very small step from microcode controller to a real processor with software equipment.

In the FPGA it is possible to implement a more complicated controller, like a controller of a mid-range digital signal processor. The DSP, which is integral part of the FPGA can handle all the tasks which would be handled by a DSP in a dual system consisting of a standalone DSP and a FPGA.

The task of controlling frequency converter with all associated sub-tasks is very complex and extensive. The developer of the system has much possibilities where to lead the cut of division of the task between the DSP part (a software) and the FPGA part (logical functions) as shown on figure 2. A system, which is exclusively running within a single chip (the FPGA) is called System on a chip (SoC).

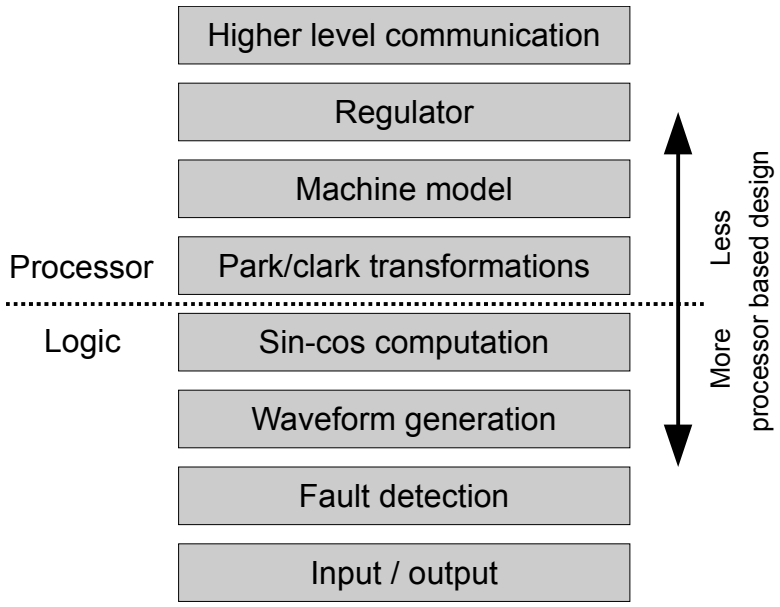

Figure 2: Distribution of tasks between processor and logic

The design of a suitable processor core for FPGA is a complicated task and the requirements for the core must be stated as a first step of the development. The complexity of the processor core depends on the decision where to lead the cut between the tasks. Because the FPGA is not limited to use only one processor core, but may contain several independent cores, it may be even more advantageous to divide the tasks between even more parts and use two or more, less powerful and complicated processor cores, instead of one. Such system, which uses more than one processor core is called a multi-processor system on a chip (MPSoC) [9].

The main reason to divide the task between two processor cores are the completely contradictory demands of the regulation task and the communication task, especially when communication incorporates very advanced methods like TCP/IP [10].

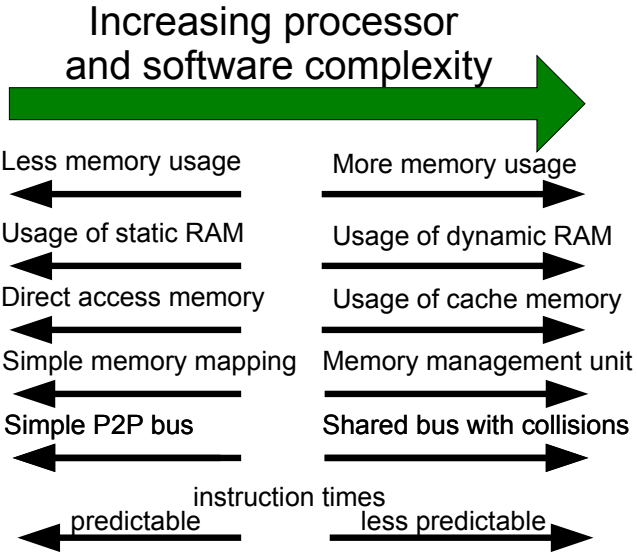

Figure 3: Software complexity consequences

The key factors for taking into consideration with processor complexity and size are:

- Instruction time predictability. Very fast regulation loops have to have given maximum computational time of one loop.
- Requirement for more or less powerful arithmetical-logical unit (ALU). More extensive ALU can run at lower clock frequency[8].
- Requirement for data throughput of peripherals and priority order, usage of direct memory access (DMA).
- Memory requirements on amount and access times, usage of cache memories[9].
- Floating-point unit (FPU) and implementation of the control algorithm in floating-point or fixed-point arithmetic (FPU consumes large number of resources, but development is faster and straightforward)[10].

8 One FPGA can have several clock domains.

9 Cache memories may introduce a chaotic behavior into the system. A small relocation of core or data in the memory can cause large differences in execution time.

10 Usage of Floating-Point arithmetic in area of electric drive control is avoidable by proper selection of units.

3.5 Wheel Slip in Railway Traction

The purpose of the electric drive control is to dynamically change given torque by the demand of the higher level system. Thanks to great variability of the electric machines and possible kinds of generation of torque in them exists plentiful means of regulation of the electric drives. These method differs by used electric machine as well as application, required scale of the regulation, efficiency of the regulation, used regulation element and demands on amount and accuracy of the measured readings of the electric machine and last but not least required computational power and algorithmic complexity of the control system.

One of the most important fields of advanced electric drives is railway traction. The usage of FPGAs in this field is advantageous and irreplaceable since 1990s[11]. The railway traction system includes wide range of subsystems. The subsystems of a railway traction system where FPGAs are advantageous are wheel speed sensors, voltage and current sensors in the voltage inverter, the inverter controller itself, communication circuits and also user interaction equipment like display and keyboard drivers.

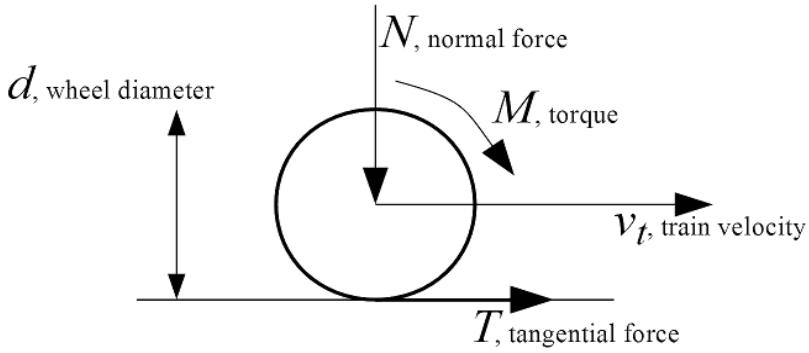

Figure 4: To the adhesion coefficient

Among issues that need to be addressed in the railway traction is railway wheel slip during torque transmission and wheel anti-slip control. The wheel anti-slip control is essential in modern railway traction vehicle.

According to Kalker and other published papers [11, 12, 13], the railway vehicle always shows a slip (creep) which is dependent on the traction force.

11 The first locomotive designed in the Czech Republic with use of FPGAs in traction computer was Škoda 93E, delivered in 1994. Coincidentally, this is the locomotive which this thesis concerns with.

The adhesion coefficient μ is

$$\mu = \frac{T}{N} \quad , \tag{1}$$

where T is tangential force and N is normal force according to the figure 4.

The slip velocity is Δv defined as

$$\Delta v = v_w - v_t \quad , \tag{2}$$

where v_w is peripheral speed of wheel and v_t is train velocity.

The adhesion coefficient μ is dependent on the slip speed, weather, dirt and other conditions (see figure 5).

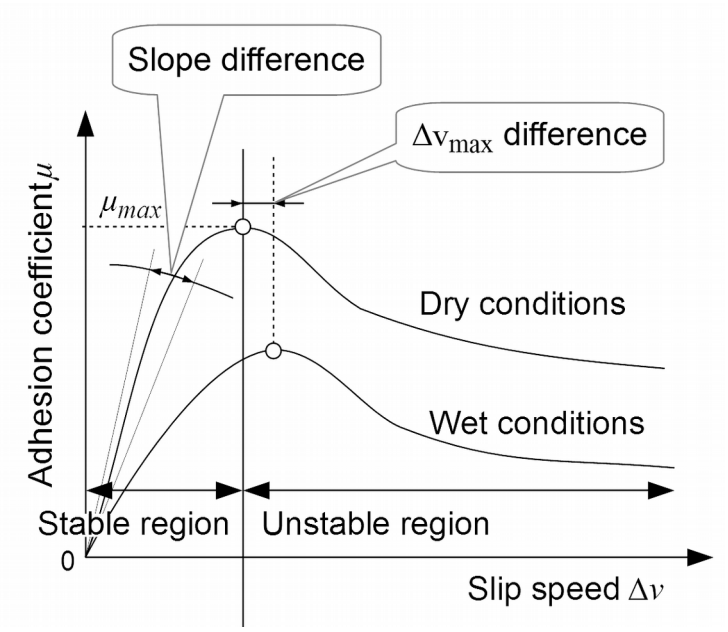

Figure 5: Simplified diagram of adhesion coefficient versus slip speed

The task of the wheel-slip controller of traction vehicle is divided into two main problems:

1. Detect slip and implement re-adhesion control (regain adhesion)
2. Find the optimal (maximum) adhesion coefficient and operate at this point.

Several methods how to detect slip have been published, either with output as a binary function or as the slip ratio or the slip velocity (difference between vehicle speed and peripheral speed of wheel) and these methods include:

- difference between speed of two or more axles (and similar methods, like observation of voltage or current differences between traction motors) [14]
- acceleration of wheelset axle [15, 16]
- comparison of wheel speed acceleration with output from accelerometers [17]
- vehicle ground speed detection using GPS, ground radar or non-powered freely rotating wheel [18, 19]
- detection of vibration and resonance phenomenons on bogie [20, 21]

It should be emphasized that the conditions below each wheel of the traction vehicle can be different, for example when the vehicle is crossing only small obstacles, like wet leaves fallen on the rails.

In some weather conditions the maximum of adhesion coefficient may not be expressed at all [22] and therefore the algorithms for searching for them must expect also this possibility.

3.6 Re-adhesion Control

Quite simple re-adhesion control can be utilized by detection of wheel acceleration or by comparing vehicle and wheel speeds. The block schematics of these controllers is depicted in figure 6. After reaching a threshold value of the acceleration or the speed difference, the traction force is lowered by a predefined value ΔF. The controller must be independent for each axle.

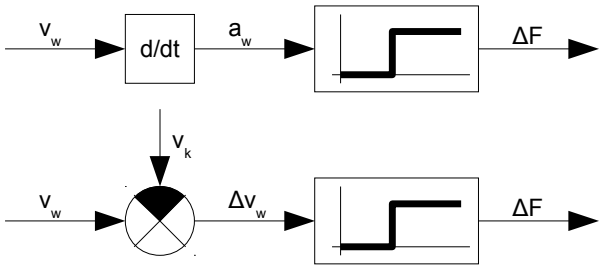

Figure 6: Block schematics of simple re-adhesion controllers

The actual shape of reduction of traction force can be different. Some of these shapes are depicted in figure 7.

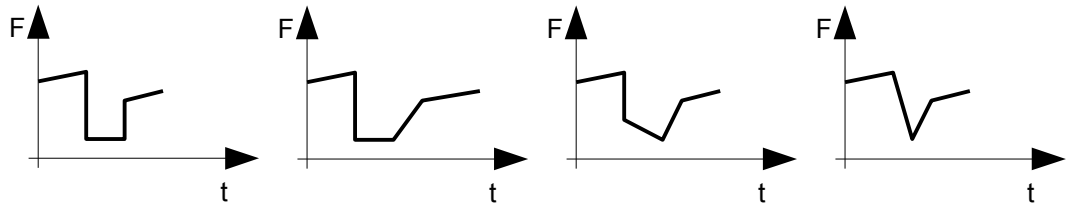

Figure 7: Different shapes of re-adhesion traction force reduction

The common property to all shapes is that new traction force must be lower on the end of the anti-slip controller intervention than on its start. The simple controllers depicted on the figure 6 and 7 are not sufficient for a real life traction vehicle, therefore a more sophisticated regulators are being tested and developed [23].

3.7 Theoretical Adhesion Characteristics and Experimental Verification

According to [11, 12] the wheel-rail contact area can be estimated as elliptical with half-axes a, b and normal stress σ distribution according to Hertz. The tangential stress τ in the Polách method caused by traction can be seen in figure 8. The maximum value of tangential stress at any point is $\tau_{max} = \mu \cdot \sigma$, where μ is friction coefficient.

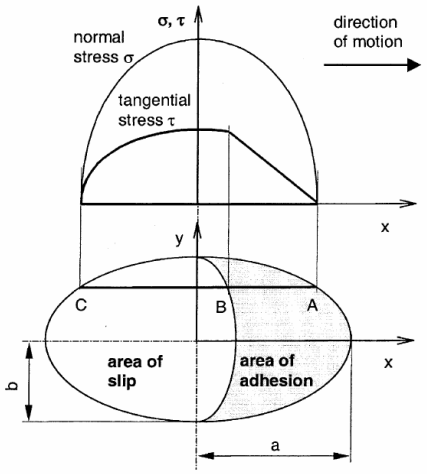

Figure 8: Distribution of normal and tangential stress in wheel-rail contact [11]

The solution is described in [12] and according to [11] it is

$$T = \frac{2N\mu}{\pi}\left(\frac{k_A \varepsilon}{1+(k_A \varepsilon)^2} + \arctan(k_S \varepsilon)\right) \quad , \tag{3}$$

where

$$\varepsilon = \frac{2}{3}\frac{C\pi a^2 b}{N\mu} s \tag{4}$$

and C is proportionality coefficient characterizing the contact shear stiffness [N/m^3] and can be derived from [24] and s is slip ratio in longitudinal direction, neglecting tangential slip and spin. The coefficients k_A and k_S are introduced in [11] to better fit the theoretical values with wet and polluted conditions. The coefficient k_A introduce lower slope than expected by theory in creep mode (initial linear part of the adhesion characteristics) and coefficient k_S introduce change of Karker's coefficient in slippage area.

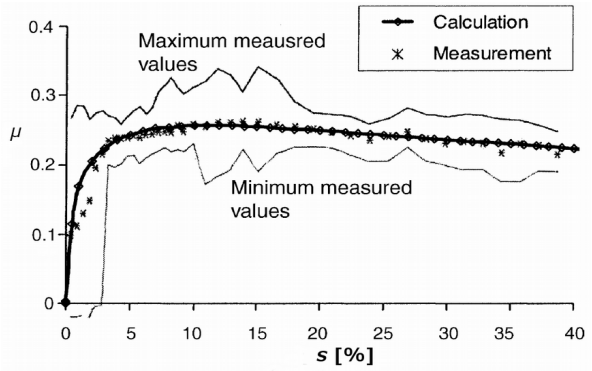

Figure 9: Model and measurement on Bombardier SBB 460 [11], [26]

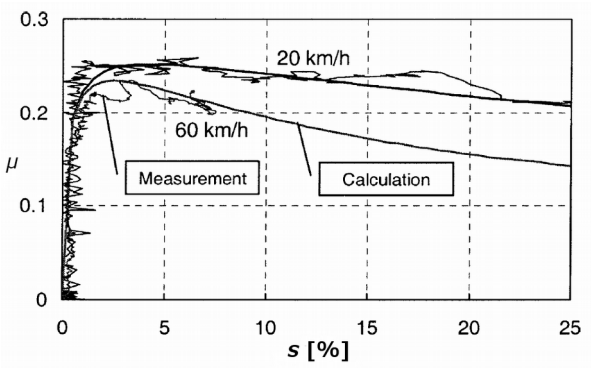

Figure 10: Model and measurement on Bombardier 12X [11], [27]

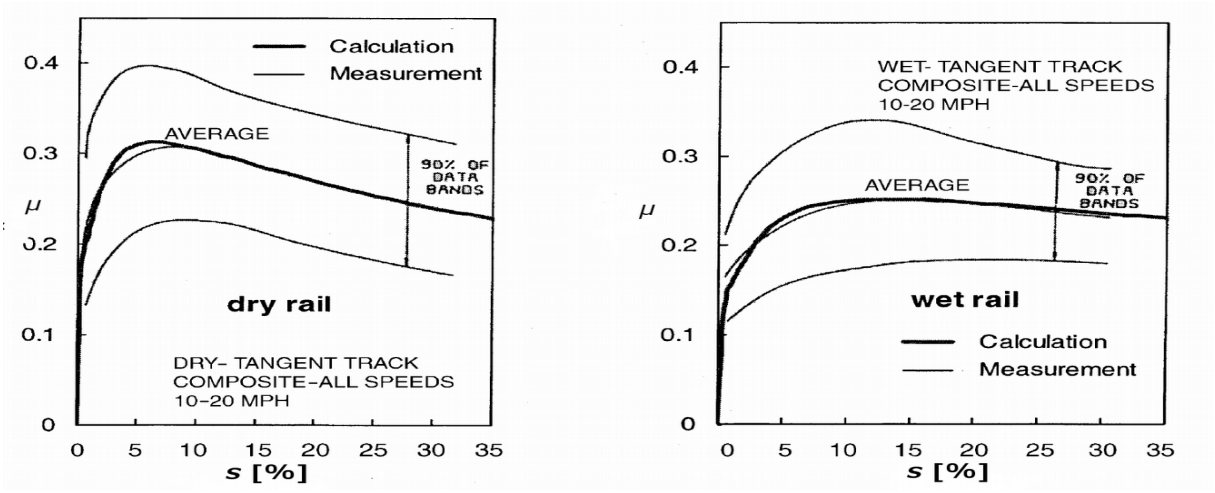

Figure 11: Model and measurement on GM SD 45X [11], [28]

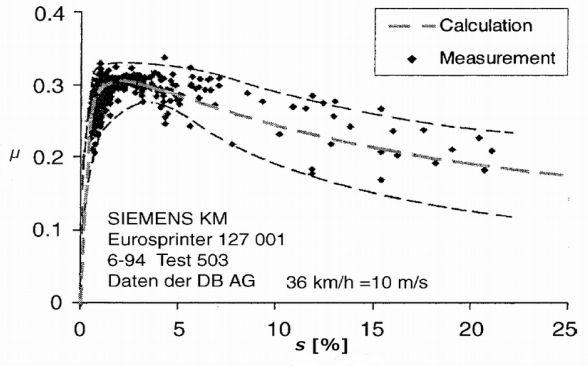

Figure 12: Model and measurement on Siemens Eurosprinter 127 [11], [29]

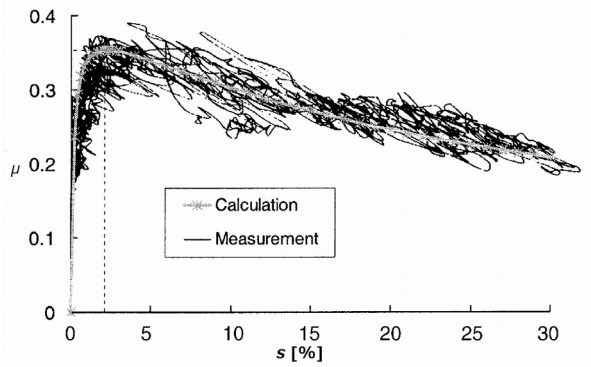

Figure 13: Model and measurement on Siemens S 252[11], [30]

The variable friction coefficient μ can be expressed according to [25] as

$$\mu = \mu_0 \left[(1 - A) e^{-B \Delta v} + A \right] \quad , \tag{5}$$

where A is the ratio between limit of friction coefficient at infinity slip and maximum friction coefficient

$$A = \frac{\mu_\infty}{\mu_0} \quad . \tag{6}$$

Polách has gathered in [11] data from set of measurements from recent years and fitted the measured data with the model by adjusting the model parameters.

Each figure 9-13 has measurement data and fitted calculated data according to the model using parameters listed in table 4.

Locomotive	SBB 460	12X	SD45X	SD45X	DB127	S252
Rail conditions	Wet	Wet	Wet	Dry	Dry	Dry
Speed [km/h]	40	20 and 60	16-32	16-32	36	30
Reference	[26]	[27]	[28]	[28]	[29]	[30]
Figure	9	10	11	11	12	13
Model parameter k_A	0.16	0.65	0.29	0.68	0.72	1.00
Model parameter k_S	0.07	0.26	0.07	0.14	0.36	0.50
Model parameter μ_0	0.31	0.28	0.30	0.40	0.36	0.40
Model parameter A	0.50	0.40	0.38	0.44	0.38	0.36
Model parameter 1/B [km/h]	22.5	9.0	20	6	5.1	6.5

Table 4: Parameters of creep model identified from measurements [11]

	Dry	Wet
Model parameter k_A	1.00	0.30
Model parameter k_S	0.40	0.10
Model parameter μ_0	0.55	0.30
Model parameter A	0.40	0.40
Model parameter 1/B [km/h]	6	18

Table 5: Typical parameters of creep model [11]

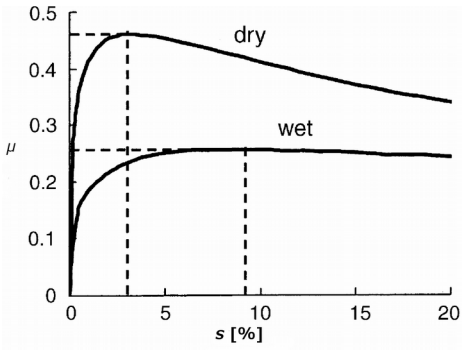

Figure 14: Calculated typical adhesion coefficient [11]

Table 5 and figure 14 contains identified typical parameters of adhesion force creep model according to [11].

4. High Precision Data Acquisition

4.1 Previously Published Wheel Speed Measurements

When evaluating adhesion characteristics, relative slip or slip speed, it is always necessary to evaluate longitudinal speed of locomotive frame (which is related to train speed) and peripheral speed of all wheels. The train speed can be, for testing purposes, easily ascertainted using GPS or Doppler radar. The rotational speed of locomotive wheels can be measured using rotary incremental encoders either directly mounted on wheelset axle (before gearbox) or on traction machine (behind gearbox). The encoder data can be obtained directly on encoder connector or the data can be received from locomotive computer after their initial processing. Many papers were published about evaluation of wheel speed, slip speed or identification of adhesion characteristics [11, 26, 27, 28, 29, 30, 31].

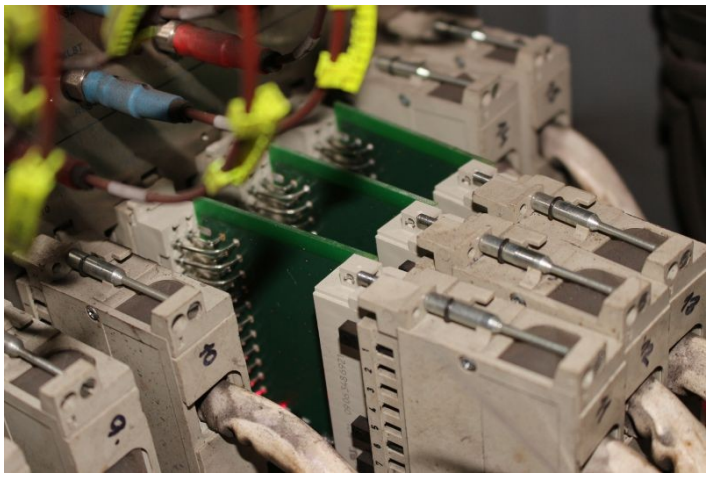

Figure 15: Direct electrical connection to encoder signals using nested stepladder PCBs

During evaluation of either independent rotary encoders installed on the locomotive only for the purpose of measuring during test run or using signals from already mounted rotary encoders it is necessary to care about the analysis of systematic and random measurement errors. Further text assumes usage only of digital encoder signals with one to three channels.

Very few studies deal with the verification of rotary encoders placement correctness and methods of the encoder signal sampling. Rare exception is Malvezzi paper [31], where she describes detailed information about communication with the locomotive computer and states that the computer obtains the data from rotary encoder and the information is transferred once per 2.4 ms (approx. 417 Hz). There is no further detailed information about the locomotive or

how the computer acquires the encoder data (at least whether the computer samples the speed with the same period and if not, what happens with "lost" samples). The author states in the paper that the wheel speed data contain considerable noise and therefore they are further filtered with low-pass filter with critical frequency 4 Hz. The obtained data are presented in figure 17. Therefore there cannot be dispelled doubts that Nyquist sampling theorem criterion is not met. Mirroring frequencies may show up as random noise and therefore authors are forced to significantly reduce the signal bandwidth to reduce the noise. The available bandwidth is far below the expected torsional vibrations of the torque transmission system.

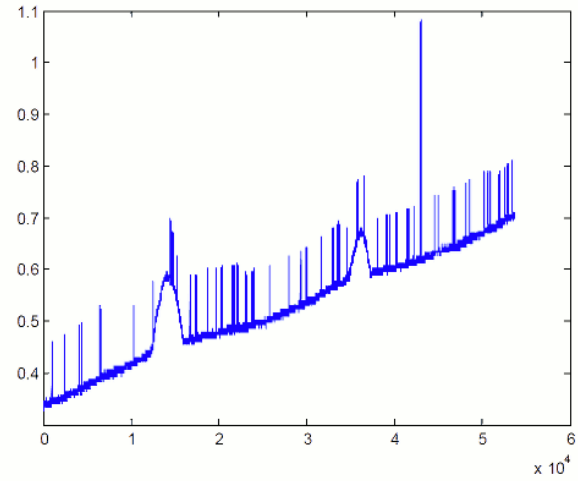

Figure 16: Wheel speed during traction on HXD2C, data from locomotive computer [32] The scale of axis are not documented

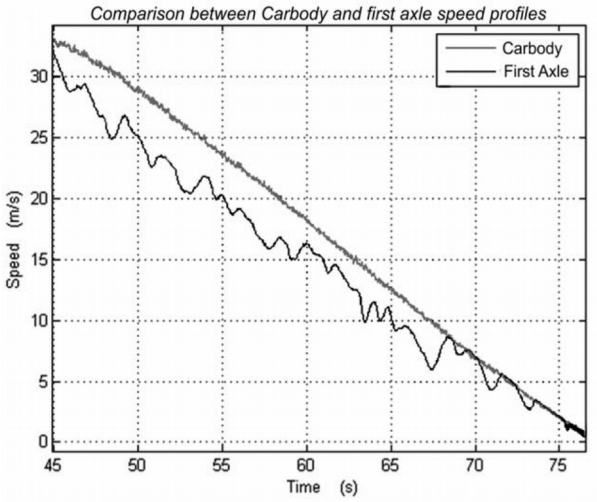

Figure 17: Wheel and train speed during breaking, data from locomotive computer [31]

On some locomotives, the quality of mounting and electrical shielding and digital filtering is so badly designed, the measured speed contains obvious spurious data. The figure 16 shows data obtained by Huang [32] on CNR HXD2C (Co'Co' heavy freight locomotive). The scale of axis are not documented the by the authors. The author of this thesis is acquainted with speed data of similar locomotive CNR HXD2B and the raw data also evince the same phenomena. The phenomena was caused by a bug in locomotive computer's own speed calculation and could be fixed by simple software revision.

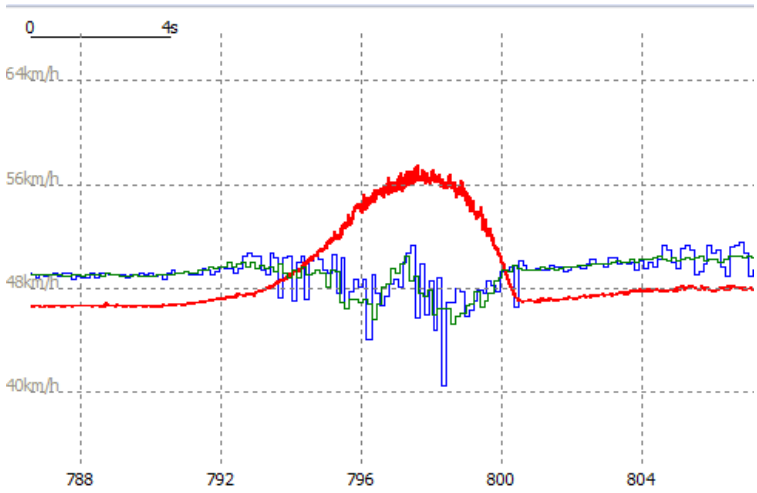

Figure 18: Comparison of obtained wheel speeds during slippage
Locomotive Škoda 93E
Red – Zebra method, low-pass filtered 11 Hz
Blue – Bogie computer data
Green – Master locomotive computer

In figure 18 is depicted comparison of data obtained by direct recording of signals from axle speed encoder obtained using stepladder PCBs (figure 15), data from bogie computer and data from master computer. The depicted data were obtained on Škoda 93E locomotive and belong to first axle (in the direction of movement). Bogie computer uses Intel 8254 peripheral circuit for encoder signal processing and communicate over RS-485 bus with master computer, which further process the data together with data from other two bogie computers. Initial DC error is caused by incorrectly set wheel diameter (due to wear from its initial diameter). The measurement algorithm utilizing Intel 8254 behaves such way the present vibrations at 52 Hz (they are filtered out on the red waveform) cause measurement errors. This can be nowadays considered as bug, but rather it demonstrates the state of available technology at early 1990s.

4.2 Initial Wheel Slip Speed Evaluation

Figures 19-24 contains measurement of GPS speed compared to measured speeds of axle 1, 3 and 5 during a test run with locomotive Škoda 93E. The test run was performed on track with light rain weather conditions.

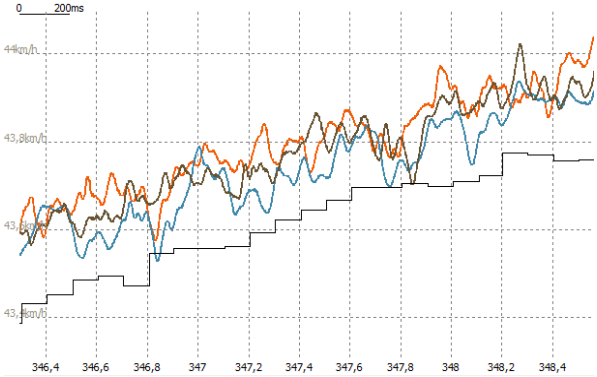

Figure 19: Wheel and GPS speed difference, traction, straight track

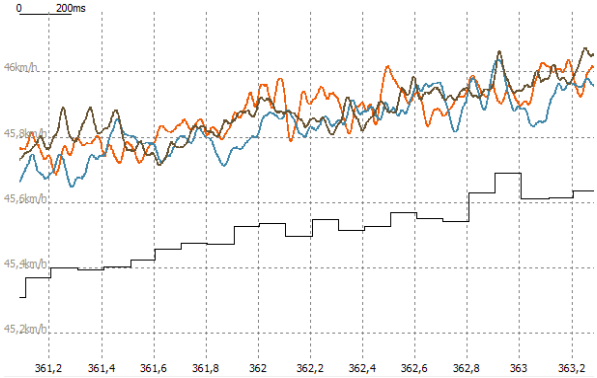

Figure 20: Wheel and GPS speed difference, traction, curved track

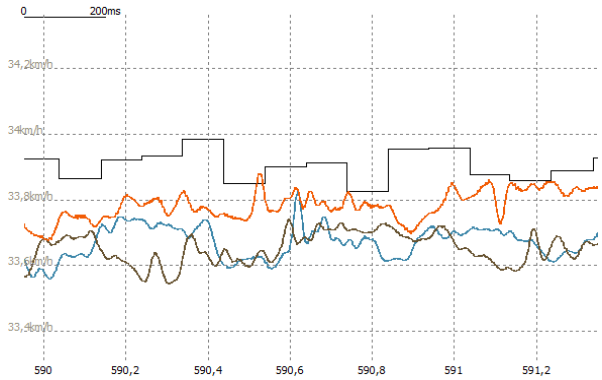

Figure 21: Wheel and GPS speed difference, braking, straight track

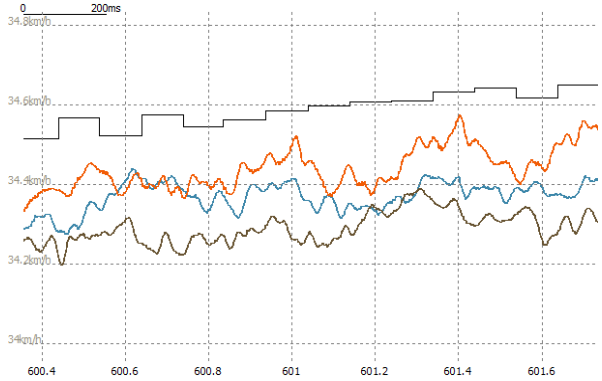

Figure 22: Wheel and GPS speed difference, braking, curved track

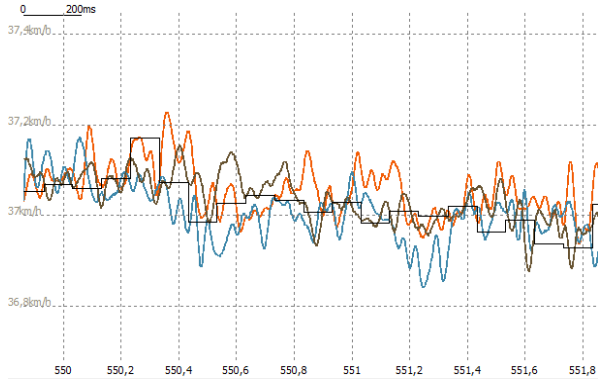

Figure 23: Wheel and GPS speed difference, coasting, straight track

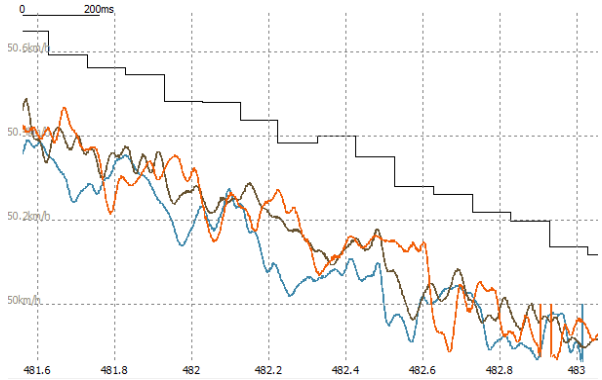

Figure 24: Wheel and GPS speed difference, coasting, curved track

Torque	Traction	Traction	Brake	Brake	Coasting	Coasting
Track	Straight	Left curve, r = 550 m	Straight	Left curve, r = 2000 m	Straight	Right curve, r = 900 m
Traction force	245 kN	245 kN	-237 kN	-237 kN	0 kN	0 kN
Figure	19	20	21	22	23	24
Time [s]	346.5-348.5	361.0-363.0	590.0-592.0	600.0-602.0	550.0-552.0	481.0-483.0
Speed v_t [km/h]	43.6	45.5	33.9	34.6	37.1	50.8
Δv axle 1 [km/h]	0.179±0.049	0.364±0.051	-0.101±0.068	-0.144±0.043	0.049±0.062	-0.238±0.081
Δv axle 3 [km/h]	0.116±0.051	0.327±0.051	-0.192±0.088	-0.213±0.040	-0.011±0.054	-0.292±0.053
Δv axle 5 [km/h]	0.155±0.042	0.361±0.049	-0.240±0.059	-0.294±0.044	0.021±0.063	-0.235±0.042
Slip ratio	0.34%	0.77%	-0.52%	-0.63%	0.05%	-0.50%

Table 6: Speed difference during various conditions without slipping

The conditions are summarized in table 6, the slip speed Δv is evaluated on 1st, 3rd and 5th axle in the direction of movement and expressed as mean value μ with standard deviation σ.

It is also important to note, that the each wheel diameter can differ.

Considering straight track with ideal conditions, there are creep ratios as expected by the Kalker's creep theory according to figure 14 (chapter 3.7), but when experiencing conditions other than ideal straight track the effect of other sources of slip speed greatly exceed the Kalker's creep speed. Therefore the typical approach of slip regulator described in chapter 3.6 and depicted in figure 6 and 7 do not work optimally and it is convenient to enhance the slip regulator.

4.3 The Zebra Method

The author of this doctoral thesis has obtained previously acquired data regarding adhesion and wheel slip. However the simulations according to the theory available in published papers gave different results than the available data – the simulation data based on published theories differ from what was measured. The very same mismatch was between published adhesion characteristics and experimentally obtained adhesion coefficients during locomotive test runs on the dry rail. During data analysis arose suspicion that the Nyquist sampling theorem criterion was not met and in connection with usage of non-linear filter the signal was irreparably damaged. To verify the suspicion and to obtain ultimately better data the author has designed and conducted unique wheel speed measurement method. The FPGA technology was used for data acquisition. This was allowed only by the state of FPGA technology that was reached in the previous 15 years.

Author designed and realized the unique measuring method of both wheels rotation speed of a wheelset simultaneously on locomotive Škoda 93E. The rotary encoder wheel was placed directly at the outer diameter of the locomotive wheel, as depicted in figure 25. Each wheel was glued and there were attached 14 self-adhesive papers previously printed with encoder pattern by laser printer. The outer border of wheel rim is distorted as the wheel diameter is progressively worn down while the locomotive runs. Therefore the adhesive stickers are made to match exactly the inner diameter of wheel rim (1080 mm) and encoder outer diameter was adjusted after attaching with razor blade. The locomotive with attached encoder resembles zebra stripes and therefore the method was nicknamed by around watching train drivers as "*zebra"* method.

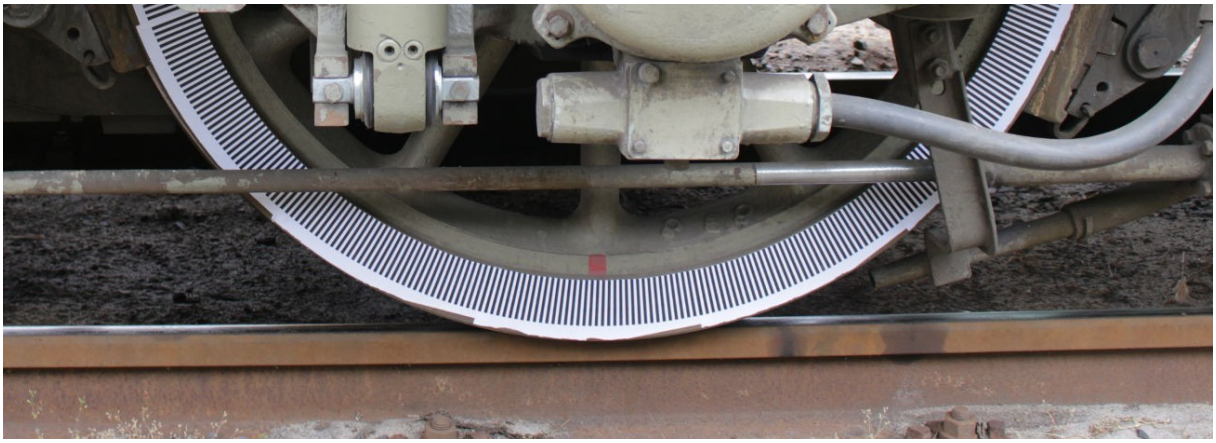

Figure 25: The locomotive wheel with zebra encoder

The basic idea of the measurement is depicted in figure 26. Current source continuously drives current through laser LED diode. The diode is aimed at the encoder pattern and it is continuously enlightened with a small dot. A PIN photodiode scans reflected light and detects transitions between dark and light places of the encoder pattern. The signal from photodiode is filtered using band-pass filter and then it is amplified and conditioned so it can be transmitted as digital signal using RS-422 physical layer over the distance to the drivers cabin. The equipment, where the signal was received, processed and recorded using FPGA based logic analyzer, was situated into drivers cabin.

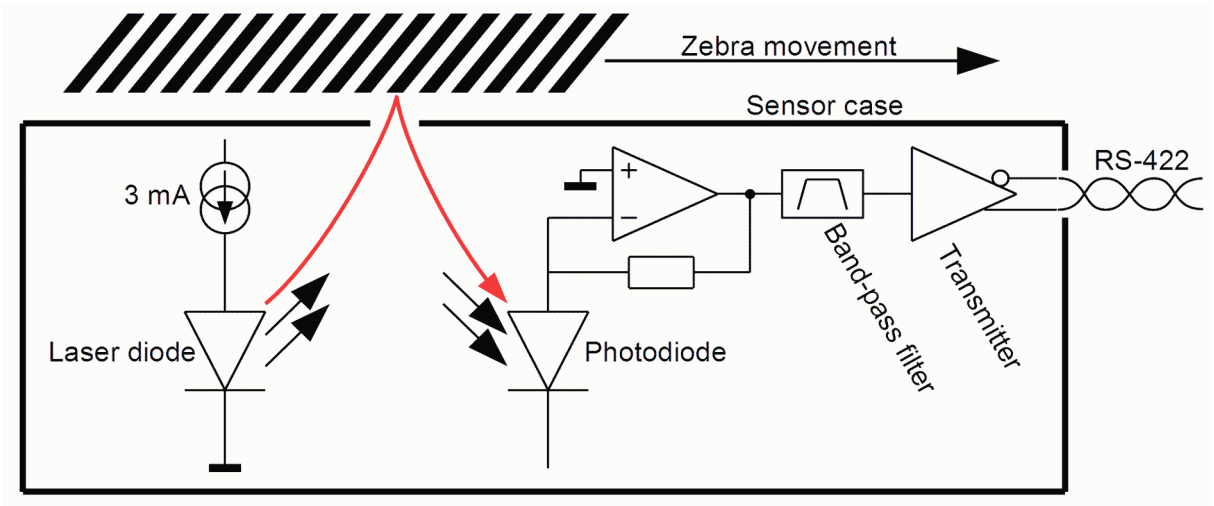

Figure 26: The idea of zebra measurement method

The placement of sensor (laser LED diode and PIN photodiode) has fundamental impact on measurement accuracy, because sensor's own movement is added to the resulting processed speed readout. Between the rotating wheel of wheel-set and the sensor must be kept minimal

distance, the sensor must be well fixed to eliminate any shift or movement and most importantly the sensor installation must not compromise safety.

For these reasons, the selected location of the sensor was at the longitudinal frame of the bogie directly above the wheelset axle. The situation is depicted in figure 27.

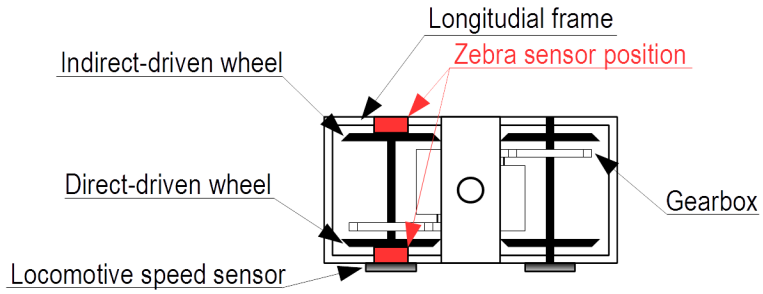

Figure 27: Position of zebra sensor within bogie

The PIN photodiode gathers also ambient light and its variance, therefore it is advantageous to place the sensor at location, which is shadowed from daylight. The upper longitudinal frame is below lower edge of the locomotive body and also the frame itself provide protection against daylight. The situation and the location of sensor is captured at figure 28.

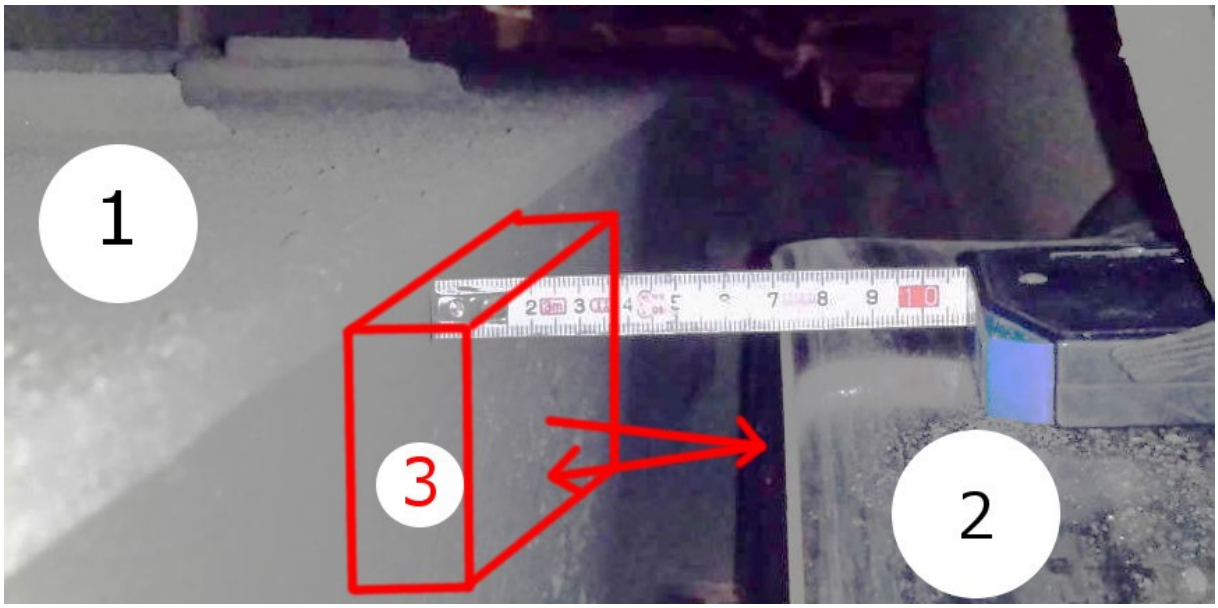

Figure 28: The location of zebra sensor
1. Longitudinal bogie frame
2. Locomotive wheel
3. Projected sensor position

In the locomotive Škoda 93E there is the space between bogie frame and wheel, including the space for the sensor itself about 7 cm (see figure 28). It is expected that the space may slightly alter during test run. The casing of the sensor itself is 3.5 cm wide

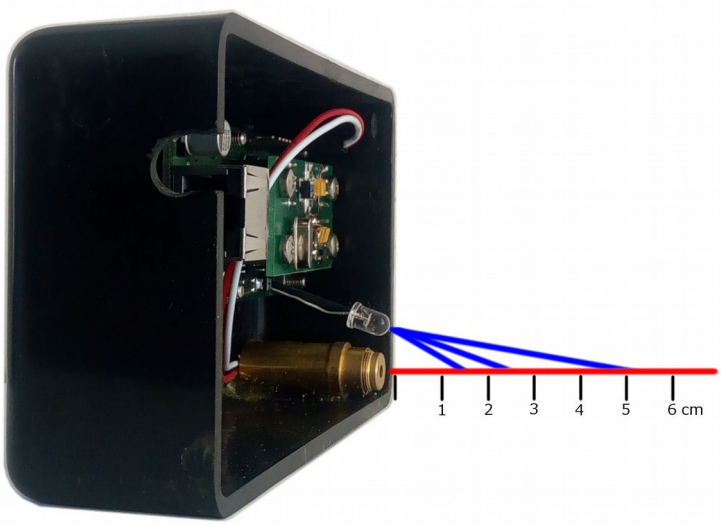

Figure 29: Adjustment of the scan depth by angle of photodiode

To further minimize influence of ambient light the selected photodiode has a very narrow field of view. Therefore it was necessary, according to figure 29, to adjust the angle of the photodiode according to the ascertained distance. The position of the photodiode is fixed by lid of the casing.

To eliminate the noise from ambient light and also the effect of electromagnetic noise generated by power electronics of the locomotive, the signal is filtered by a band-pass filter. After filtration the signal is digitized using the zero-cross comparator. The simulated magnitude and the phase response of the band-pass filter[12] is depicted in figure 30.

12 The amplitude response in the band-pass range of -20 dB is due to setup of the simulation. The exciting signal is set as PIN photodiode current of amplitude 100 nA. The magnitude response of 0 dB is voltage of 1 V at the output of the filter, at the input of comparator.

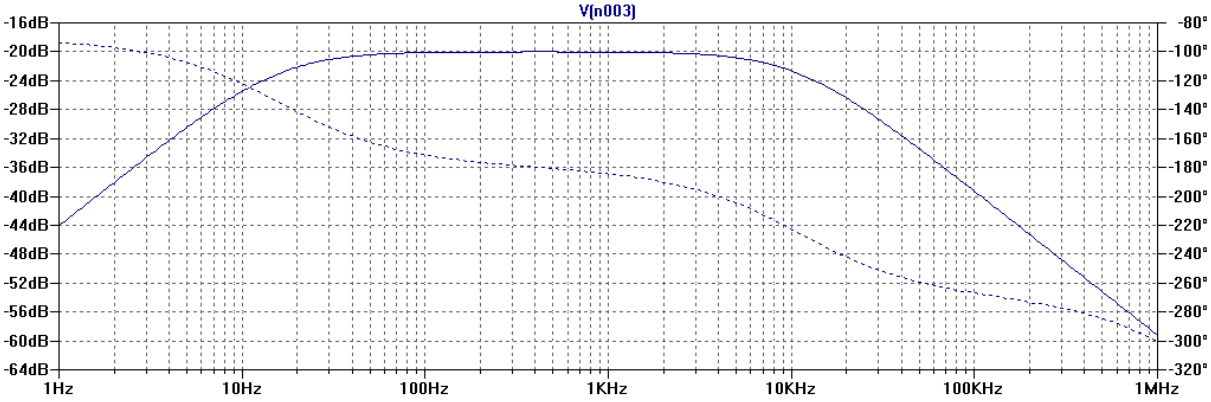

Figure 30: The magnitude and the phase response of band-pass filter

In figure 31 there is depicted waveform of received signals during setting the locomotive into motion. The waveform in the first line (Input2) is the waveform from locomotive's own speed sensor coupled with wheelset axle. The waveforms in the second and third lines (Input14 and Input16) are received from presented *zebra* method sensor. It can be seen that once the signal reaches frequency of about 5 Hz, the wanted signal dominates an unwanted noise. According to the magnitude response (figure 30) the wanted signal to noise ratio is at least 10 dB.

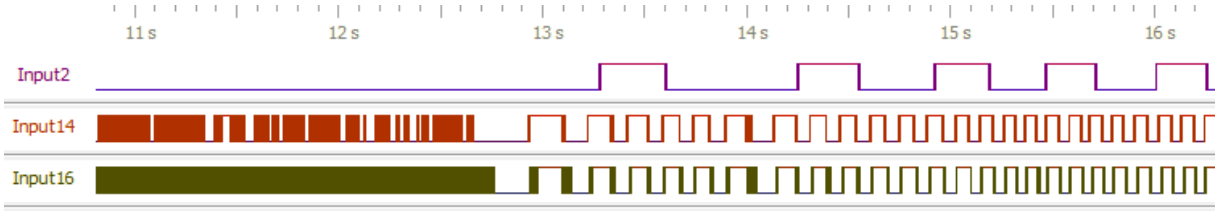

Figure 31: Captured waveforms during setting the locomotive into motion

The *zebra* encoder has more signal periods per revolution than the locomotive sensor and therefore has better resolution and sampling rate of calculated speed. The higher number of periods per revolution allowed better buffer between observed self-resonance frequencies and the Nyquist frequency. Also simultaneous continuous measurement of the encoders on both wheels of single wheelset allowed to calculate the speed of each wheel with the mutual coupling. The sensor also incorporates a three-axis accelerometer with Σ-Δ A/D converter with higher sampling rate (3906.25 ksps) and therefore potential mounting issues can be addressed.

4.4 Encoder Autocorrelation Method

The encoder *autocorrelation* method fights the systematic errors of angle respectively angular speed measurement utilizing incremental rotary encoder which are caused by inaccuracies of fabrication of the encoder. The method can be used in applications where change of movement direction is rare or known.

The *autocorrelation* method is elaborated and can be used independently within the *zebra* method. Both these methods can be used independently or combined and the results presented in chapter 5 are obtained utilizing both these methods – data were obtained using the *zebra* method and processed using the encoder *autocorrelation* method.

The errors of a speed measurement using rotary encoder can be divided into two groups: random errors and systematic errors. In figure 32 is depicted typical waveform of signal from rotary encoder and its properties. The delay of rising and falling edge of signal (t_{dr} respectively t_{df}) has three parts: 1) the constant part is caused by properties of the electrical circuitry 2) the hysteresis part which are caused by different rising and falling delays 3) the jitter part is caused by external stresses. The first part does not cause any problems except time delays. The second part contributes to distortion of signal duty cycle depending on the actual period. The difference in the delays can be simply eliminated by measuring the period of the signal from rising edge to the rising edge (t_{rr}) and from falling edge to the falling edge (t_{ff}). The such low speeds where the influence of t_{dr} / t_{df} difference is negligible compared to the period, if the duty cycle is known and guaranteed, the speed can be calculated from width of positive pulse (t_p) and width of negative pulse (t_n). The third contribution to delay times is jitter (t_j) caused by external stresses (electromagnetic noise, ambient light noise, noise in sensor power supply and noise coupled to the signal itself). This type of noise cannot be eliminated, but due to its natural cause it is distributed as Gaussian distribution and unwanted frequencies can be filtered out at the cost of lower bandwidth.

Moreover, unlike other sensors, the rotary encoder is integrator from its nature. Consider two consecutive measurements of speed based on distance of rising edges: the first measurement begins at edge at time t_{b1} and ends at edge at time t_{e1}, respectively the second measurement begins at t_{b2} and ends at t_{e2}. Each time measurement is loaded with error with a standard deviation σ.

Number of revolutions per second w can be calculated as

$$w = \frac{t_e - t_b}{n} \pm \frac{\sigma}{n\sqrt{2}} \quad , \tag{7}$$

where n is number of events[13] per revolution. The average made of two consecutive measurements is

$$\frac{w_1 + w_2}{2} = \frac{1}{2}\left(\frac{t_{e1} - t_{b1}}{n} + \frac{t_{e2} - t_{b2}}{n}\right) \pm \frac{\sigma}{2n} \quad , \tag{8}$$

but considering case where end of one measurement and begin of the next measurement is identical ($t_{e(n-1)} = t_{b(n)}$) the average of two consecutive measurements is

$$\frac{w_1 + w_2}{2} = \frac{t_{e2} - t_{b1}}{2n} \pm \frac{\sigma}{2n\sqrt{2}} \quad , \tag{9}$$

which has lower standard deviation. Therefore it is crucial to ensure that there are no "gaps" (criterion $t_{e(n-1)} = t_{b(n)}$ is met) in the measurement by correct design of the measurement algorithm. Unfortunately, the measurement algorithm used by locomotive computer of Škoda 93E do not meet this criteria. One of possible approaches is to execute the algorithm in a FPGA.

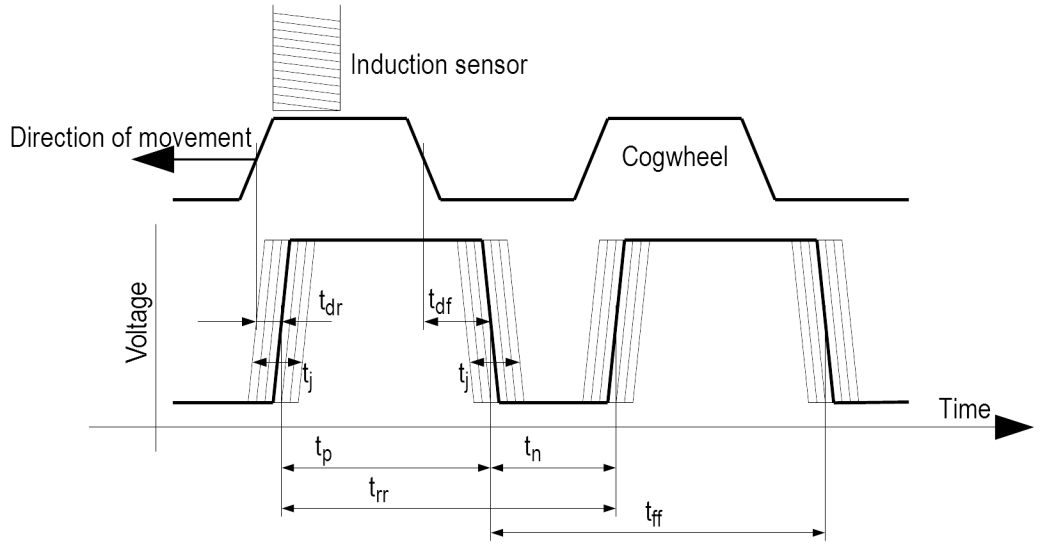

Figure 32: Typical rotary encoder signal and its properties

The actual position of each edge of signal respectively duty cycle is dependent on each position of physical edge on the pattern. This is influenced by accuracy of fabrication, but the

13 In this case it is number of rising edges.

error is repeated each revolution. When assumed no pulse is lost[14] and direction of movement is constant, the errors are repeated every *n* periods, where *n* is number of cogs of the encoder.

The motivation of the *autocorrelation* method is fact that the encoder pattern was glued on locomotive wheel manually and the pattern is made of 13 to 15 pieces printed on A4 paper. The required accuracy of assembly is much higher than accuracy which can be achieved by manual assembly. The error of the assembly shows up in the measurement as systematic error, because the actual inaccuracy can be measured and the speed calculation can counter-count with it.

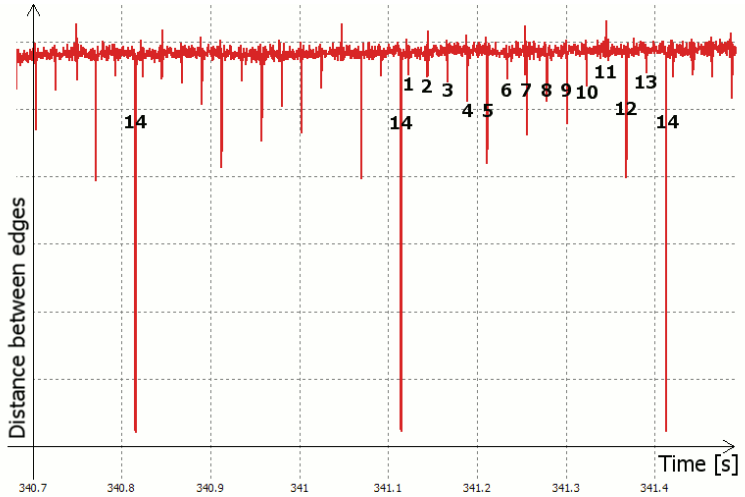

Figure 33: The data acquired by zebra method
The autocorrelation method was not applied

Figure 33 shows waveform of captured speed data using *zebra* method without application of *autocorrelation* method. There are clearly visible boundaries of glued segments of encoder pattern. The last 14th segment is smaller.

Let w_i be the number of calculated revolutions per second between each considered events *i* and *i*+1, relative cog error κ_k can be defined as

$$\kappa_k = \sum_{i=k+n\cdot r} \frac{w_i - p_i}{p_i}; r \in \mathbb{N} \quad , \tag{10}$$

where *r* is number of revolution and p_i is the moving average of w_i

$$p_i = \sum_{j=0}^{n-1} \frac{w_{(i-j)}}{n} \tag{11}$$

14 Many rotary encoders guarantee there are no lost pulses.

of last n samples, that means one revolution. Relative cog error κ_k is intrinsically independent on revolution number r.

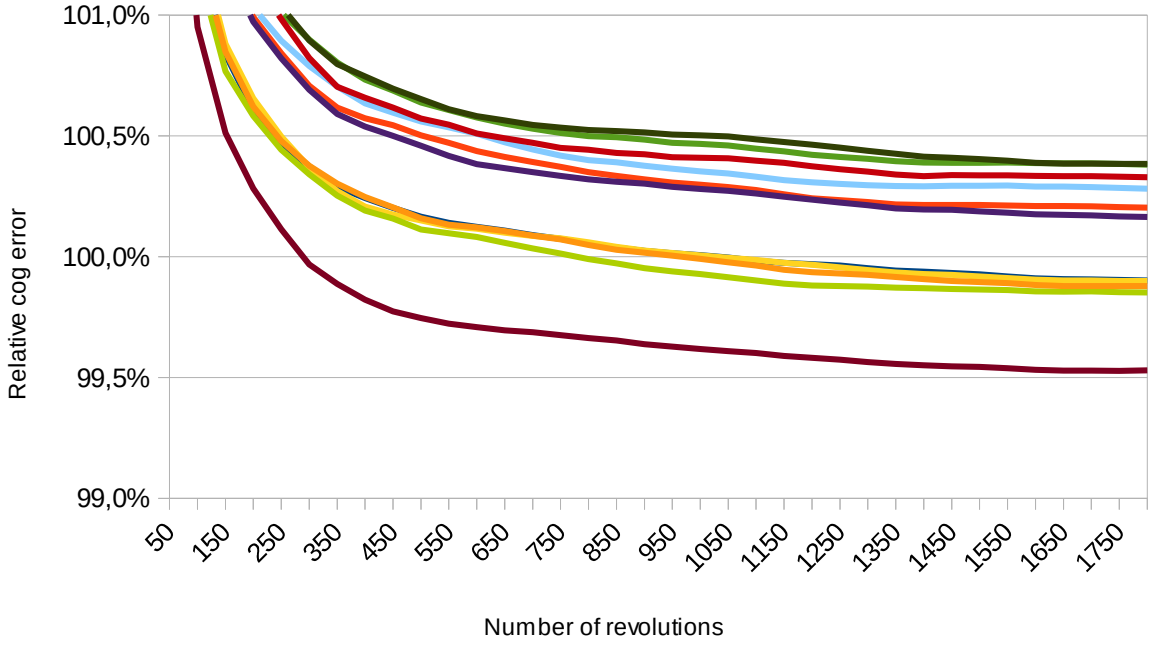

Figure 34: Progress of relative cog error κ_k

After evaluation of cog wheel error κ_i for each revolution and period we would obtain graph similar to one depicted in figure 33. The best option is to obtain the data during uniform travel without any acceleration on straight section of track.

In figure 34 is depicted progress of calculated relative cog error κ_k of few randomly selected cogs. The data were obtained on locomotive Škoda 93E designation number 184503 from encoder mounted on first axle. The figure show first 1800 revolutions of a test run, it means first approximately 7 km.

Relative error of all 100 cogs of a locomotive encoder is depicted in figure 35. The calculation was done during the same test run depicted in figure 34. It can be seen, that the detectable relative cog error caused by cogwheel manufacture is up to ±0,7 % and so ±0,35 km/h at 50 km/h.

Waveform of measured axle speed is depicted in figure 36. The amplitude of noise is lowered as expected by ±0,35 km/h. The rest of the noise attribute to other sources. The group in the beginning and in the middle of the figure are related to entrance of a curve.

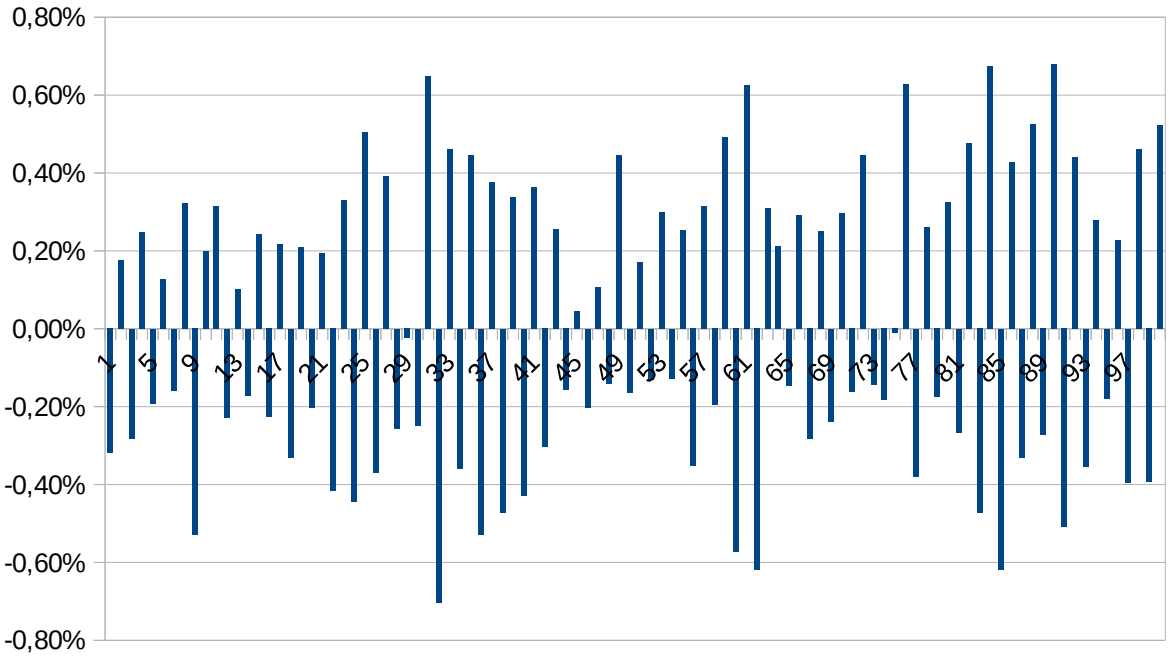

Figure 35: Relative cog error κ_k of all 100 cogs on an axle mounted encoder. Locomotive type Škoda 93E, designation number 184503, first axle.

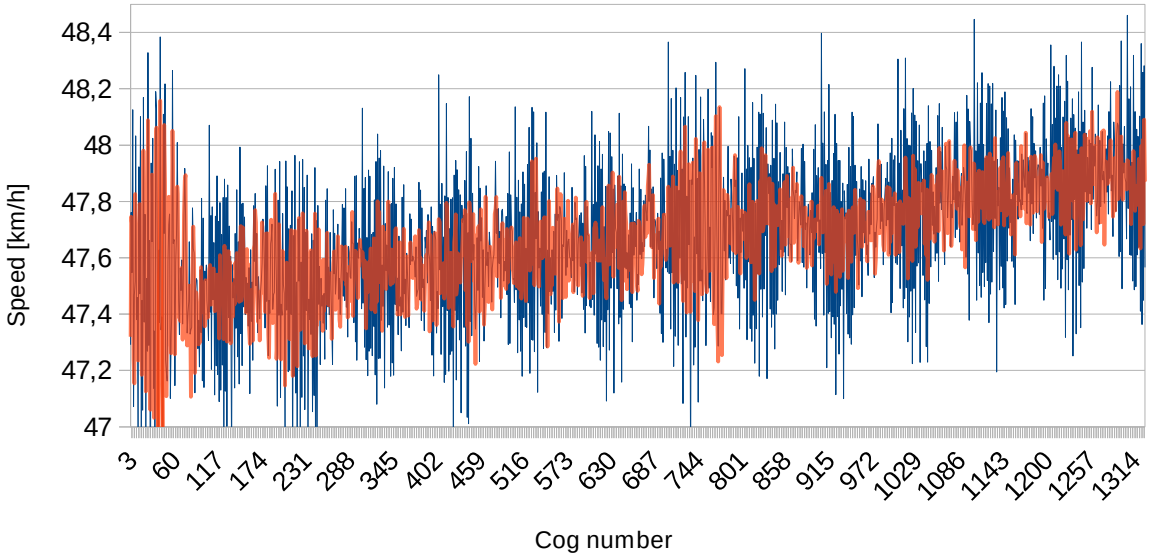

Figure 36: Rotary encoder raw measured and processed wheel speed
Locomotive Škoda 93E, designation 184503, first axle
Blue – raw measured speed
Red – speed processed by autocorrelation method

4.5 Data Acquisition and Record Utilizing FPGA

The data from all sensors is required to be captured for later processing with as most resolution as possible. All the signals are treated as binary, therefore the time resolution (sampling rate) is the most important factor affecting data loss during the process of sampling and recording.

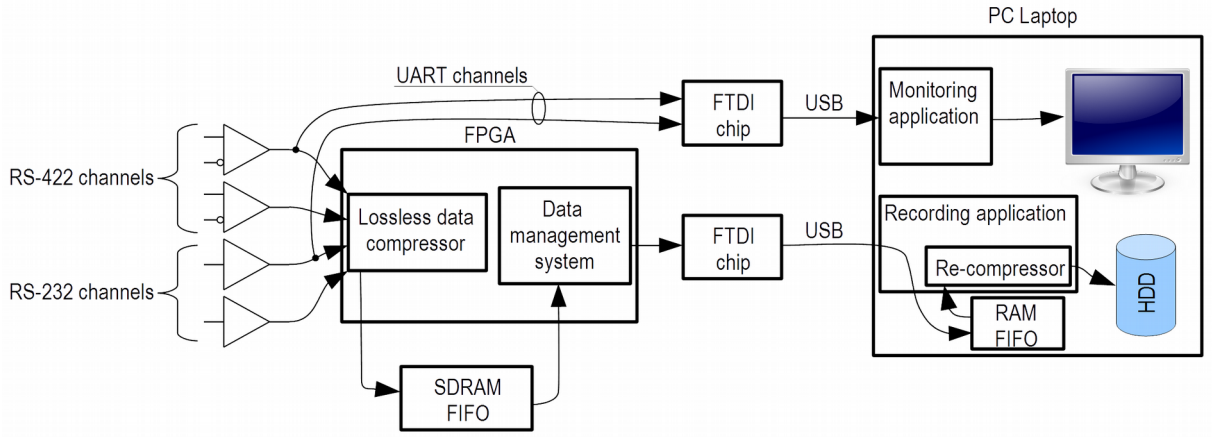

Figure 37: Simplified diagram of data capture chain

The author has designed and developed an electronics[15], which can sample, record and reconstruct all required digital data as 16 digital channels with an accuracy of 5 ns (sampling frequency 200 MHz). Thanks to this it was possible to record all data from all channels simultaneously. The channel types include asynchronous stream of data[16] (UART) at various baud rates[17], raw encoder channels and GPS timing channel. The simultaneous recording of all these channels allowed to acquire precise information of frequency and phase shift between various channels.

To allow recording for long enough with such resolution a lossless compression algorithm was developed and implemented in a Spartan-3 FPGA by Xilinx. The compression is based on run-length encoding (RLE) and variable-length coding applied on both RLE timestamps and input vectors. The net data flow on the input of the compressor is 3.2 Gbps. The only present

15 The components came into existence progressively as different tests were performed. Therefore the electronics are not integrated on one PCB and not operated by a single PC application.

16 Used for analog sensors, transmitted over RS-422.

17 Used baud rates of asynchronous channels include standard 9.6 kbps and 115.2 kbps and special high-speed 312.5 kbps (10 MHz / 32).

means of information loss is the sampling and the fact of presence of an input filter which filters out signals with width less than 10 ns. The delay of the filter is constant and present on every digital input to the same extent. The highest expected frequency on any of the inputs correspond to the maximum UART baud rate 312.5 kbps. All other considered channels including encoder data channels generate signals with frequency much lower than 10 kHz.

The data are compressed in an FPGA and sent to a FIFO buffer constituted mostly by SDRAM memory of size 512 Mbit. The compressed data are transferred over USB 2.0 (480 Mbps) to a Laptop PC, where the data are processed and stored by a 32-bit Windows application. The application partially decompress the data (only the variable-length coding, RLE compression stage is kept) and afterward it compress the data using common DEFLATE algorithm[18]. Because the DEFLATE algorithm process the data stream slower than it is generated by the RLE compressor, the FIFO is vital part of whole data recording chain.

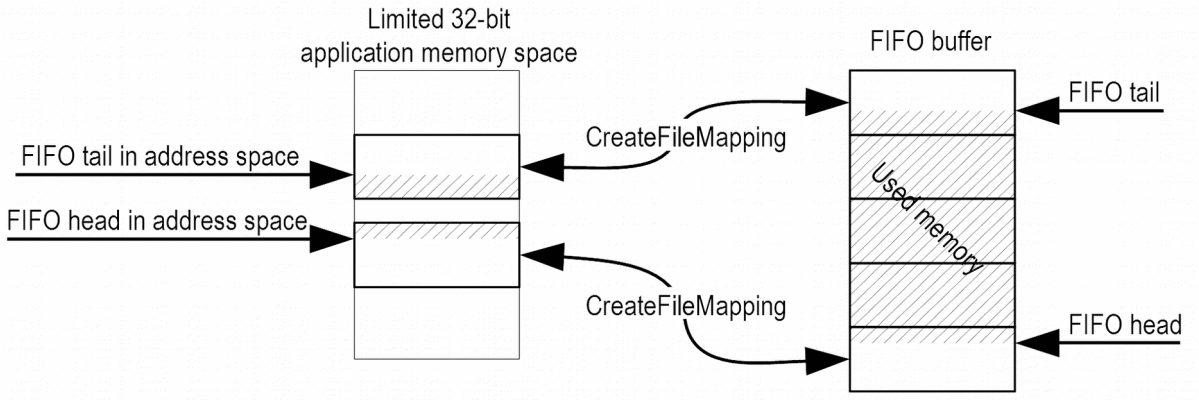

Figure 38: FIFO organization in 32-bit memory address space

Every 32-bit application is limited by its available address space. Therefore it is not possible to fit whole FIFO buffer managed by the application into the application address space. According to the figure 38, only a small portion of the FIFO buffer is mapped into the application's address space utilizing the *CreateFileMapping* WINAPI function. The FIFO is divided into blocks and the application has mapped in at least the first and the last block of the buffer[19]. This method allowed to use FIFO of size almost 75% of all available RAM+swap.

18 The DEFLATE algorithm is widely used in *zip* and *png* file formats. The algorithm owes its extension to the *zlib* library, which is very easy to use.

19 This very much resembles using of XMS on 16-bit MS-DOS.

The monitoring application mentioned in figure 37 is used for diagnostic purposes and to monitor status and data from some of the sensors before the actual test run is initiated. The application also displays downloading status of GPS Ephemeris Data and Almanac Data.

4.6 Test Run Data

Very accurate data about speeds of both wheels of a wheelset among other information were obtained during several test runs with the locomotive Škoda 93E. Out of these data it was possible to extract the frequency and phase shift of vibrations on both wheels of the wheelset. Such data were not previously published.

Both raw recorded data by logic analyzer and processed data are depicted in figure 39.

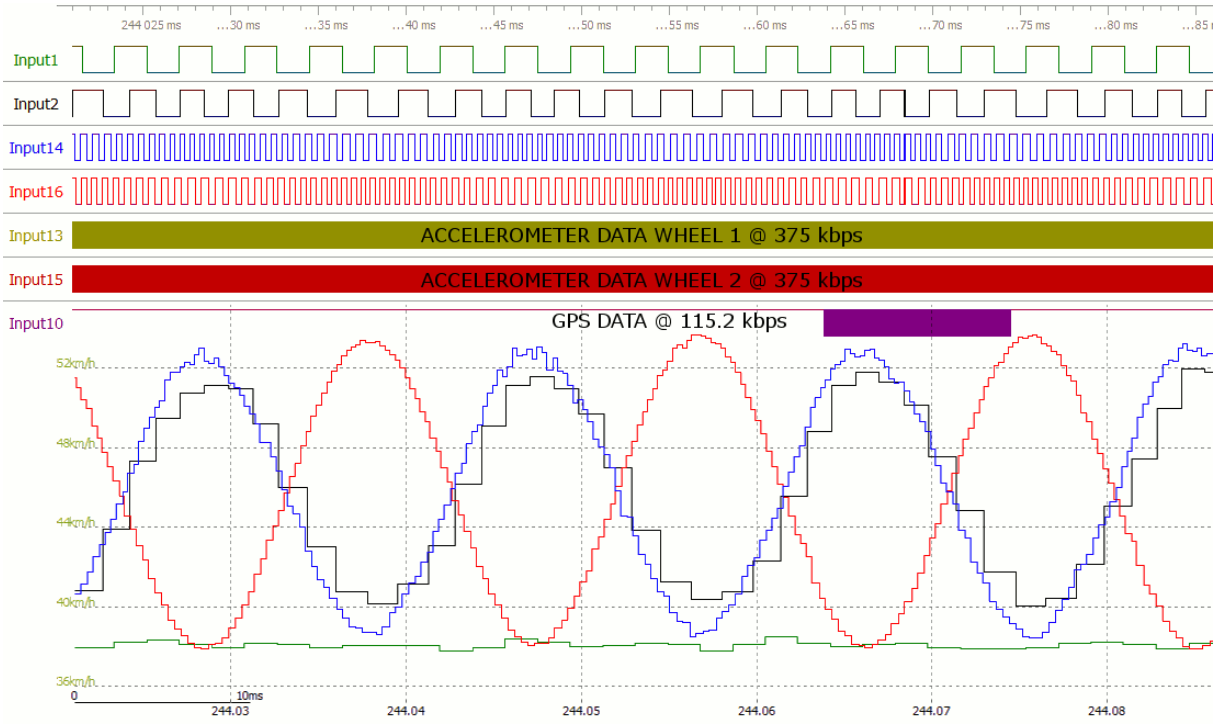

Figure 39: Raw and processed data from logic analyzer

Interpretation of these data is discussed in the chapter 5.

5. Three-Mass Traction System Model

5.1 Zebra Method Obtained Data – Locomotive Škoda 93E

The data obtained by the *zebra* method can be used to identify torsional vibrations of the traction system and better understand the conditions during wheel slip. The data were obtained during test runs on locomotive Škoda 93E.

Vibrations on two different frequencies have been identified using *MATLAB* software. There are documented and expected vibrations on two frequencies corresponding to eigenvalues of the system [22, 33, 34]. Both frequencies were further isolated using two digital filters. The magnitude response of both filters is depicted in figure 40.

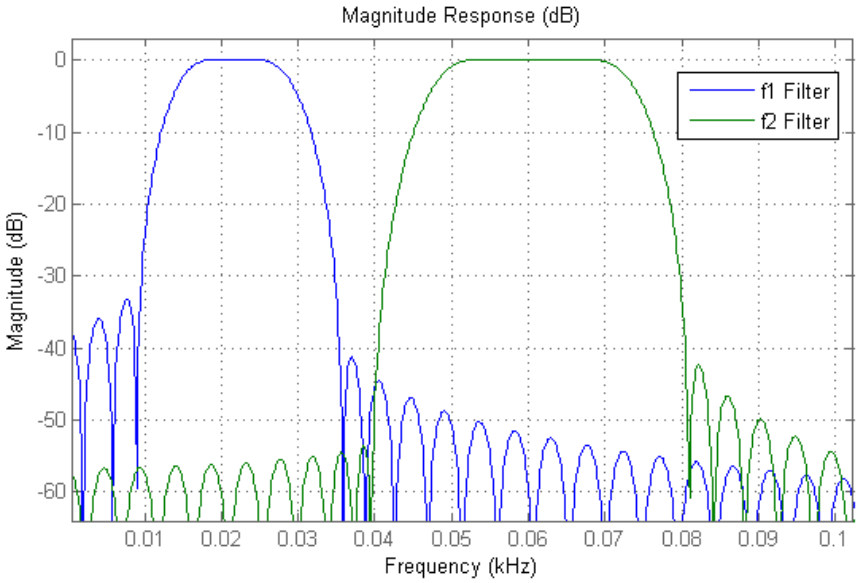

Figure 40: Magnitude response of FIR filter used for frequency isolation

The filters are constructed as FIR filters with emphasis on group delay which has to be constant for all frequencies and same for both filters.

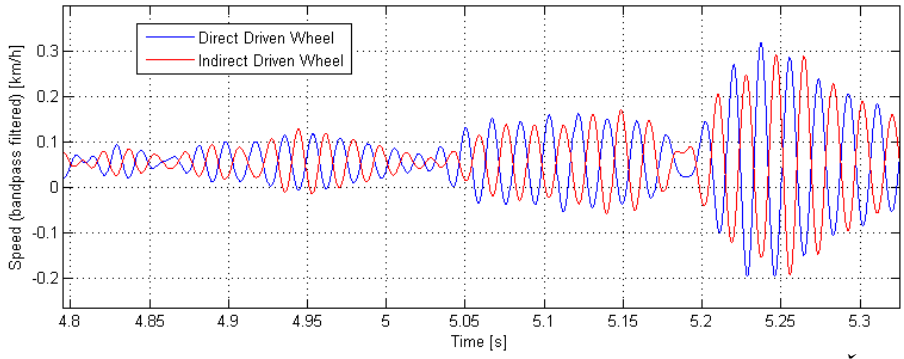

Figure 41: Acquired wheel speed data band-pass filtered 50-70Hz on Škoda 93E

Waveform depicted in figure 41 is cutout of acquired speeds of direct driven wheel (DDW) respectively indirect driven wheel (IDW) filtered by band-pass filter with pass in range 50 - 70 Hz (filter f2 depicted in figure 40)[20].

The figure 41 show there are wheelset axle torsional vibrations on both wheels approximately of the same amplitude (in some phenomena there is higher amplitude on direct driven wheel, in some cases in higher amplitude on indirect driven wheel) and the vibrations are on both wheels in antiphase. The vibrations are imperceptible without tangential traction force. In modes of operation with tangential force and without prominent slippage the vibrations reach amplitude of tenths km/h, during excessive slippage the amplitude can reach enormous magnitude. Largest observed slips at speed 50 km/h show peak-peak amplitudes of 30 km/h during slips with average slipping speed of 15 km/h[21].

Waveforms depicted in figure 42 are captured during slip on dry rail filtered by the filter f1 with band-pass 18 - 25 Hz from figure 40.

20 The signal is not symmetric around horizontal axis due to imperfect attenuation of DC component.

21 The development of such slides can be considered as fault of slip regulator. Such slips are common on the locomotive Škoda 93E because of inclusion of non-linear filter in processing of rotary encoder data. The vibrations behave such way that the minimum of instant slip value is zero (this was confirmed by comparing the axle speed on straight track with longitudinal train velocity obtained by high accuracy GPS receiver) and the maximums are shifted towards higher values. The mentioned non-linear filter drops values of speed which varies too much from previous valid value. The computer ignores most of the values during vibrations and only the values near the minimum were considered to be valid. These values did not differ from reference train speed. Some slips were ignored by the computer for several seconds.

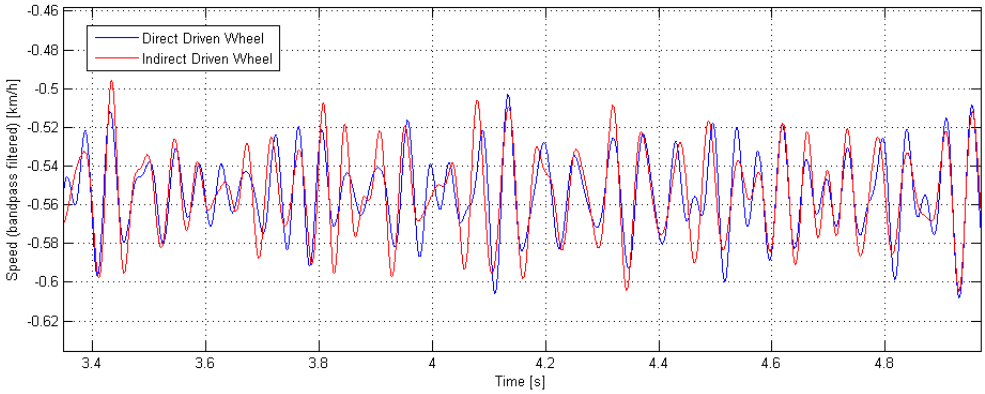

Figure 42: Acquired wheel speed data band-pass filtered 18-25Hz on Škoda 93E

The stability of these vibrations is much lower (higher damping) than those in figure 41 and the amplitude is significantly lower. The presence of the oscillations is uniform during the test run independent on the actual mode of operation and the amplitude is stable during slips. The amplitude is the same on both direct driven and indirect driven wheels and the vibrations are in phase.

This type of oscillations correspond to torsional vibration between traction machine and wheelset – this is published and studied in [34, 22, 16]. The authors also discuss methods of appropriate traction motor control with possibilities of active damping.

The table 7 summaries obtained properties of detected wheelset vibrations.

	f_1	f_2
Frequency	approx. 22 Hz	approx. 52 Hz
Amplitude between wheels	approx. the same	approx. the same
Phase between wheels	approx. the same	approx. the opposite

Table 7: Obtained properties of detected wheelset vibrations

5.2 Zebra Method Obtained Data – Locomotive CNR HXD2

Author has access to data acquired by the *zebra* method during test run of locomotive HXD2 of Chinese locomotive manufacturer CNR Datong (nowadays CRRC Datong). Unfortunately there are not enough freely available information about the bogie construction and means of torque transmission from the traction machine to the wheelset to build up sufficiently accurate mathematical model. The obtained data show similarities with the data acquired on locomotive Škoda 93E. There are similar wheelset axle torsional vibrations at frequency of about 55 Hz between wheels of the wheelset, but the vibrations are not in perfect antiphase in this case. This would suggest the vibrations are also present on the traction machine. The second frequency, which can be identified is approximately 20 Hz on direct driven wheel and approximately 30 Hz on indirect driven wheel. Both these frequencies are in ratio 2:3. The three-mass model discussed in the chapter 5.3 is in this case too simple to explain and simulate this behavior.

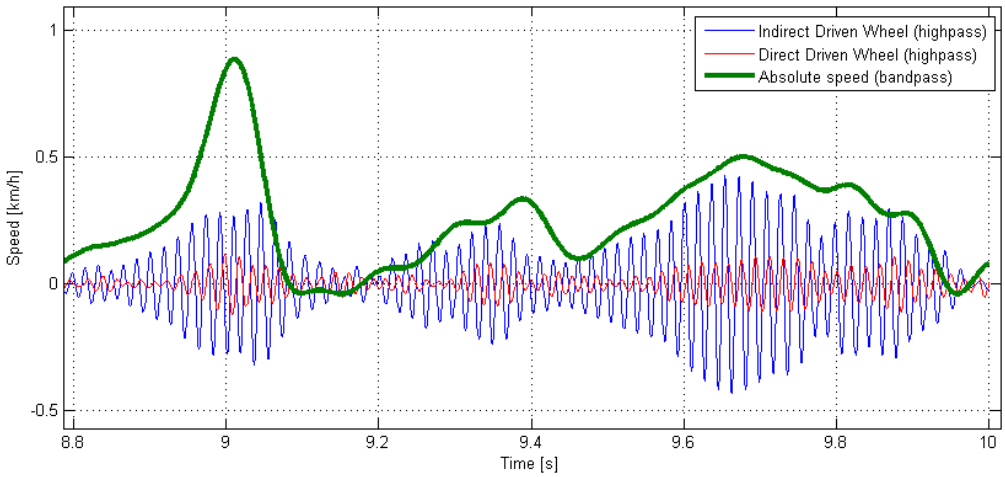

Figure 43: Acquired and filtered wheel speed data on CNR HXD2

The waveform in figure 43 shows data obtained during a test run on a locomotive CNR HXD2 during slips on dry rail. All performed filtration is done with filters with the same group delays. There are visible vibrations at frequency 55 Hz, indirect driven wheel show higher amplitudes. Green waveform in figure 43 represents band-pass filtered speed with eliminated DC and 55 Hz components. On the right-hand side of the figure is slip which has similar properties with the slip observed on the locomotive Škoda 93E – minimums of

oscillations of the indirect driven wheel follows the predicted train longitudinal speed (green waveform acts as envelope for the blue waveform). Because the direct driven wheel of similar moment of inertia shows lower amplitudes and is not perfectly antiphase, it is evident that other mechanical part of the torque transmission system is oscillating at this frequency. This could not be confirmed by direct measurement, because it was not possible to access further high quality data. Author has data from locomotive rotary encoder directly mounted on traction AC induction machine (ACIM), but these data are incorrectly sampled and non-linearly filtered by the locomotive computer and are driven useless for the analysis.

Unfortunately there are not enough freely available information about the bogie construction and means of torque transmission from the traction machine to the wheelset to build up sufficiently accurate mathematical model, but from the data which are available is demonstrable that there are vibrations of wheels of the wheelset which are prominent during slips and may reach considerable amplitudes.

5.3 Three-Mass Model of Torque Transmission System

To explain the obtained data it is necessary to look closer at the construction of bogie and its rotational masses. The behavior can be modeled and studied using three-mass model of the torque transmission system. Out of the work of Danzer, Schwartz, Buscher, Engel and others [22, 33, 34, 35] follows that frequencies of locomotive frame and case are lower than observed frequencies. These movements have indirect effect on the adhesion – they cause change of the normal force. Well designed slip regulator reacts on normal forces (see equation (1)) changes, because they react fast enough to detect the changes in closed loop regulation. The dynamic forces on locomotive frame are well known in the industry and compensated.

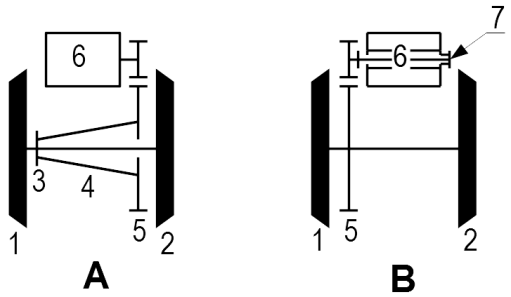

Figure 44: Simplified schematic of torque transmission system
A – hollow shaft; B – Cardan shaft
1 – direct driven wheel
2 – indirect driven wheel
3 – flexible joint
4 – hollow shaft
5 – gearbox
6 – traction machine
7 – Cardan shaft

There are discussed two different configurations of bogie and traction machine mounting depicted in figure 44. Torque transmission with hollow shaft (A) is common on locomotives with ACIM as traction machine, like BR120 discussed in [33, 34, 35], while Cardan shaft was common on Škoda locomotives with DC traction machine (B).

In the case of hollow shaft (A) the gearbox (5) is fully sprung mass. The space for necessary movement is in the cavity of hollow shaft (4). In the case of Cardan shaft (B) is the gearbox only partially sprung mass and the space for necessary movement is in the cavity of hollow rotor of DC machine.

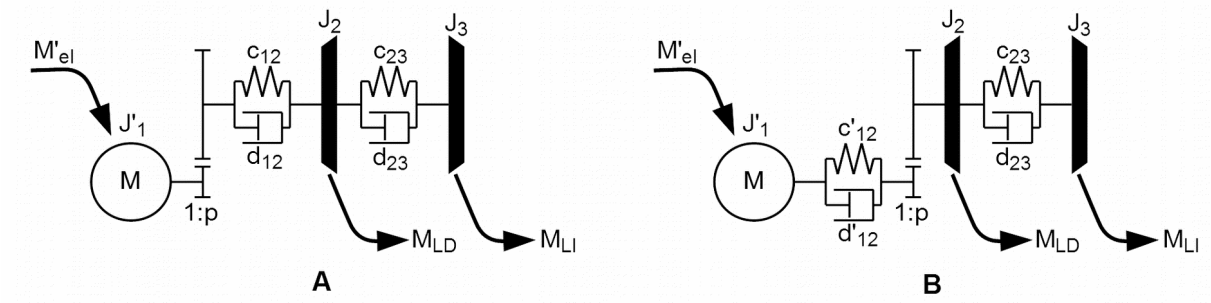

Figure 45:Three mass model of torque transmission system

Both systems depicted in figure 44A, B can be simplified and modeled using a three-mass model according to figure 45.

Both models, from mathematical point of view, differ only whether most of the stiffness c_{12} (and its associated damping d_{12}) is before or behind the gearbox with ratio 1:p. In one case the stiffness and the damping belongs to hollow shaft, in the second case the stiffness and the damping belongs to Cardan shaft. It is useful to recalculate all the quantities to the one side of the gearbox to eliminate the need to work with gearbox ratio coefficient. In this thesis the quantities denoted with prime (′) are the quantities recalculated to the side of traction machine. The quantities without prime are recalculated to the side of wheelset using the formula

$$\begin{aligned} c_x &= c_x' \cdot p^2 \\ d_x &= d_x' \cdot p^2 \\ J_x &= J_x' \cdot p^2 \\ M_x &= M_x' \cdot p \end{aligned} \quad , x \in \{1, 2, 3, 12, 23\}. \tag{12}$$

After recalculation of all components of the model to the side of the wheelset are both discussed variants the same. The general three-mass model is depicted in figure 46.

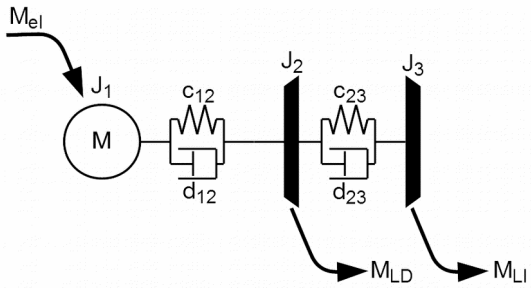

Figure 46: General three-mass model of torque transmission

Assuming all the parameters of the model and linear and time-invariant (LTI), the system can be described using set of ordinary differential equations (ODE)

$$\begin{aligned} \dot{x}_1 &= f_1(x,u,t) \\ \dot{x}_2 &= f_2(x,u,t) \\ &\vdots \\ \dot{x}_n &= f_n(x,u,t) \end{aligned} \quad . \tag{13}$$

Obtaining accurate parameters (J_1, J_2, J_3, c_{12}, c_{23}, d_{12}, d_{23}) of the model is relatively large problem. Manufacturer of the locomotive do not specify these parameters and it is also not trivial task to obtain the parameters. The parameters of locomotive BR120 are listed in [33, 34, 35], but they slightly differ one from another.

The next source for filling of the model is the work of Danzer [22], who deals with anti-slip protection and regulator on Škoda locomotives of so called II. generation (factory designation 69E, 71E (ČSD class 163, 363)) and he also provides the data for III. generation locomotive Škoda 85E (ČSD class 169). The test runs were performed on the locomotive Škoda 93E (class 184) is designated also as III. generation and has bogie of similar construction.

	BR120	**65E (Class 150)**	**85E (Class 169)**	**93E (Class 184)**
1:p	1:4.818	1:3.176	1:5.333	1:4.5
p^2	23.21	10.09	28.44	20.25

Table 8: The gearbox ratio of discussed locomotives

The table 8 holds the values of gearbox ratio p of mentioned types of locomotive. The squared value p^2 is used in the recalculation of moment of inertia, stiffness and damping coefficients. Because the conversion factor p^2 is in the second power, the differences between locomotives of similar designation can be up to triple.

The table 9 shows the published values of the three-mass model. Bold listed values in the table are the values which are published by the respective author, italics listed values are the recalculated values. Each cell holds on first line the value recalculated to the side of wheelset, the second line holds the value recalculated on the side of electric machine. The moment of inertia of traction machine (J_1) is naturally placed on the side its side of the gearbox (in brackets), the moments of inertia of direct and indirect driven wheel, J_2 respectively J_3, are naturally places on the wheelset side of the gearbox, without brackets.

Author	**Danzer [22]**	**Engel [34]**	**Buscher [35] 3 mass model**	**Buscher [35] 6 mass model**	**Schwartz [33]**
Locomotive	65E DC machine Cardan shaft	BR120 ACIM machine Hollow shaft			
(J_1)	*504 kgm²* (**50 kgm²**)	*530 kgm²* (**22.82 kgm²**)	*532 kgm²* (**22.9 kgm²**)	**466.6+55.0+10.1 kgm²** (*20.1+2.37+0.44 kgm²*)	**531.51 kgm²** (*22.9 kgm²*)
J_2	Total J_2+J_3: **345 kgm²** (*34,2 kgm²*)	*175 kgm²* (**7.55 kgm²**)	*170 kgm²* (**7.33 kgm²**)	**163.0+9.7 kgm²** (*7.02+0.42 kgm²*)	**170.13 kgm²** (*7.33 kgm²*)
J_3		*157 kgm²* (**6.77 kgm²**)	*157 kgm²* (**6.78 kgm²**)	**157.3 kgm²** (*6.78 kgm²*)	**157.31 kgm²** (*6.78 kgm²*)
c_{12}	*7061 kNm* (**700 kNm**)	*4248 kNm* (**183 kNm**)	*4100 kNm* (**176.6 kNm**)	~4162 kNm (*~179.3 kNm*)	**4167 kNm** (*180 kNm*)
c_{23}	not mentioned	*7080 kNm* (**305 kNm**)	*7070 kNm* (**304.6 kNm**)	**7060 kNm** (*304 kNm*)	**7070 kNm** (*305 kNm*)
d_{12}	*2421 Nms* (**240 Nms**)	*640 Nms* (**27.57 Nms**)	*1132 Nms* (**48.76 Nms**)	n/a	**1131.9 Nms** (*48.76 Nms*)
d_{23}	not mentioned	53.6 Nms (**2.31 Nms**)	*39.7 Nms* (**1.71 Nms**)	**73.7 Nms** (*3.17 Nms*)	**39.6 Nms** (*1.71 Nms*)

Table 9: Published three-mass model parameters

The data listed in the table 9 show that in the case of the moments of inertia of wheels (J_2 and J_3) different papers match. The same match is also about the moment of inertia of machine (J_1), because [22] state that DC machine has about twice moment of inertia compared to ACIM. More interestingly, the recalculated moment of inertia of DC machine on locomotive 65E is about the same as recalculated moment of inertia of ACIM on locomotive BR120, because the recalculation coefficient on BR120 p^2 is about twice such on 65E. The moment of inertia can be obtained from bogie drawings. Calculating of stiffness and damping directly from bogie drawings does not lead to satisfactory results which can be confirmed by measurements.

5.4 Identification of Three-Mass Model Parameters

The ordinary differential equations (ODE) describing the state-space linear time-invariant system with n internal state variables and r inputs can be expressed using matrix notation as

$$\dot{\boldsymbol{x}} = \boldsymbol{A}\,\boldsymbol{x} + \boldsymbol{B}\,\boldsymbol{u} \quad , \tag{14}$$

where the state vector $\boldsymbol{x}$ is a column vector of length n, the input vector $\boldsymbol{u}$ is a column vector of length r, $\boldsymbol{A}$ is an $n \times n$ square matrix of constant coefficients a_{ij} and $\boldsymbol{B}$ is an $n \times r$ matrix of the coefficients b_{ij} what weight the inputs.

The system depicted in figure 46 can be described by a corresponding system matrix $\boldsymbol{A}$ and respective vector $\boldsymbol{x}$:

$$\boldsymbol{A} = \begin{bmatrix} -\frac{d_{12}}{J_1} & \frac{d_{12}}{J_1} & 0 & -\frac{c_{12}}{J_1} & \frac{c_{12}}{J_1} & 0 \\ \frac{d_{12}}{J_2} & -\frac{d_{12}+d_{23}}{J_2} & \frac{d_{23}}{J_2} & \frac{c_{12}}{J_2} & -\frac{c_{12}+c_{23}}{J_2} & \frac{c_{23}}{J_2} \\ 0 & \frac{d_{23}}{J_3} & -\frac{d_{23}}{J_3} & 0 & \frac{c_{23}}{J_3} & -\frac{c_{23}}{J_3} \\ 1 & 0 & 0 & 0 & 0 & 0 \\ 0 & 1 & 0 & 0 & 0 & 0 \\ 0 & 0 & 1 & 0 & 0 & 0 \end{bmatrix} \quad \boldsymbol{x} = \begin{bmatrix} \omega_1 \\ \omega_2 \\ \omega_3 \\ \varphi_1 \\ \varphi_2 \\ \varphi_3 \end{bmatrix} \tag{15}$$

By solving the eigenvalues and eigenvectors of the matrix $\boldsymbol{A}$ we can obtain the solution of oscillations of the system.

	93E (class 184) expected values	**Comment**
p	4.5	Gearbox ratio 18:81
J_1	810 kgm^2	J'_1 = 40 kgm^2; $J_1 = J'_1 \cdot p^2$ = 810 kgm^2
J_2	190 kgm^2	Incl. gearbox cogwheel 60 kgm^2
J_3	130 kgm^2	$J_2 + J_3$ = 320 kgm^2
d_{12}	0	Damping is neglected
d_{23}	0	Damping is neglected
f_1	22 Hz	First discovered frequency of oscillation
f_2	52 Hz	Second discovered frequency of oscillation
$\varphi_{23(f1)}$	0°	Phase between J_2 and J_3 at f_1
$\varphi_{23(f2)}$	180°	Phase between J_2 and J_3 at f_2

Table 10: Measured and expected properties in relation to three-mass model

After substituting of expected parameters of locomotive Škoda 93E to the matrix $\boldsymbol{A}$ according to the table 10, we obtain using *Mathematica* software relatively simple solution of eigenvalues (except trivial solution) as

$$Eig[A] = \pm \frac{\sqrt{-650\,c_{12} - 1296\,c_{23} \pm \sqrt{422500\,c_{12}^2 - 575991\,c_{12}\,c_{23} + 1679616\,c_{23}^2}}}{9\sqrt{2470}} \quad (16)$$

The solution for eigenvalues equal to frequencies f_1 and f_2 from table 10 we get two solutions,

$$1)\ c_{12} = 1.44 \cdot 10^7,\ c_{23} = 2.52 \cdot 10^6, \quad (17)$$

$$2)\ c_{12} = 5.02 \cdot 10^6,\ c_{23} = 7.20 \cdot 10^6. \quad (18)$$

After checking the eigenvectors of the both possible solutions, the second solution (18) corresponds to the expected $\varphi_{23(f1)}$ and $\varphi_{23(f2)}$.

The table 11 lists the estimated model parameters of locomotive Škoda 93E in comparison to other types of locomotives with published three-mass model.

Source	**Identified by measured behavior**	**Danzer [22]**	**Schwartz [33]**
Locomotive	93E DC machine Cardan shaft	65E DC machine Cardan shaft	BR120 ACIM machine Hollow shaft
(J_1)	810 kgm^2 (**40 kgm^2**)	*504 kgm^2* (**50 kgm^2**)	**531.51 kgm^2** (*22.9 kgm^2*)
J_2	**190 kgm^2** (*9.38 kgm^2*)	Total J_2+J_3: **345 kgm^2** (*34,2 kgm^2*)	**170.13 kgm^2** (*7.33 kgm^2*)
J_3	**130 kgm^2** (6.42 *kgm^2*)		**157.31 kgm^2** (*6.78 kgm^2*)
c_{12}	**5020 kNm** (*248 kNm*)	*7061 kNm* (**700 kNm**)	**4167 kNm** (*180 kNm*)
c_{23}	**7200 kNm** (*356 kNm*)	not mentioned	**7070 kNm** (*305 kNm*)
d_{12}	*2430 Nms* (**120 Nms**)	*2421 Nms* (**240 Nms**)	**1131.9 Nms** (*48.76 Nms*)
d_{23}	**40 Nms** (*1.98 Nms*)	not mentioned	**39.6 Nms** (*1.71 Nms*)

Table 11: Estimated model parameters of discussed locomotives

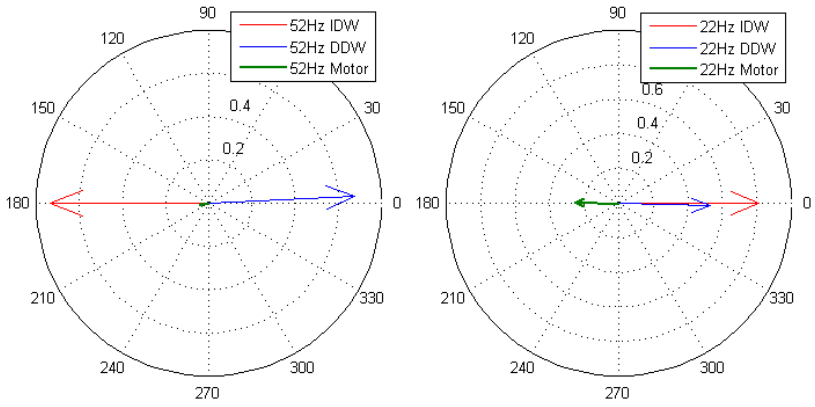

Figure 47: Eigenvectors of three-mass model
IDW – Indirect Driven Wheel J_3, ω_3
DDW – Direct Driven Wheel J_2, ω_2
Motor – J_1, ω_1

In figure 47 are depicted eigenvectors of the system calculated by *MATLAB* software. It is worth of noticing that the eigenvector of traction machine (ω_1) at frequency 52 Hz (torsional vibration of wheelset axle) is diminutive.

5.5 Damping of the Three-Mass Model

The torque transmission system contain several components, which are damping oscillations of the system. The damping can be both lossy as well as loss less. The study of possible damping sources help to understand ways how to suppress and prevent the torsional vibrations.

Parameters of the DC machine

In figure 48 is depicted simplified schematic diagram of electric parameters of traction motors of one bogie for the purpose of analysis. There are two DC motors with separate field coils (sepex). Armature coils are connected in series and through both machines is flowing current i_a. Both field coils are connected in series with current i_b for both machines.

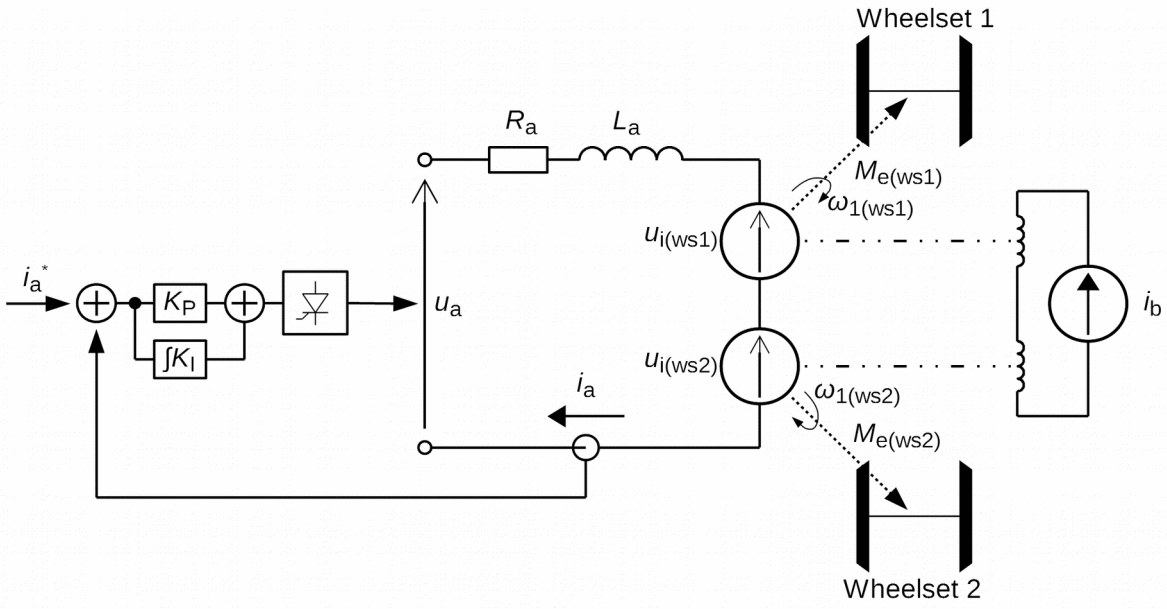

Figure 48: Simplified diagram of electric parameters of one bogie

For the purpose of analysis, the current i_b can be assumed to be sourced from a current source. On the other hand, the current i_a may significantly contribute to the behavior of the whole mechanical system and therefore it is modeled including its PI regulator.

The power output of the machine is $P = \omega \cdot M$, where both angular velocity (ω) and output torque (M) must be recalculated to the same side of gearbox. In the further text, all quantities are expressed on the wheelset side of the gearbox. The torque generated by machine M_e and internal machine voltage u_i can be expressed as

$$\begin{matrix} M_{e(x)} = k_1 \cdot i_a \\ u_{i(x)} = k_1 \cdot \omega_{1(x)} \end{matrix} \quad , x \in \{ws1, ws2\}. \tag{19}$$

The parameter k_1 varies with i_b with dependence close to linear. The resistance of armature circuit is $R_a = 0.1\ \Omega$ and total armature inductance together with filter inductor is $L_a = 21$ mH. The armature voltage can be expressed as

$$u_a = R_a i_a + L_a \frac{di_a}{dt} + \sum_x \omega_{1(x)} k_1 \quad , x \in \{ws1, ws2\}. \tag{20}$$

For the purpose of analysis, k_1 varies so slowly, it can be considered as constant.

Parameters of PI voltage regulator

General PI regulator has transfer function $G(z)$ of

$$G(z) = K_P \left(1 + \frac{1}{T_I} \cdot \frac{T_s}{z-1} \right) \quad , \tag{21}$$

where the parameters of the locomotive regulator are $K_P = 0.9$ V/A, $T_I = 30$ ms, $f_s = 300$ Hz $\rightarrow$ $T_s = 1/f_s = 1/300$ s.

Approximate transfer function of PI regulator in continuous time-space with zero-order hold is $G(s)$:

$$G(s) = K_P \left(\frac{1}{T_I s} \right) \quad , \tag{22}$$

where $K_P = 0.9$ V/A, $T_I = 30$ ms.

Parameters of adhesion characteristics

For the purpose of linear analysis the adhesion characteristics can be linearized in operation point with a linear slope k_μ.

Considering operating point Δv_1 (figure 49) with adhesion coefficient μ_1, near this operating point at $\Delta v_1 \pm \varepsilon$ the adhesion coefficient can be expressed as $\mu_1 \pm k_\mu \varepsilon$.

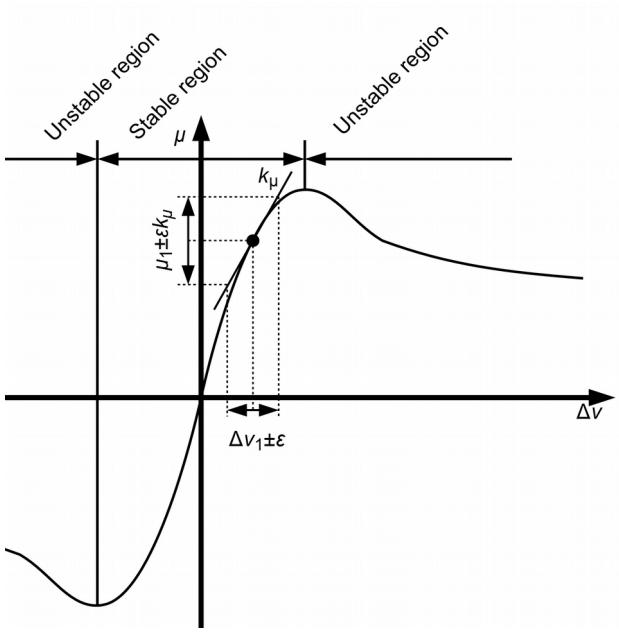

Figure 49: Linearization of adhesion characteristics near operating point

For the purpose of analysis, it is better to use slope of resulting adhesion force, not only the adhesion coefficient and also use the slope related to angular speed (ω, rad/s), not longitudinal velocity (v, m/s). For this purpose can be used equation (1) and using $M = F \cdot r$ we obtain

$$K_\mu = N k_\mu r \quad , \tag{23}$$

where k_μ is

$$k_\mu = \lim_{\epsilon \to 0} \frac{\mu(\Delta\omega + \epsilon) - \mu(\Delta\omega)}{\epsilon} \quad . \tag{24}$$

The normal force N is equal to locomotive weight per wheelset divided by 2 (number of wheels per wheelset) and multiplied by gravity of Earth, or

$$N = \frac{m_{pws}}{2} g \quad , \tag{25}$$

which is m_{pws} = 20 t and N = 98,1 kN.

The resulting matrix $\boldsymbol{A}$ is

$$\boldsymbol{A}=\begin{bmatrix} -\frac{d_{12}}{J_1} & \frac{d_{12}}{J_1} & 0 & -\frac{c_{12}}{J_1} & \frac{c_{12}}{J_1} & 0 & \frac{k_1}{J_1} & 0 \\ \frac{d_{12}}{J_2} & -\frac{d_{12}+d_{23}+K_\mu}{J_2} & \frac{d_{23}}{J_2} & \frac{c_{12}}{J_2} & -\frac{c_{12}+c_{23}}{J_2} & \frac{c_{23}}{J_2} & 0 & 0 \\ 0 & \frac{d_{23}}{J_3} & -\frac{d_{23}+K_\mu}{J_3} & 0 & \frac{c_{23}}{J_3} & -\frac{c_{23}}{J_3} & 0 & 0 \\ 1 & 0 & 0 & 0 & 0 & 0 & 0 & 0 \\ 0 & 1 & 0 & 0 & 0 & 0 & 0 & 0 \\ 0 & 0 & 1 & 0 & 0 & 0 & 0 & 0 \\ -\frac{k_1}{L_1} & 0 & 0 & 0 & 0 & 0 & -\frac{R_1+K_P}{L_1} & 1 \\ 0 & 0 & 0 & 0 & 0 & 0 & -\frac{K_P}{T_I} & 0 \end{bmatrix} \quad \boldsymbol{x}=\begin{bmatrix} \omega_1 \\ \omega_2 \\ \omega_3 \\ \varphi_1 \\ \varphi_2 \\ \varphi_3 \\ i_a \\ u_I \end{bmatrix} \tag{26}$$

where $k_1=\frac{u_i}{\omega_1}$ is the DC machine constant dependent on actual flux coil current i_b, u_i is internal back-EMF voltage and ω_1 is machine angular speed recalculated to the wheels of the locomotive. With the respect to the fact both DC machines of wheelsel 1 and wheelset 2 are connected in series, the total angular speed can be obtained as sum of each wheelset angular speeds $\omega_1 = \omega_{1(ws1)} + \omega_{1(ws2)}$.

The blue and red elements in matrix $\boldsymbol{A}$ are the elements which are not present in pure mechanical three-mass model and represent the electrical part of the model or PI current regulator (red) and damping present on wheel-rail contact (blue).

The general solution of the set of ordinary differential equations (ODE)

$$\dot{\boldsymbol{x}}=\boldsymbol{A}\,\boldsymbol{x} \tag{27}$$

is linear combination of

$$\boldsymbol{x}=c_n \mathrm{e}^{\lambda_n t}\boldsymbol{v_n} \quad , \tag{28}$$

where λ_n are eigenvalues and $\boldsymbol{v_n}$ are corresponding eigenvectors.

The influence of different operating conditions represented by changing the of values k_1 and K_μ on the resulting values of eigenvalues and eigenvectors are presented in table 12 and figure 50.

k_1	K_μ	λ	f [Hz]	v_1 (Motor)	v_2 (DDW)	v_3 (IDW)
0	-13125	27.5 ± 130.40i	20.75	-0,286-0,174i	0,657-0,108i	1
50	-13125	27.3 ± 130.46i	20.76	-0,287-0,176i	0,656-0,109i	1
0	0	-3.92 ± 138.28i	22.01	-0,314+0,005i	0,655-0,0193i	1
60	0	-3.97 ± 138.42i	22.03	-0,316+0,004i	0,654-0,0196i	1
0	13125	-35.1 ± 127.99i	20.37	-0,271+0,181i	0,662+0,0712i	1
50	13125	-35.0 ± 128.15i	20.40	-0,273+0,183i	0,662+0,0716i	1
k_1	K_μ	λ	f [Hz]	v_1 (motor)	v_2 (DDW)	v_3 (IDW)
0	-13125	36.8 ± 323.50i	51.49	0,051+0,033i	-0,932-0,157i	1
50	-13125	36.8 ± 323.50i	51.49	0,051+0,033i	-0,932-0,157i	1
0	0	-4.23 ± 326.64i	51.99	0,057+0,011i	-0,926-0,046i	1
60	0	-4.23 ± 326.64i	51.99	0,057+0,011i	-0,926-0,046i	1
0	13125	-45.4 ± 323.43i	51.48	0,056-0,011i	-0,935+0,063i	1
50	13125	-45.4 ± 323.43i	51.48	0,056-0,011i	-0,935+0,063i	1

Table 12: Eigenvalue and eigenvector dependency on k_1 and K_μ

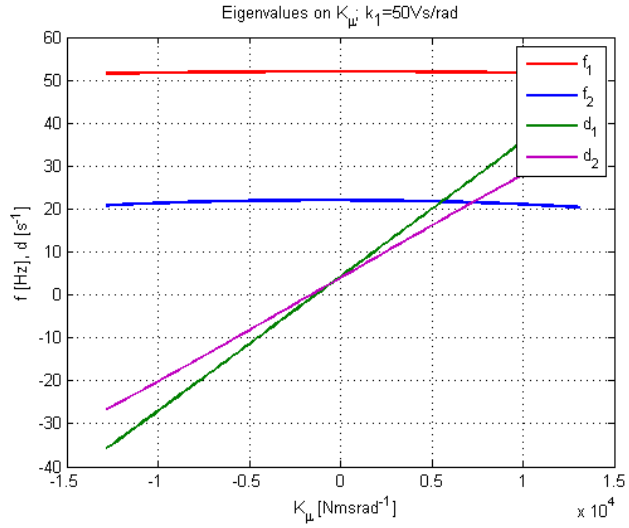

Figure 50: Eigenvalues and eigenvectors dependency on Kμ

In figure 50 is depicted dependence of eigenvalues on value of K_μ. The real part with inverted sign of complex eigenvalue λ representing damping is drawn as d_1 and d_2 (envelope is e^{-dt}). Negative damping means rising amplitude oscillations. The imaginary part of complex eigenvalue λ is drawn divided by 2π as f_1 and f_2 to represent frequency of the oscillations ($e^{i2\pi ft}$) in Hz.

The foregoing means that the DC machine and PI current regulator has negligible influence on the damping of the system (in the meaningful range of k_1 – but the opposite is valid for one order higher values of k_1).

On the other hand the slope of adhesion characteristics K_μ has significant influence on damping of the system. The analyzed slope of $K_\mu = \pm 13125$ Nms/rad correspond to change of adhesion by 56% from its maximum $\mu = 0.38$ (see chapter 3.7) multiplied by normal force $N = 98{,}1$ kN (see equation (25) and (1)) in change of wheel speed by 1 rad/s. In creepage part of the adhesion characteristics can be expected slopes as much as $K_\mu = 50000$ Nms/rad.

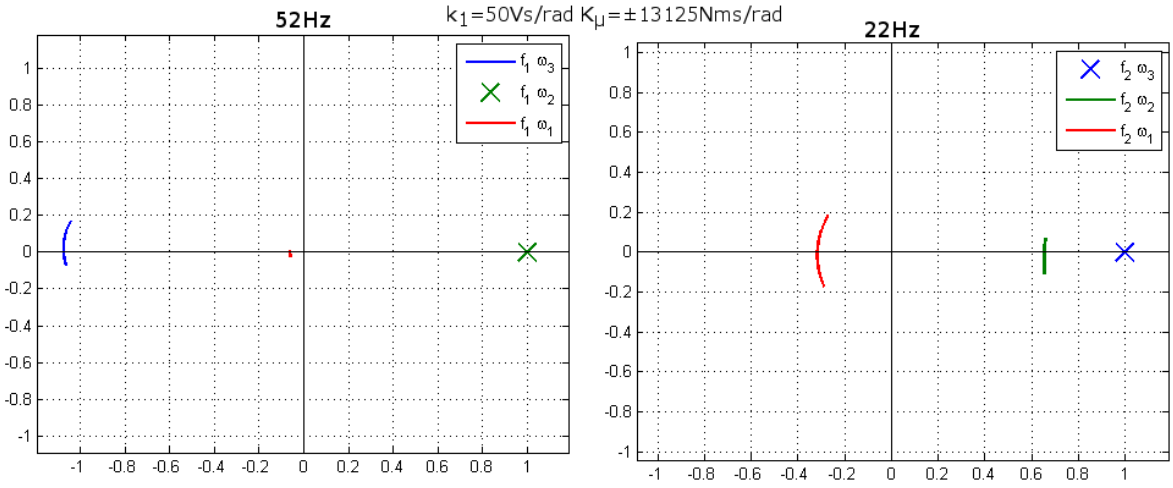

Figure 51: Eigenvector dependency on Kμ

For oscillations with small amplitude ($lim\ \varepsilon \rightarrow 0$, see equation (24)) in figure 51 depicted dependence of eigenvectors on value of K_μ. The situation correspond to the table 12. In the first case (frequency about 52 Hz) depicted on the left half of the figure is for better clarity eigenvector corresponding to ω_2 (representing direct driven wheel) fixed to 1+0i. In the second case (frequency about 22 Hz) depicted on the right half of the figure is for better clarity eigenvector corresponding to ω_3 (representing indirect driven wheel) fixed to 1+0i.

The slope of adhesion characteristics manifest itself as damping of the system with far the most significant importance. Depending on the slope of the adhesion characteristics, the damping can have negative value meaning capability to increase amplitude of the oscillation. Analyzed scale of coefficient $K_\mu = \pm 13125$ Nms/rad is rather conservative.

The mentioned analysis is valid only for linear time-invariant systems. The introduction of variable adhesion coefficient violates this assumption and the analysis is valid only in very small amplitudes of adhesion coefficient ($lim\ \varepsilon \rightarrow 0$). Yet the conclusions can be extended to other situations and even measurements confirm that the effective method of damping of axle

torsional vibration is transition of operating point (or better operating characteristics) into the area of adhesion characteristics that has significant damping effect.

From the figure 51 can be read out that the axle torsional vibration (f_1) is virtually not transmitted to the traction machine. Taking into account that gearbox has not linear stiffness, especially around zero torque, is impossible to damp the vibration using active intervention of traction machine and its regulator. It is important to note, that this does not apply for machine-wheelset vibration (f_2), where it is possible to damp the vibrations using regulator [34, 16].

5.6 Energy Balance and Conditions During Slippage

In figure 52 are depicted typical waveforms of voltage and current of the traction DC machine of one bogie during large scale slip. The values in the figure were obtained by utilizing RS-232 communication link with the bogie traction computer of the locomotive Škoda 93E. The computer is based on Intel 80186 microprocessor. There are three such computers installed on the locomotive, one for each bogie.

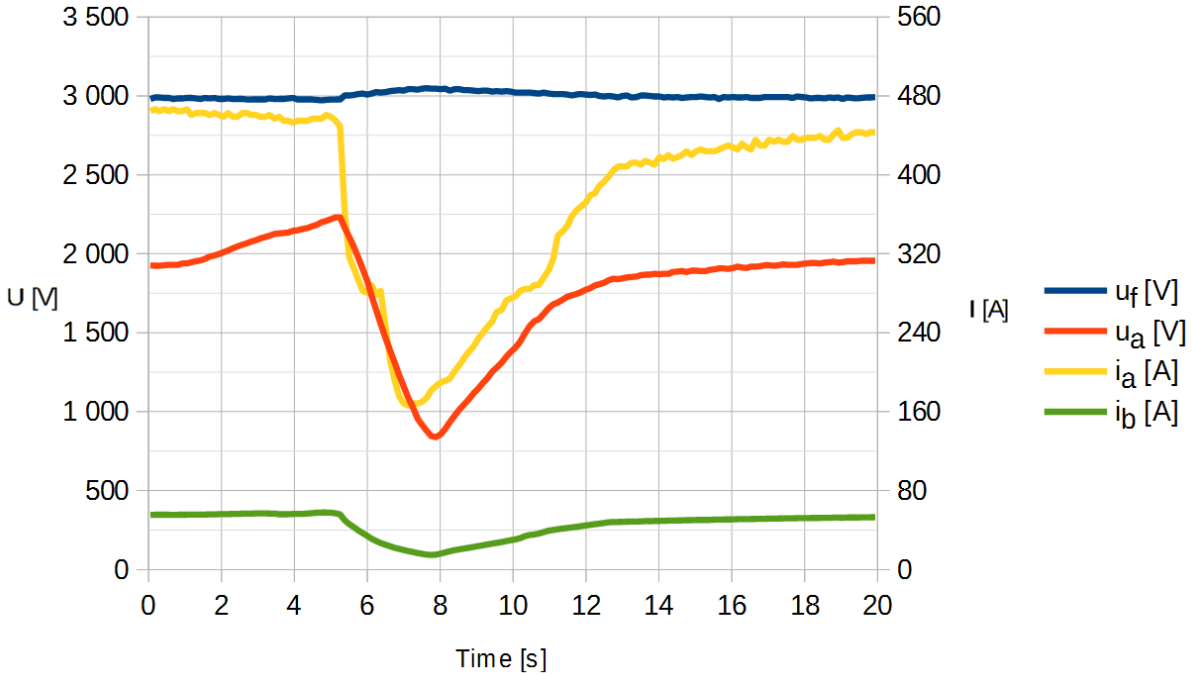

Figure 52: Voltage and currents of DC machine during slip

There are four parameters drawn in the graph. The filtered overhead power line voltage (u_f) has nominal voltage 3000 V and may reflect power taken by the locomotive from the

overhead line. The armature voltage (u_a) of both DC motors in series is proportional to sum of their rpm multiplied by magnetic flux which has almost linear dependence on flux coil current (i_b). The torque of both DC motors is dependent on armature current (i_a) multiplied by aforementioned magnetic flux. By knowledge of internal parameters of the machine can be calculated other quantities representing state of the drive: output torque and rotation speed (the sum of both DC machines). Rotation speed of one DC machine was also captured during the test run, therefore the rotation speed of the second DC machine can be calculated to the end.

During the test run, at the time from the beginning to 5.5 seconds, there is developing a slip on first wheelset. The slip regulator acts twice at times 5.5 s and 6.5 s. The re-adhesion occurs in the time between 6.5 s and 8 s. The the time between 8 s and 13 s the slip regulator output restores to 90% of the initial torque.

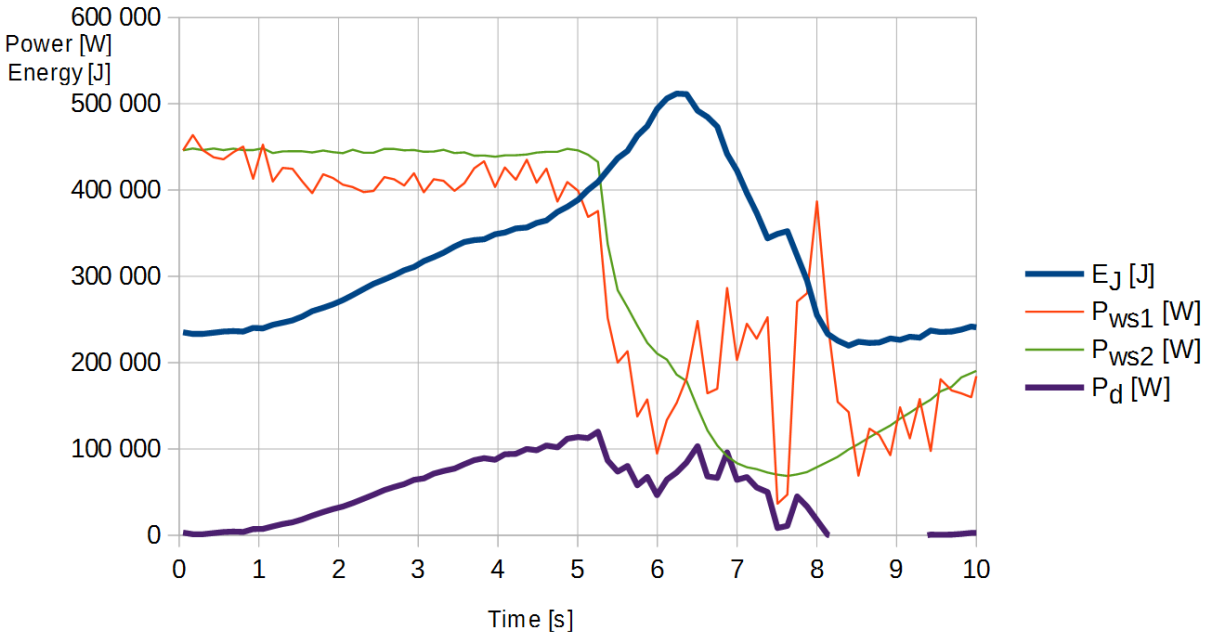

Figure 53: Power and energies during slip

The figure 53 holds calculated values of total kinetic energy stored in rotational parts of the system (E_J), power being transferred by wheelset 1 (P_{ws1})[22] and wheelset (P_{ws2}) and power lost in damping (P_d).

22 This power is the traction force multiplied by velocity.

There can be observed difference between power being transferred by wheelset 1 and wheelset 2, despite both DC machines produce the same torque. The difference is partly stored into surplus kinetic energy of the wheelset 1 and partly lost in damping. Because the rotational speed of DC machine driving the wheelset 1 is rising with unchanged torque, also the power output of the DC machine is rising.

The wheelset 2 output power P_{ws2} can be estimated as

$$P_{ws2} = F_{ws2} \cdot v_t \quad , \tag{29}$$

where F_{ws2} is tangential traction force generated by the second wheelset and v_t is velocity of the train. The train velocity is velocity of wheelset 2 reduced by wheel slip velocity ($v_t = v_2 - v_{s2}$). The energy lost in wheel-rail contact can be neglected by placing wheel slip velocity to zero ($v_{s2} = 0$). The actual magnitude of wheel slip velocity is analyzed in chapter 4.2.

The output torque of each machine can be estimated from currents i_a and i_b.

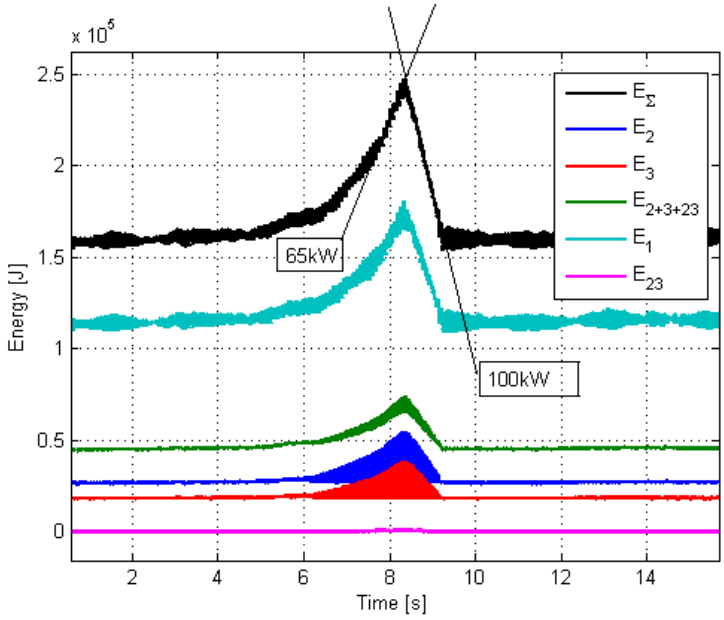

Figure 54: Energy stored in rotational mass during slip
The data were acquired during different test run than data presented in figures 52, 53. The energies are calculated directly from speeds of wheels measured by zebra method.

Total kinetic energy stored in rotational parts can be calculated as $E_J = E_1 + E_2 + E_3 + E_{12} + E_{23}$ (see figure 54) according to labeling of three-mass model (figure 46).

The energy E_{12} is neglected. Energy E_1 is estimated from average value of angular speed as

$$E_1 = \frac{1}{2} J_1 \omega_{avg}^2 \quad , \tag{30}$$

energy $E_2 + E_3 + E_{23}$ is estimated as

$$E_2 + E_3 + E_{23} = \frac{1}{2} J_2 \omega_{min}^2 + \frac{1}{2} J_3 \omega_{max}^2 \approx \frac{1}{2} J_{2/3} \left(\omega_{avg}^2 + \omega_{ampl}^2 \right) \quad , \tag{31}$$

assuming both masses oscillating at phase difference 180° with same amplitude and $J_2 = J_3$. This assumption is very close to the observation (see figure 47).

The power P_J required to accelerate (and decelerate) rotational masses can be calculated as change of energy E_J over time

$$P_J = \frac{\mathrm{d}\, E_J}{\mathrm{d}\, t} \quad . \tag{32}$$

The energy lost in damping on the wheel-rail contact of the first bogie is

$$P_d = F_{ws1} \cdot v_{s1} \quad , \tag{33}$$

where slip speed of first wheelset can be calculated as

$$v_{s1} = v_1 - v_t \tag{34}$$

and tangential tractive force of first wheelset F_{ws1} can be calculated from

$$F_{ws1} = \frac{M_{ws1}}{r} = \frac{P_{el} - P_J}{r \cdot \omega_{avg}} \quad . \tag{35}$$

The decomposition of power into mentioned parts is depicted in figure 55.

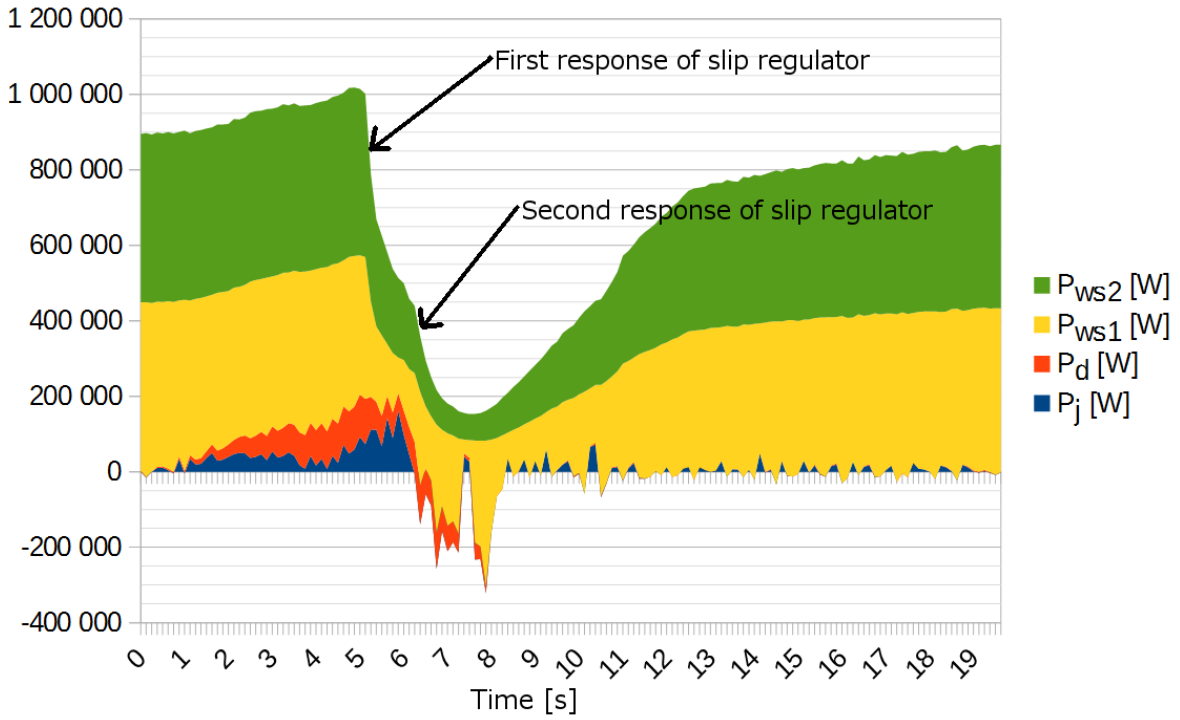

Figure 55: Decomposition of traction power into parts
P_d – Power lost in damping
P_J – Power stored (and recovered) as kinetic energy
P_{ws1} – Power delivered by wheelset 1
P_{ws2} – Power delivered by wheelset 2

The total (stacked) power from zero axis is total power generated by DC machine (P_{el}) is rising while the slip is developing (time to 5.5 second) before slip regulator acts. The area below horizontal axis signify negative value of P_J during re-adhesion.

In figure 56 is depicted calculated actual adhesion coefficient μ during the analyzed slip in dependency on peak-peak amplitude of the wheel speed ($v_{1p\text{-}p}$). The adhesion coefficient is typically drawn as dependent of wheel slip speed (Δv_1). If we neglect[23] the oscillation, it holds

$$\Delta v_1 \approx \frac{v_{1\,p-p}}{2} \quad , \tag{36}$$

because lower amplitude peak follows train longitudinal speed.

23 For example unintentionally by lowering the wheel speed measurement bandwidth.

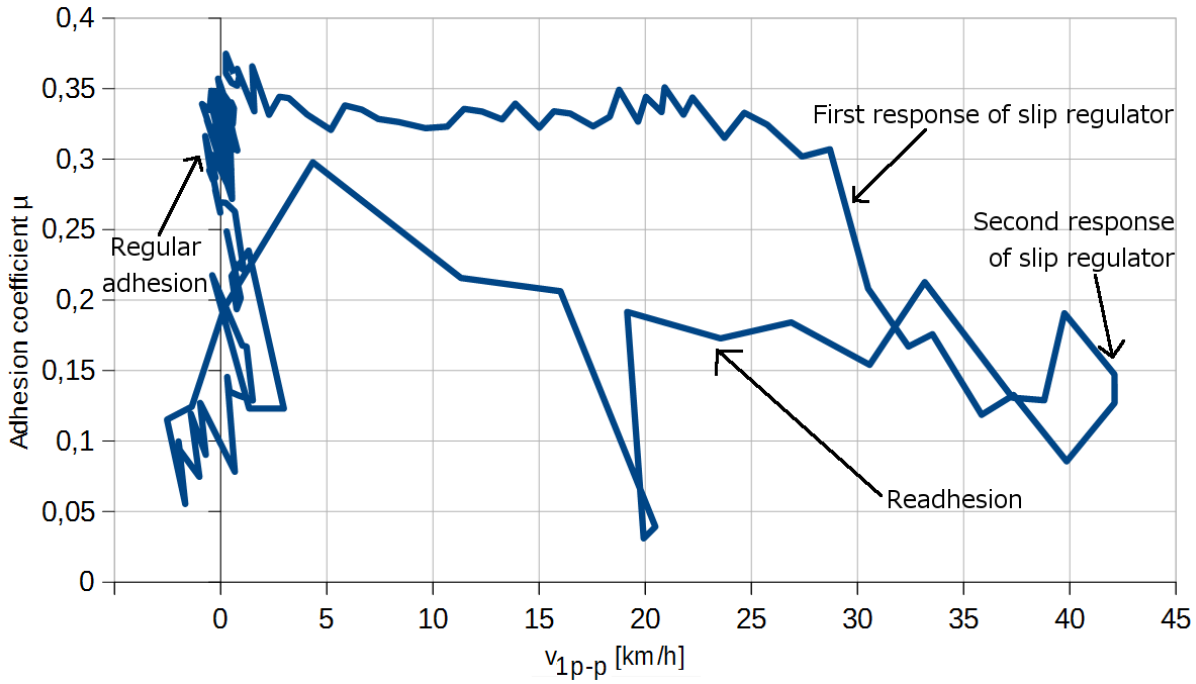

Figure 56: Detected adhesion coefficient μ on wheel speed peak-peak amplitude

The graph in case of substitution of Δv_1 with $v_{1p\text{-}p}$ in the figure 56 resembles other published data [31]. The vibrations during excessive slips makes distinctive noise. The measurements using the *zebra* method were carried out only on two types of locomotive and in both cases there were observed discussed oscillations with various probability. Other authors did not mention oscillations in their studies. This does not exclude neither confirms other authors have neglected oscillations intentionally or unintentionally. Nevertheless both the three-mass mathematical model and measurements on two different types of locomotive with different bogie construction indicate the presence of wheelset axle torsional vibrations and their substantial relation to wheel slip.

5.7 Detection of Wheelset Axle Torsional Vibrations

In figure 57 is depicted example possible filter magnitude response for different axle rotation speeds (very close to actual locomotive speed). The filter is constructed as 4th order band-pass IIR filter operating at time equidistant 1 kHz sampling rate. The measurement can be carried on current rotary encoder installed on the locomotive. Basic rising-to-rising edge measurement produce samples equidistantly in angle, but not time, therefore the signal needs to be interpolated. Independent filling-to-falling period measurement can be also carried out. In the case both measurement data are processed independently, there is no benefit on rising of the Nyquist frequency. Only after both measurements are combined by means of interpolation, the Nyquist frequency is raised, in (rather) theoretical assumption of duty cycle 50 % it is raised by two. The simulated Nyquist frequency is for 10 km/h (blue line in figure 57) approximately 72 Hz.

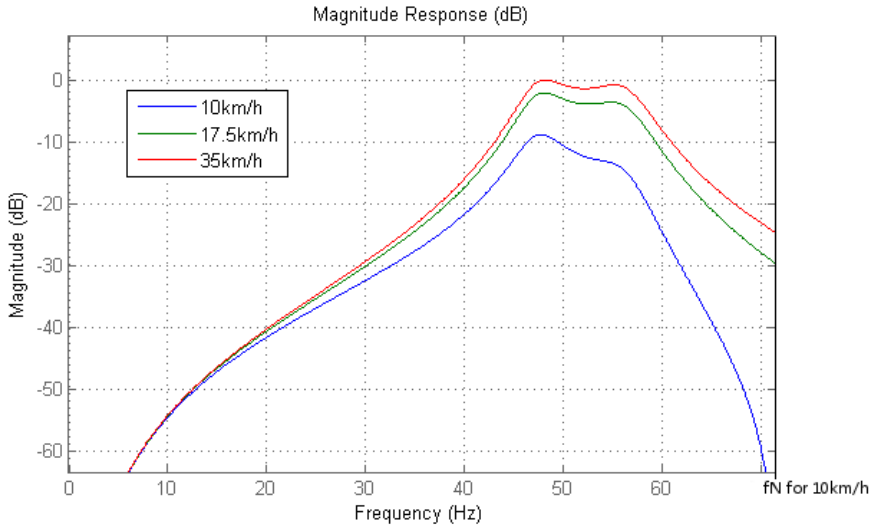

Figure 57: Simulated magnitude response for different speeds

Speed [km/h]	Period [ms]	Nyquist frequency [Hz]	Enhanced Nyquist frequency [Hz] (assuming 50% duty cycle)
0 km/h	∞	0 Hz	0 Hz
5 km/h	28,3 ms	17,7 Hz	35,4 Hz
8 km/h	17,7 ms	28,3 Hz	56,6 Hz
10 km/h	14,1 ms	35,4 Hz	70,7 Hz
20 km/h	7,07 ms	70,7 Hz	141 Hz
30 km/h	4,71 ms	106 Hz	212 Hz
40 km/h	3,53 ms	141 Hz	283 Hz
50 km/h	2,83 ms	177 Hz	354 Hz

Table 13: Nyquist frequency on locomotive speed

In table 13 are listed Nyquist frequencies for different locomotive speeds and two measurement methods – simple rising-to-rising edge and enhanced interpolated measurement based on rising-to-rising edge and falling-to-falling edge. It is important to notice that the Nyquist frequency is for 10 km/h is exactly on the right edge of the figure 57 and therefore for higher frequencies there may be noticeable mirroring of the signal. Another consequence of lack of enough buffer between the Nyquist frequency and band-pass frequency is yet noticeable attenuation of about -10 dB. Therefore there may be included compensation factor for low speeds at the cost of even higher mirroring of unwanted signal. It is theoretically possible in particular cases of lower speeds than 10 km/h to filter and detect the axle torsional vibration signal even when the Nyquist sampling theorem is not met, but this is rather theoretical option because of the attenuation of the encoder (its integration character) itself and the difficulty of mixing unwanted and wanted signals together. Good enough results, if ever, would be achievable only with unacceptable response times.

6. Conclusions

This doctoral thesis has focused on several goals which were fulfilled as follows:

1. Analyze slip velocity and adhesion characteristics
    - The slip velocity was precisely measured by comparison of GPS speed with wheelset axle rotation speed. The results are presented in chapter 4.2 and summarized in table 6.

      Considering straight track with ideal conditions, there are creep ratios as expected by the Kalker's creep theory, but when experiencing conditions other than ideal rail conditions (not straight track, dirt, dust, wet) the effect of other sources of slip speed greatly exceed the Kalker's creep speed. Therefore the typical approach of slip regulator by regulating onto desired slip velocity do not work optimally and it is convenient to enhance the slip regulator by taking onto account different possible sources for detection of wheel slip.
2. Analyze the speed measurement method and propose improvements
    - The axle speed measurement on locomotive Škoda 93E is heavily flawed. The rotary encoder installed on each axle works correctly and reliably and this was verified by unique independent measurement method, but there are major shortcomings in the current processing of the signals from rotary encoders:
        - The measurement is not conducted so that integral character of the measurement is fully utilized (see chapter chapter 4.4).
        - It would be beneficial to install the *autocorrelation* method described in chapter 4.4. The method can improve the accuracy of the measurement and this would be beneficial in low speeds. Moreover, the slip regulator accuracy is most important in situations like setting into motion.
        - It is necessary to remove non-linear filters processing the numerical data and by contrast it is necessary to do all numerical filtering using linear IIR filters[24].

24 The FIR filters would be too computationally demanding.

It is convenient to introduce non-linear filtration to act on the digital signals to eliminate potential short spikes[25].

- The operator of the locomotive suggested to install new rotary encoder with twice resolution (number of signal periods per revolution). This can actually improve the response time and resolution in very low speeds, during setting into motion and move below the lowest speed where can be detected (and filtered) torsional vibrations of wheelset axle (see chapter 5.5), but in higher speeds there is little effect of such upgrade.

All of the mentioned improvements (except rotary encoder upgrade) is possible to be conducted by revising of the bogie computer by installing a new improved electronics card with auxiliary unit for signal conditioning and processing using FPGA technology. Regrettably the economic priorities of the owner and operator of the locomotive Škoda 93E did not make the upgrade possible.

3. Analyze the traction force transmission from traction machine to the wheel-rail contact
   - The three mass mathematical model of traction force transmission from traction machine to the wheel-rail contact was constructed, verified and analyzed (chapters 5.3, 5.4 and 5.5). The parameters of the studied locomotive traction force mathematical model has similar properties as the previously published models of different locomotive type with different bogie construction and therefore the conclusions are not restricted to just the one type of studied locomotive. The mathematical model helped to understand the wheelset axle torsional vibration relation to the adhesion.
4. Analyze the conditions during slippage
   - The traction motor working conditions, slip speed, energy and power balance is discussed in chapter 5.6. Part of the surplus energy is absorbed as kinetic energy of rotational parts. During enormous slippage over 100 kW per wheel is lost in wheel-rail contact as friction. Substantially smaller amount of energy is stored as torsional potential energy in wheelset axle. Virtually any recorded slip was

25 Even though any such spikes were detected during test runs.

accompanied by large scale torsional wheelset axle vibrations. The vibrations were detected in connection to the slips also on the types of locomotives (chapter 5.2).

5. Analyze slip regulator and propose possible improvements
    - The slip regulator on the locomotive Škoda 93E is not working optimally. This is largely due to flawed axle speed measurement and the slip regulator works with incorrect data. The axle speed data are acquired by insufficiently powerful hardware and the data are improperly acquired (chapter 4.1) and inappropriately filtered (chapter 4.4). The construction of the locomotive itself and installation of the rotary encoder is correct and this was verified (chapter 4.3).

      It is possible to upgrade the current locomotive computer (one digital board card) with new FPGA technology without the need for modifications of the locomotive construction. This would enable the computer to better filter out the unwanted wheelset axle torsional vibrations and at the same time to detect the amplitude of the same torsional vibrations, which can be used as one of the inputs for slip regulator.

The conclusions of this doctoral thesis exceed application on single studied type of locomotive. The similarities of three-mass mathematical model of traction torque transmission system with other published types of locomotives means that torsional vibrations are real problem during wheelset axle speed measurements. It is essential during any signal acquisition to study and verify the Nyquist sampling criterion and the same apply for the case of the wheelset axle speed measurements, where vibrations at considerable amplitudes are expected. At the same time, both contemporary and future slip regulator implementations should take into account wheelset axle torsional vibrations as one of the indications of wheel slip.

7. List of Used Literature

[1] Soudris, D.; Masselos, K.; Blionas, S.; Siskos, S.; Nikolaidis, S.; Tatas, K.; Jean-Yves Mignolet: *AMDREL: Designing Embedded Reconfigurable Hardware Structures for Future Reconfigurable Systems-on-Chip for Wireless Communication Applications*, Proceedings of IEEE Workshop on Heterogeneous Reconfigurable Systems on Chip (SOC), 2002

[2] Intel: *Intel® 64 and IA-32 Architectures Software Developer's Manual*
Volume 1: Basic Architecture, available online:
http://download.intel.com/products/processor/ manual/253665.pdf

[3] NVidia: *The GeForce 6 Series GPU Architecture*, available online:
http://download.nvidia.com/developer/GPU_Gems_2/GPU_Gems2_ch30.pdf

[4] Shuai Che; Jie Li; Sheaffer, J.W.; Skadron, K.; Lach, J.: *Accelerating Compute-Intensive Applications with GPUs and FPGAs*, Symposium on Application Specific Processors, 2008

[5] Figuli, P.; Hubner, M.; Girardey, R.; Bapp, F.; Bruckschlogl, T.; Thoma, F.; Henkel, J.; Becker, J.: *A heterogeneous SoC architecture with embedded virtual FPGA cores and runtime Core Fusion*, 2011 NASA/ESA Conference on Adaptive Hardware and Systems, 2011

[6] LEM: *Product catalog Railway Current & Voltage Transducers*, available online: http://www.lem.com/images/stories/files/Products/1-5-3_traction_trackside/ch210103_e.pdf

[7] Mahlein, J.; Igney, J.; Weigold, J.; Braun, M.; Simon, O.: Matrix Converter Commutation Strategies With and Without Explicit Input Voltage Sign Measurement. IEEE Transactions on Industrial Electronics, 2002

[8] Navré project on OpenCores, available online: http://opencores.org/project,navre

[9] Ben Othman, S.; Ben Salem, A.K.; Abdelkrim, H.; Ben Saoud, S.: *MPSoC Design Approach of FPGA-based Controller for Induction Motor Drive*, IEEE International Conference on Industrial Technology ICIT, 2012

[10] Zoubek, O.: *Řízení asynchronního motoru signálovým procesorem*, Diploma thesis, ČVUT FEL 2010

[11] Polach, O.: *Creep forces in simulations of traction vehicles running on adhesion limit.* Wear; 2005. vol. 255, p. 992-1000

[12] Polach, O.: *A Fast Wheel-Rail Forces Calculation Computer Code.* 1999

[13] Kalker, J. J.: *A Strip Theory For Rolling W I T H Slip And Spin.* Mechanics; 1967. vol. 70, no. 1, p. 10-62.

[14] Danzer, J.: *Protiskluzové zařízení tyristorových lokomotiv.* Žel. Technika; 1986. vol. 16, no. 4, p. 155-158.

[15] Park, D. Y.; Kim, M. S.; Hwang, D. H.: *Hybrid Re-Adhesion Control Method for Traction Systém of High-speed Railway.* Electrical Machines and Systems (ICEMS); 2001. vol. 5, p. 739-742

[16] Yasuoka, I.; Henmi, T.; Nakazawa, Y.: *Improvement of Re-adhesion for Commuter Trains with Vector Control Traction Inverter.* PCC-Nagaoka; 1997. p. 51-56

[17] Tarnow, A. C.: *System and method for detecting wheel slip and skid in a locomotive.* US 2008/0051967 A1; 2008.

[18] Kumar, A. K.; Worden, B. D.: *System and method for determining true ground speed in a locomotive.* 2001

[19] Kane, M. E.; Shockley, J. F.; Hickenlooper, H. T.: *Method and system for compensating for wheel wear on a train.* US 2007/0095988 A1; 2007

[20] Mei, T. X.; Yu, J. H.; Wilson, D. A.: *A Mechatronic Approach for Anti-slip Control in Railway Traction.* World Congress The International Federation of Automatic Control; 2008. vol. 17, p. 8275-8280

[21] Kia, S. H.; Henao, H.; Capolino, G. A.: *Torsional vibration assessment in railway traction system mechanical transmission.* IEEE International Symposium on Diagnostics for Electric Machines, Power Electronics and Drives (SDEMPED); 2009. p. 1-8

[22] Danzer, J: *Elektrická trakce 7. - Adheze*, available online on website of Katedra výkonových elektrotechnických systémov, Žilinská univerzita v Žiline as a study material for course Elektrická trakce, http://www.kves.uniza.sk, 2011

[23] Watanabe, T.: *Anti-slip Readhesion Control with Presumed Adhesion Force - Method of Presuming Adhesion Force and Running Test Results of High-speed Shinkansen Train*, Q Rep RTRI (Railw Tech Res Inst), 2000

[24] Kalker, J. J.: *On the rolling contact of two elastic bodies in the presence of dry friction.* Diss. T H Delf; 1967

[25] Kragelski, I. V.; Dobyčin, M. N.; Kombalov V. S.: *Friction and Wear: Calculation Methods*, Pergamon Press, Oxford, 1982

[26] Polach, O.: SBB 460 Adhäsionsversuche, Techn. Report No. 414, SLM Winterthur, 1992

[27] Polach, O.: *Optimierung moderner Lok-Drehgestelle durch fahrzeugdynamische Systemanalyse.* Eisenbahningenieur; 2002. vol. 53, no. 7, p. 50-57

[28] Logston, C. F. Jr.; Itami, G. S.: *Locomotive Friction-Creep Studies.* ASME; 1980

[29] Engel, B.; Beck, H. P.; Alders, J.: *Verschleißreduzierte Radschlupfregelung mit hoher Kraftslußausnutzung.* EB; 1998. vol. 96, no. 6, p. 201-209

[30] Lang, W.; Roth, G.: *Optimale Kraftschlußausnutzung bei Hochleistungs-Schienenfahrzeugen.* ETR; 1993. vol. 42, no. 1,2, p. 61-66

[31] Malvezzi, M.; Pugi, L.; Papini, S.; Rindi A.: *Identification of a wheel–rail adhesion coefficient from experimental data during braking tests*. Proceedings of the Institution of Mechanical Engineers Part F Journal of Rail and Rapid Transit 227(2):128-139; March 2013

[32] Huang, J.; Xiao, J.; Zhao, D.; Wang, S.: *A Wheel Slip Detection Method of Electric Locomotive Based on Time-Frequency Analysis.* International Conference on Intelligent Transportation Systems (IEEE ITSC); 2014. vol. 17

[33] Schwartz, H. J.: *Regelung der Radsatzdrehzahl zur maximalen Kraftschlußausnutzung bei elektrischen Triebfahrzeugen.* VDI Vorschr.; 1992. vol. 12, no. 178

[34] Engel, B.: *Verschleißmindernde Kraftschlussregelung mit Zustandsregler für elektrische Traktionsantriebe.* Diss. TU Clausthal; 1996

[35] Buscher, M.: *Radschlupfregelung zur maximalen Kraftschlußausnutzung bei elektrischen Traktionsantrieben.* Diss. TH Darmstadt; 1995

8. List of Author's Publications

Article in reviewed journal related to the thesis topic:

- ZOUBEK, O. Použití programovatelných logických obvodů v elektrických pohonech. In: *ELEKTRO*. Praha: FCC Public, s. r. o., 2017, 6/2017, p. 6-9, ISSN 1210-0889.

List of publications in WoS related to the thesis topic:

- PICHLÍK, P., ZOUBEK, O., a ZDĚNEK, J. Measuring Device for Measurement of Train Dynamic Motion During Wheel Slip. In: *19th International Conference on Applied Electronics 2014*. Pilsen, 09.10.2014 - 10.10.2014. Pilsen: University of West Bohemia. 2015, p. 247-250. ISSN 1803-7232. ISBN 978-80-261-0276-2. (33%)
  - Number of citations in WoS: 2
    - Zhang, C., Cheng, X., He, J., Liu G.: *Automatic Recognition of Adhesion States Using an Extreme Learning Machine*. In: INTERNATIONAL JOURNAL OF ROBOTICS & AUTOMATION, Volume: 32, Issue: 2, Pages: 194-200, Published: 2017; Journal impact factor (2016): 0.674
    - Novak, M., Ferkova, Z.: *Analysis of Tram DC Traction Motors Pairing*. In: 17th IEEE International Power Electronics and Motion Control Conference (PEMC), Varna, Bulgaria, Date: SEP 25-28, 2016

List of other publications related to the thesis topic:

- ZOUBEK, O., et al. Locomotive Wheel Speed Measurement under Wheel Slip Conditions. In: *Proceedings of PIERS 2015 in Prague*. Progress In Electromagnetics Research Symposium. Praha, 06.07.2015 - 09.07.2015. Cambridge: Electromagnetics Academy. 2015, p. 2528-2533. ISSN 1559-9450. ISBN 978-1-934142-30-1. (25%)
- ZOUBEK, O. High Resolution Shaft Speed Measuring Method. In: *POSTER 2012 - 16th International Student Conference on Electrical Engineering*. Prague, 17.05.2012. Praha: Czech Technical University in Prague. 2012, ISBN 978-80-01-05043-9.
- ZOUBEK, O. a ZDĚNEK, J. Induction Motor Field Oriented Control Using Soft Processor Implemented In Field Programmable Gate Array. In: *Electronic Devices and Systems, IMAPS CS International Conference 2011 Proceedings*. Brno, 22.06.2011 - 23.06.2011. Brno: VUT v Brně, FEKT. 2011, p. 153-158. ISBN 978-80-214-4303-7. (50%)
- ZOUBEK, O. a ZDĚNEK, J. Ultra-Wide Range High Precision Motor Speed Measuring Method Using Incremental Rotary Encoder. In: *XIX. International Symposium On Electric Machinery In Prague*. Praha, 07.09.2011 - 09.09.2011. Praha: ČVUT FEL, Katedra elektrických pohonů a trakce. 2011, p. 140-144. ISBN 978-80-01-04890-0. (50%)

Patents:

- Co-authorship of two pending patents (9% respectively 5% share) related to the topic of the thesis.

Appendix A – Schematics

List of schematics:

- ACLADC (1 page)
  - A small sandwich board with accelerometer and ADC converter, fits into VISIRC.
- VISIRC (2 pages)
  - Zebra method laser-diode and photo-diode driver. Connects with VISREC using Ethernet cable, up to 30 m long.
- X11-IFACE (1 page)
  - Connects with VISREC using Ethernet cable, up to 30 m long.
- LEA-5S (1 page)
  - A board with GPS receiver and backup battery.
- VISREC (3 pages)
  - Four Ethernet links receiver with interface for logic analyzer and USB.

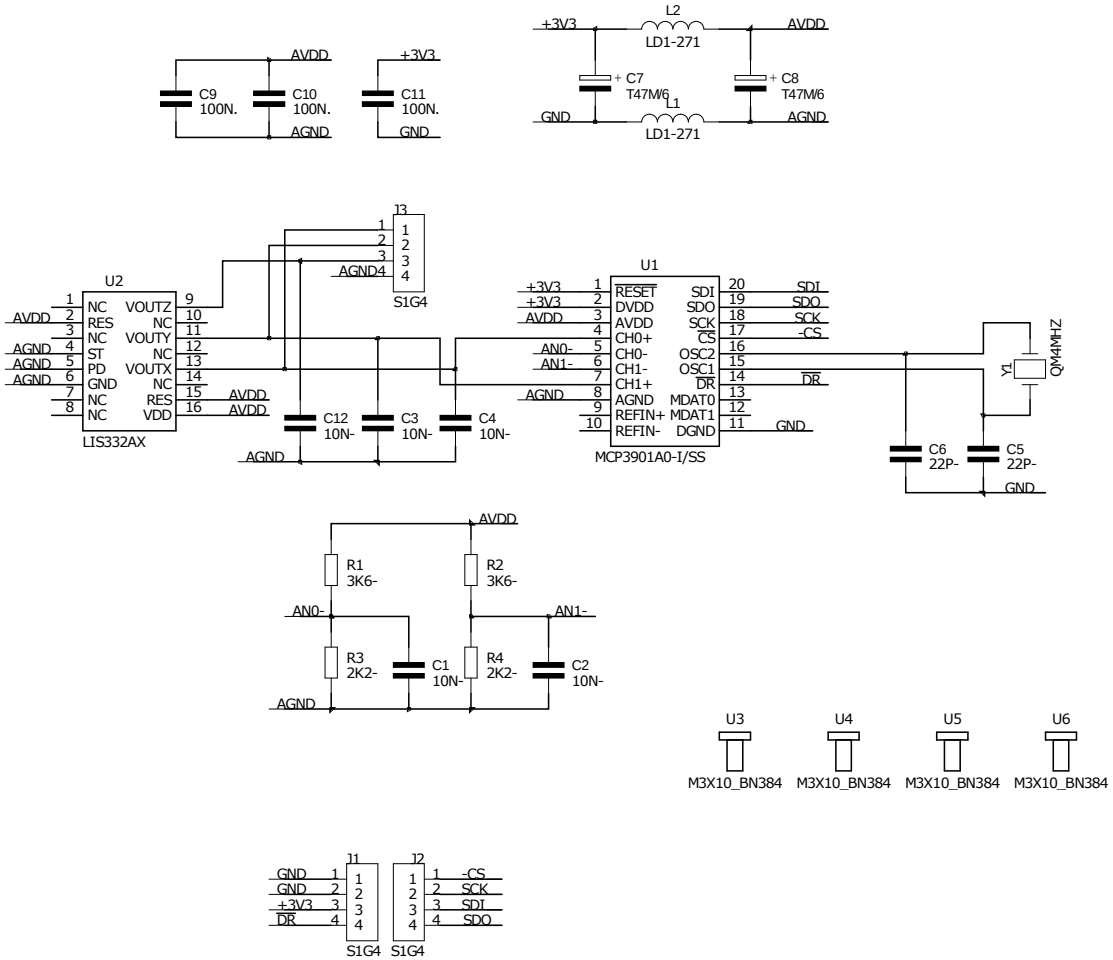

COMPANY:	CTU Prague	REV:	2
TITLE:	ACLADC	PAGE:	1 OF 1

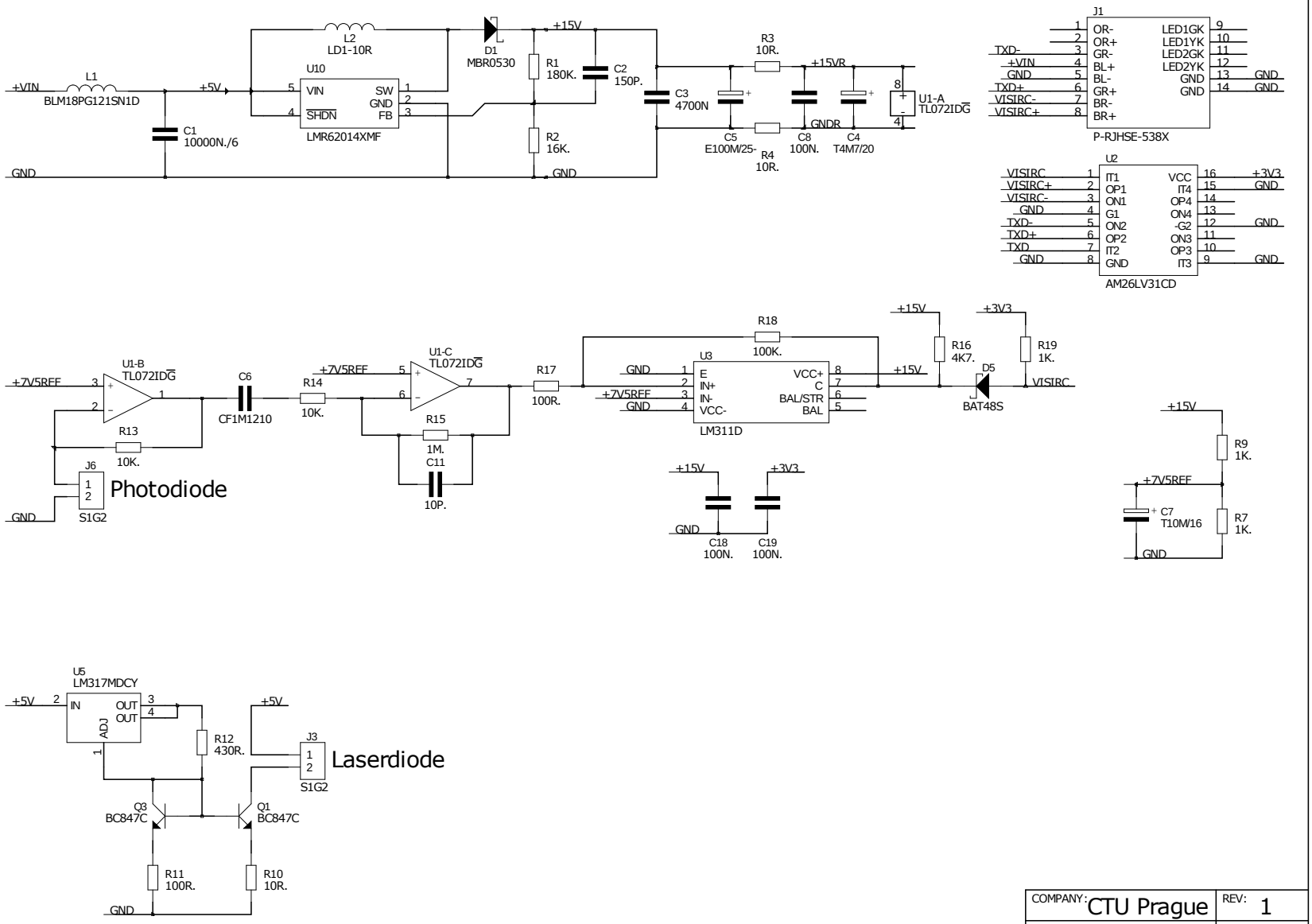

COMPANY:	CTU Prague	REV:	1
TITLE:	VISIRC	PAGE:	1 OF 2

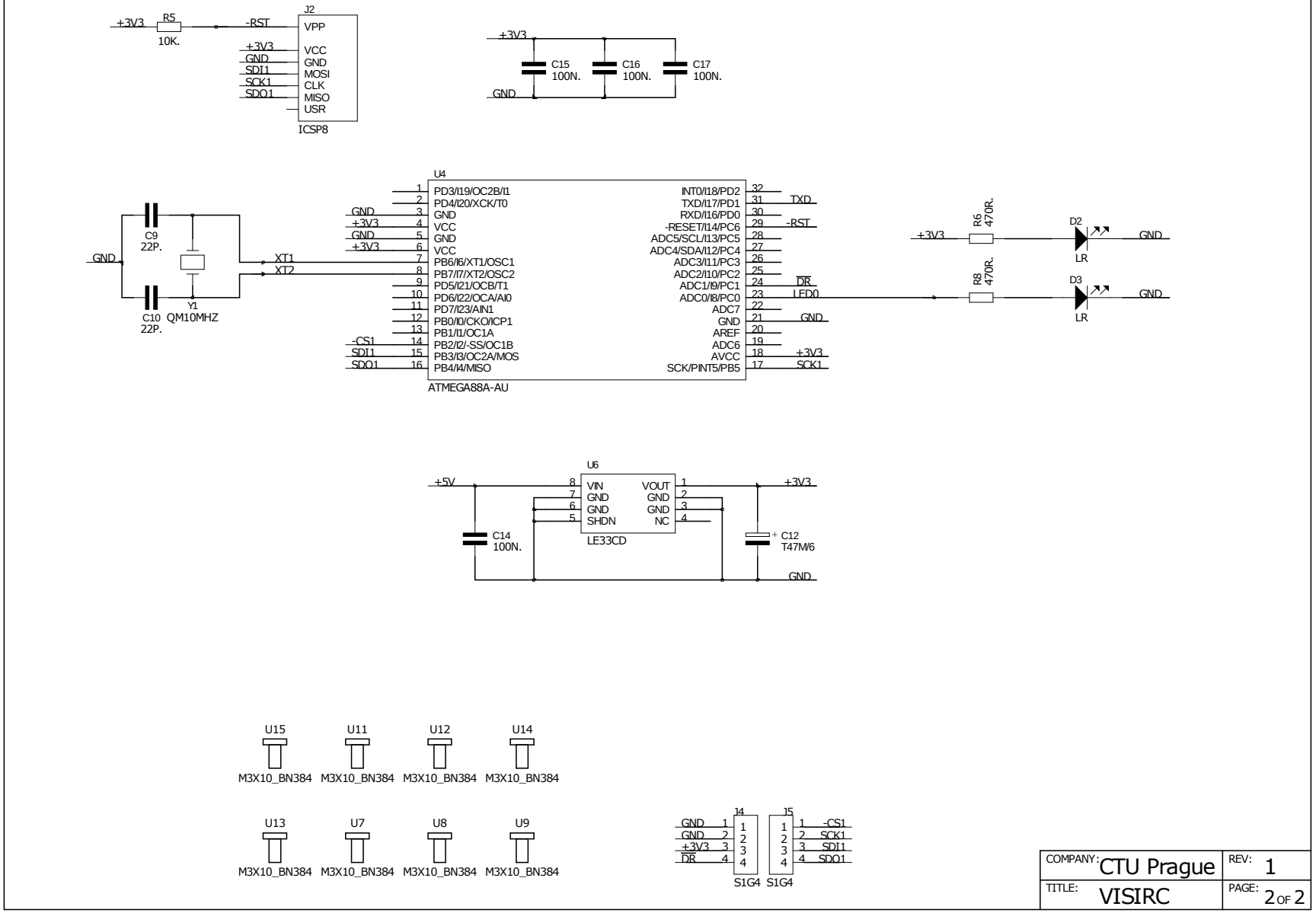
J2
+3V3
R5
10K.
-RST
VPP
+3V3
VCC
GND
GND
SDI1
MOSI
SCK1
CLK
SDO1
MISO
USR
ICSP8
+3V3
C15
100N.
C16
100N.
C17
100N.
GND
U4
C9
22P.
GND
C10
22P.
Y1
QM10MHZ
XT1
XT2
GND
+3V3
GND
+3V3
-CS1
SDI1
SDO1
PD3/I19/OC2B/I1
PD4/I20/XCK/T0
GND
VCC
GND
VCC
PB6/I6/XT1/OSC1
PB7/I7/XT2/OSC2
PD5/I21/OCB/T1
PD6/I22/OCA/AI0
PD7/I23/AIN1
PB0/I0/CKO/ICP1
PB1/I1/OC1A
PB2/I2/-SS/OC1B
PB3/I3/OC2A/MOS
PB4/I4/MISO
INT0/I18/PD2
TXD/I17/PD1
RXD/I16/PD0
-RESET/I14/PC6
ADC5/SCL/I13/PC5
ADC4/SDA/I12/PC4
ADC3/I11/PC3
ADC2/I10/PC2
ADC1/I9/PC1
ADC0/I8/PC0
ADC7
GND
AREF
ADC6
AVCC
SCK/PINT5/PB5
TXD
-RST
DR
LED0
GND
+3V3
SCK1
ATMEGA88A-AU
+3V3
R6
470R.
D2
LR
GND
R8
470R.
D3
LR
GND
U6
+5V
C14
100N.
VIN
GND
GND
SHDN
VOUT
GND
GND
NC
LE33CD
C12
T47M/6
+3V3
GND
U15
U11
U12
U14
M3X10_BN384
M3X10_BN384
M3X10_BN384
M3X10_BN384
U13
U7
U8
U9
M3X10_BN384
M3X10_BN384
M3X10_BN384
M3X10_BN384
J4
GND
GND
+3V3
DR
S1G4
J5
-CS1
SCK1
SDI1
SDO1
S1G4
COMPANY: CTU Prague
REV: 1
TITLE: VISIRC
PAGE: 2 OF 2

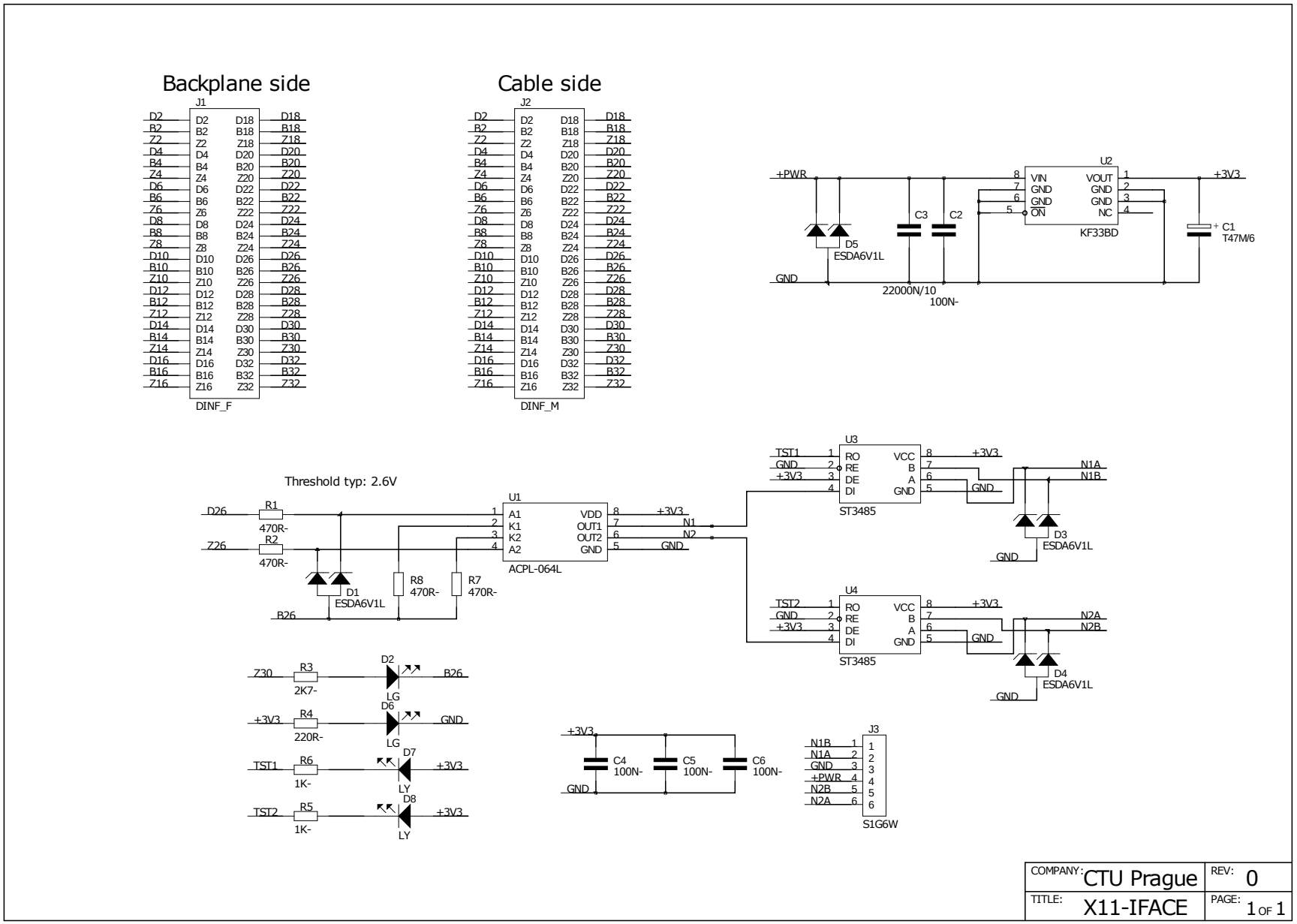
Backplane side
Cable side
J1
J2
DINF_F
DINF_M
U2
KF33BD
+PWR
+3V3
GND
C1
T47M/6
C2
C3
D5
ESDA6V1L
22000N/10
100N-
Threshold typ: 2.6V
U1
ACPL-064L
R1
R2
470R-
D1
ESDA6V1L
R8
R7
U3
U4
ST3485
D3
D4
N1A
N1B
N2A
N2B
R3
2K7-
R4
220R-
R6
1K-
R5
D2
D6
D7
D8
LG
LY
C4
C5
C6
100N-
J3
S1G6W
COMPANY: CTU Prague
REV: 0
TITLE: X11-IFACE
PAGE: 1 OF 1

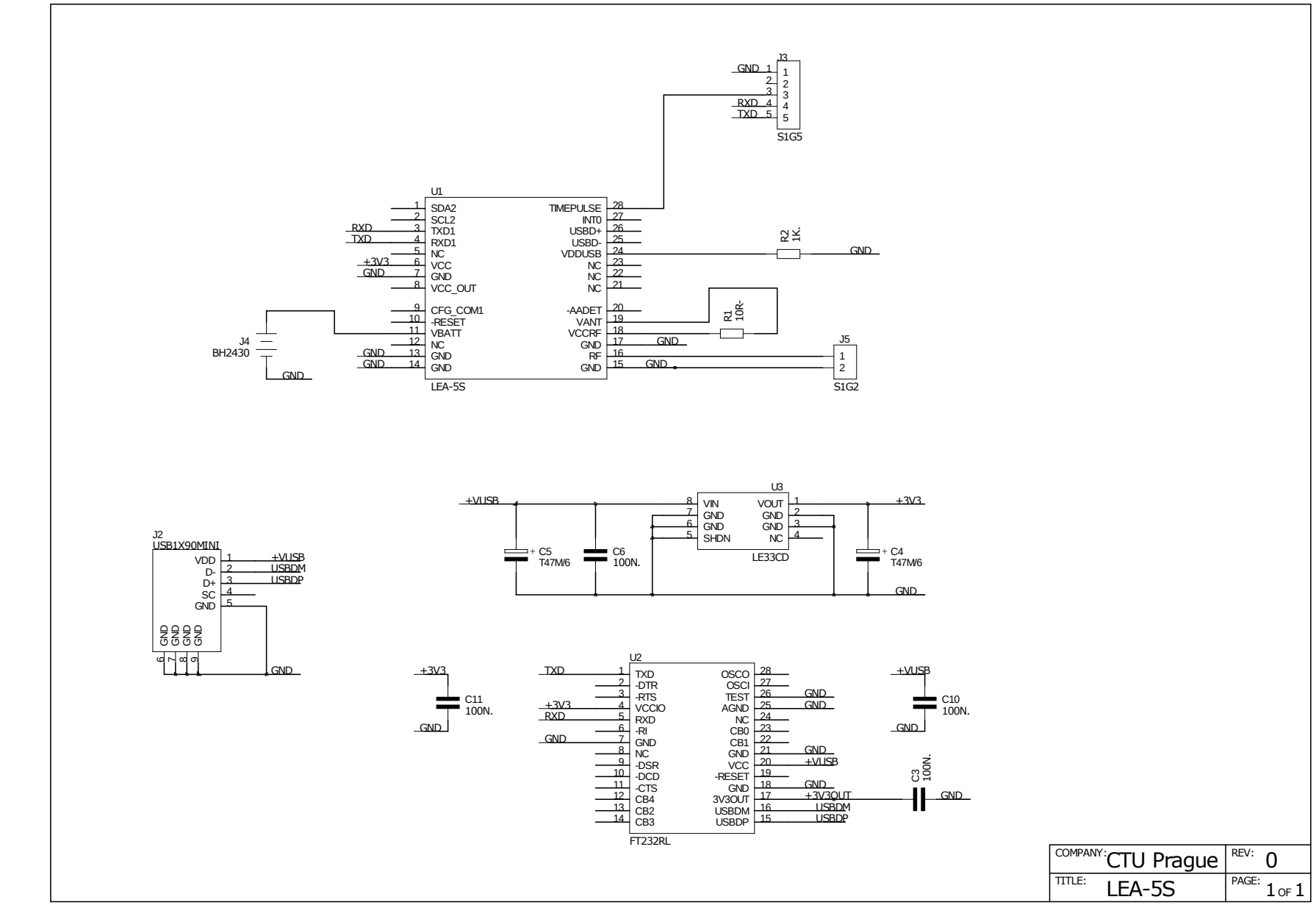

COMPANY: CTU Prague	REV: 0
TITLE: LEA-5S	PAGE: 1 OF 1

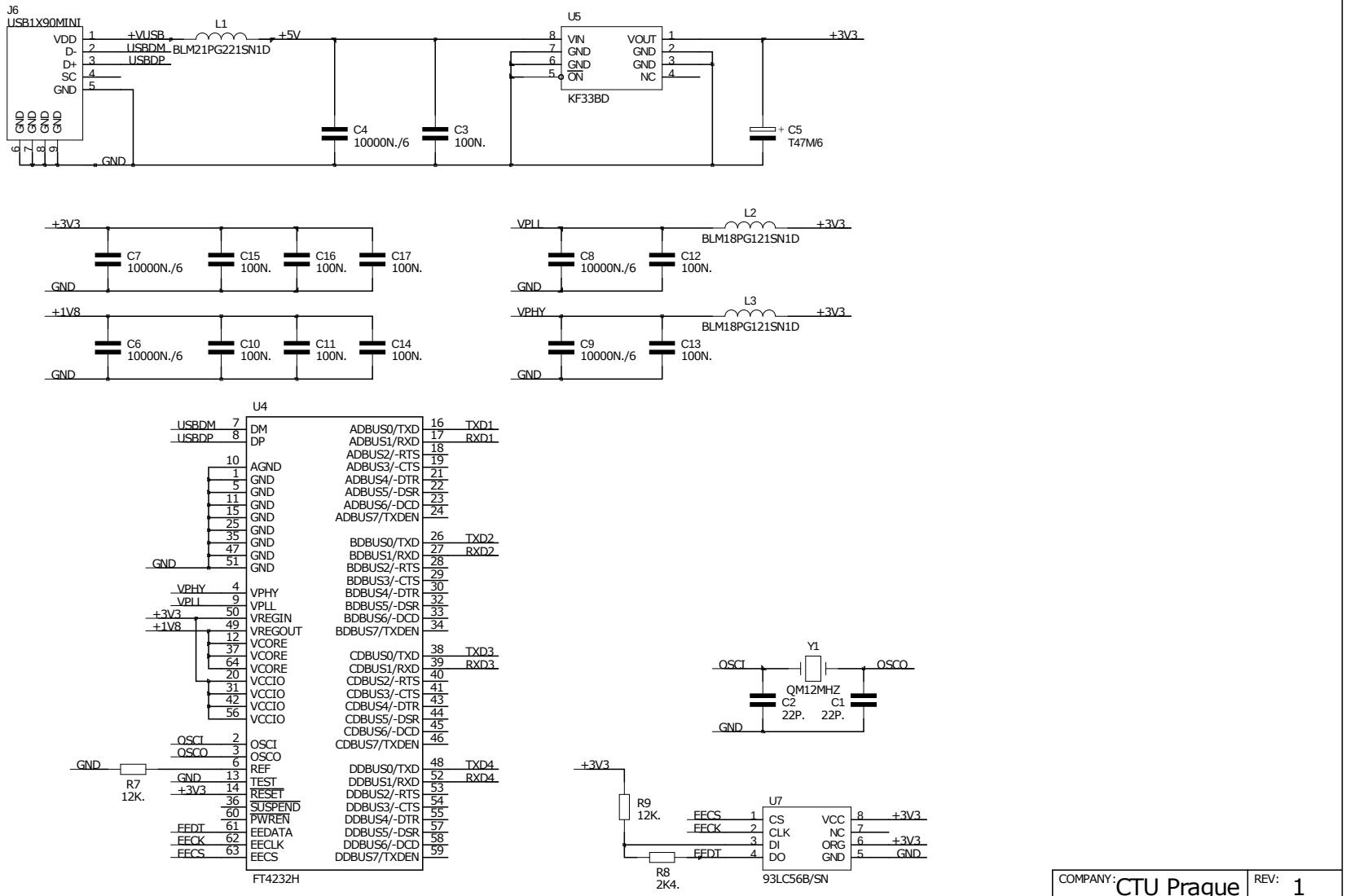

COMPANY: CTU Prague	REV: 1
TITLE: VICREC	PAGE: 1 OF 3

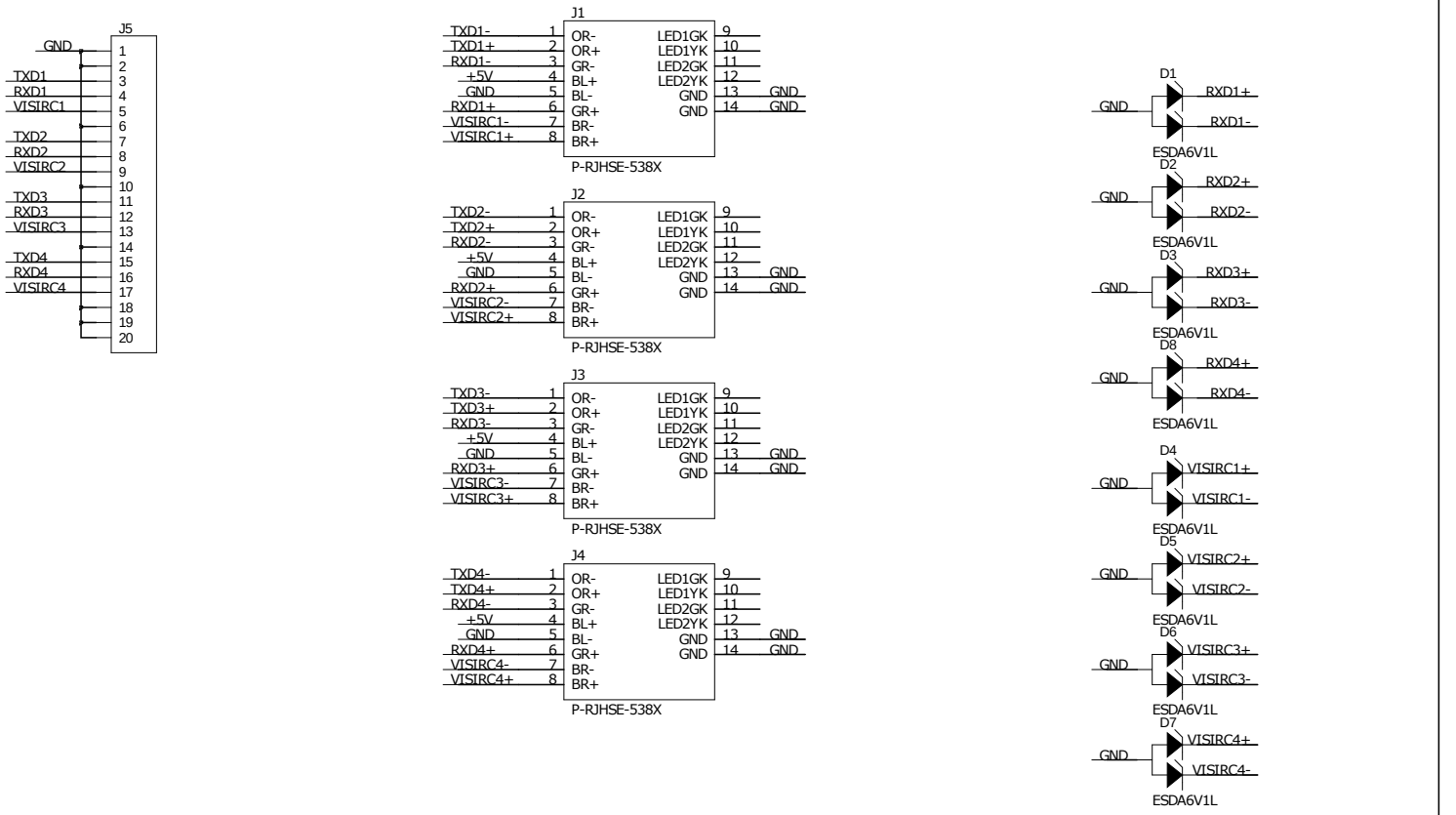

COMPANY: CTU Prague	REV: 1
TITLE: VICREC	PAGE: 2 OF 3

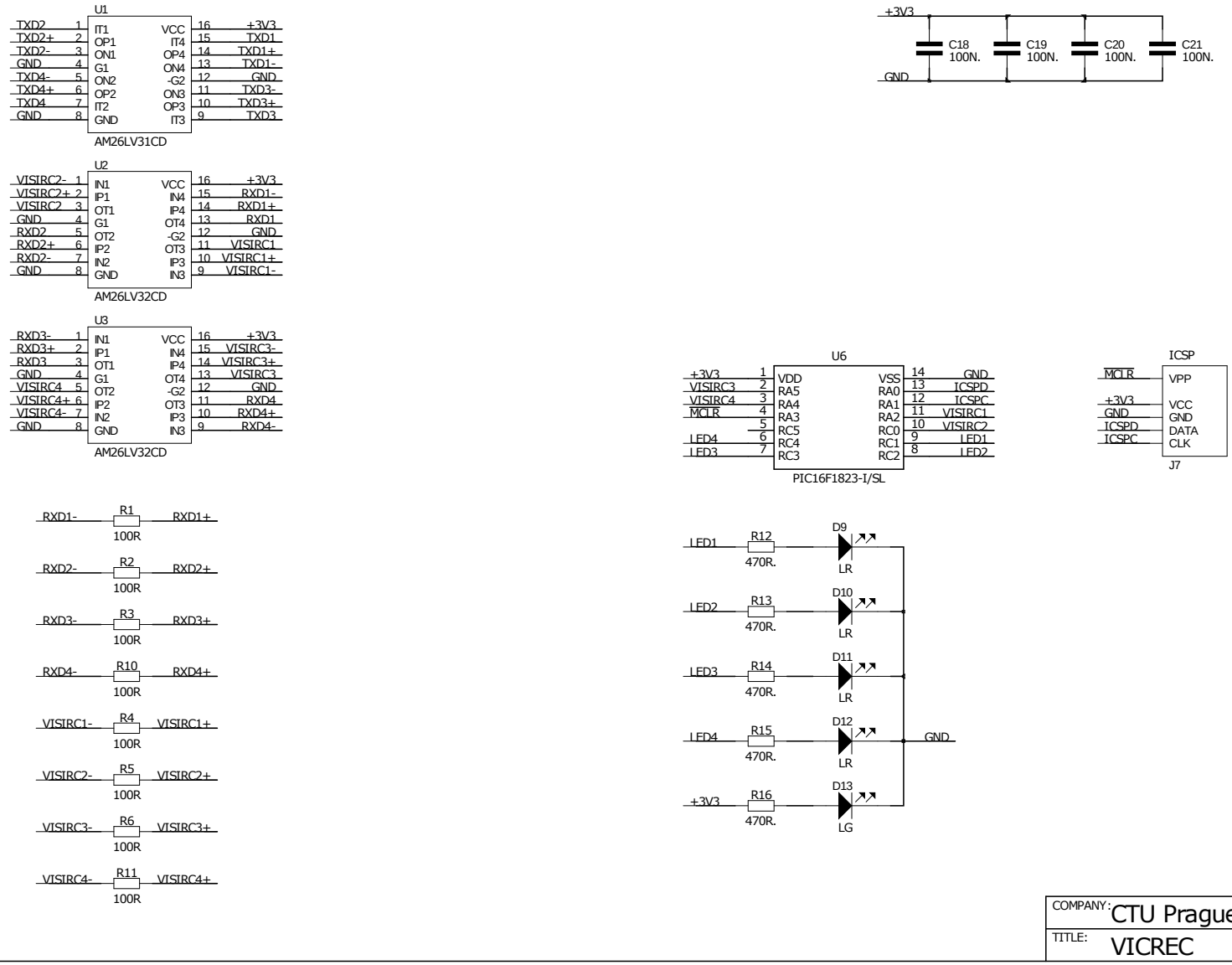
U1
TXD2 1
TXD2+ 2
TXD2- 3
GND 4
TXD4- 5
TXD4+ 6
TXD4 7
GND 8
IT1
OP1
ON1
G1
ON2
OP2
IT2
GND
VCC
IT4
OP4
ON4
-G2
ON3
OP3
IT3
16 +3V3
15 TXD1
14 TXD1+
13 TXD1-
12 GND
11 TXD3-
10 TXD3+
9 TXD3
AM26LV31CD
U2
VISIRC2- 1
VISIRC2+ 2
VISIRC2 3
GND 4
RXD2 5
RXD2+ 6
RXD2- 7
GND 8
IN1
IP1
OT1
G1
OT2
IP2
IN2
GND
VCC
IN4
IP4
OT4
-G2
OT3
IP3
IN3
16 +3V3
15 RXD1-
14 RXD1+
13 RXD1
12 GND
11 VISIRC1
10 VISIRC1+
9 VISIRC1-
AM26LV32CD
U3
RXD3- 1
RXD3+ 2
RXD3 3
GND 4
VISIRC4 5
VISIRC4+ 6
VISIRC4- 7
GND 8
IN1
IP1
OT1
G1
OT2
IP2
IN2
GND
VCC
IN4
IP4
OT4
-G2
OT3
IP3
IN3
16 +3V3
15 VISIRC3-
14 VISIRC3+
13 VISIRC3
12 GND
11 RXD4
10 RXD4+
9 RXD4-
AM26LV32CD
RXD1- R1 100R RXD1+
RXD2- R2 100R RXD2+
RXD3- R3 100R RXD3+
RXD4- R10 100R RXD4+
VISIRC1- R4 100R VISIRC1+
VISIRC2- R5 100R VISIRC2+
VISIRC3- R6 100R VISIRC3+
VISIRC4- R11 100R VISIRC4+
+3V3
GND
C18 100N.
C19 100N.
C20 100N.
C21 100N.
U6
+3V3 1
VISIRC3 2
VISIRC4 3
MCLR 4
5
LED4 6
LED3 7
VDD
RA5
RA4
RA3
RC5
RC4
RC3
VSS
RA0
RA1
RA2
RC0
RC1
RC2
14 GND
13 ICSPD
12 ICSPC
11 VISIRC1
10 VISIRC2
9 LED1
8 LED2
PIC16F1823-I/SL
ICSP
MCLR
+3V3
GND
ICSPD
ICSPC
VPP
VCC
GND
DATA
CLK
J7
LED1 R12 470R. D9 LR
LED2 R13 470R. D10 LR
LED3 R14 470R. D11 LR
LED4 R15 470R. D12 LR
+3V3 R16 470R. D13 LG
GND
COMPANY: CTU Prague
REV: 1
TITLE: VICREC
PAGE: 3 OF 3

Appendix B – Photo Documentation

The locomotive Škoda 93E at home depot